Flow Characteristics and Status of CFD Hydrodynamic Model Development in Sudden Contraction Manifold/Orifice Configurations

W. H. Nurick

Nurick & Associates
6126 Palomar Circle
Camarillo CA 93012

July 2011

**AIR FORCE RESEARCH LABORATORY
PROPULSION DIRECTORATE**

■ **Air Force Materiel Command**   ■ **United States Air Force**   ■ **Edwards Air Force Base, CA 93524**

UNCLASSIFIED

- STINFO COPY -
NOTICE AND SIGNATURE PAGE

Using Government drawings, specifications, or other data included in this document for any purpose other than Government procurement does not in any way obligate the U.S. Government. The fact that the Government formulated or supplied the drawings, specifications, or other data does not license the holder or any other person or corporation; or convey any rights or permission to manufacture, use, or sell any patented invention that may relate to them.

Qualified requestors may obtain copies of this report from the Defense Technical Information Center (DTIC) (http://www.dtic.mil).

AFRL-RZ-ED-TR-2011-0021 HAS BEEN REVIEWED AND IS APPROVED FOR PUBLICATION IN ACCORDANCE WITH ASSIGNED DISTRIBUTION STATEMENT.

FOR THE DIRECTOR:

This report is published in the interest of scientific and technical information exchange, and its publication does not constitute the Government's approval or disapproval of its ideas or findings.

REPORT DOCUMENTATION PAGE

1. REPORT DATE *(DD-MM-YYYY)* July 2011	2. REPORT TYPE Special Report	3. DATES COVERED *(From - To)* 01 May 2007 – 31 May 2011

4. TITLE AND SUBTITLE Flow Characteristics and Status of CFD Hydrodynamic Model Development In Sudden Contraction Manifold/Orifice Configurations	5a. CONTRACT NUMBER
	5b. GRANT NUMBER
	5c. PROGRAM ELEMENT NUMBER
6. AUTHOR(S) W. H. Nurick	5d. PROJECT NUMBER 62203F
	5e. TASK NUMBER
	5f. WORK UNIT NUMBER 50260538

7. PERFORMING ORGANIZATION NAME(S) AND ADDRESS(ES) Nurick & Associates 6126 Palomar Circle Camarillo CA 93012	8. PERFORMING ORGANIZATION REPORT NO.

9. SPONSORING / MONITORING AGENCY NAME(S) AND ADDRESS(ES) Air Force Research Laboratory (AFMC) AFRL/RZS 5 Pollux Drive Edwards AFB CA 93524-7048	10. SPONSOR/MONITOR'S ACRONYM(S)
	11. SPONSOR/MONITOR'S REPORT NUMBER(S) **AFRL-RZ-ED-TR-2011-0021**

12. DISTRIBUTION / AVAILABILITY STATEMENT
Approved for public release; distribution unlimited. PA No. 111028.

13. SUPPLEMENTARY NOTES

14. ABSTRACT
Applications of sudden contraction manifold/orifice configurations range from city water drainage, diesel and gasoline fuel injection systems, and high speed underwater torpedoes, as well as rocket engine injector manifold flow passages. While the literature is extensive and dates back more than a century, the details of the flow characteristics as well as the quantitative impacts on losses are still sketchy at best. A clear understanding of the detailed process flow characteristics and fluid state in the entrance region and throughout the flow path to the orifice exit is a vital element in the ability to more knowledgeably predict these loss coefficients as well as orifice exit flow characteristics. More recent studies have been focusing on the details of the processes in an attempt to better understand the governing variables and quantify flow characteristics impacts. These processes are known to be dependent on orifice configuration, and there are a myriad of possible manifold/orifice configurations with abrupt contraction whose selection depends on both the application and manufacturer preference. The recent generation of empirical correlations has allowed limited verification of hydraulic CFD code predictions and status of their development. However, the data necessary to verify code prediction of orifice exit characteristics and hydraulic flip are lacking. Complete verification allowing for prediction of the global and spatial processes as well as hydraulic flip is vital to the goal of achieving predictive capability of spatial and global spray distributions. Due to the importance of achieving reliable hydraulic CFD models, a brief discussion is included of attempts to verify CFD code prediction with experimental data.

15. SUBJECT TERMS
zero-point energy; plane wave diffraction; vacuum fluctuations; vacuum energy

16. SECURITY CLASSIFICATION OF:			17. LIMITATION OF ABSTRACT	18. NUMBER OF PAGES	19a. NAME OF RESPONSIBLE PERSON Stephen A. Danczyk
a. REPORT Unclassified	b. ABSTRACT Unclassified	c. THIS PAGE Unclassified	SAR	85	19b. TELEPHONE NO *(include area code)* N/A

This Page Intentionally Left Blank

TABLE OF CONTENTS

LIST OF FIGURES

LIST OF FIGURES (Cont'd)

LIST OF TABLES

This Page Intentionally Left Blank

1.0 INTRODUCTION

Applications of sudden contraction manifold/orifice configurations range from city water drainage, diesel and gasoline fuel injection systems, and high speed underwater torpedoes, as well as rocket engine injector manifold flow passages. While the literature is extensive and dates back more than a century, the details of the flow characteristics as well as the quantitative impacts on losses are still sketchy at best. A clear understanding of the detailed process flow characteristics and fluid state in the entrance region and throughout the flow path to the orifice exit is a vital element in the ability to more knowledgeably predict these loss coefficients as well as orifice exit flow characteristics. More recent studies have been focusing on the details of the processes in an attempt to better understand the governing variables and quantify flow characteristics impacts. These processes are known to be dependent on orifice configuration, and there are a myriad of possible manifold/orifice configurations with abrupt contraction whose selection depends on both the application and manufacturer preference.

For most applications the manifold/orifice configurations fall into two general categories; (1) where all the manifold flow enters the contraction orifice; and (2) where only a portion of the manifold flow enters the contraction orifice and the remainder flows downstream via the manifold. The major flow regimes are: (1) Non-Cavitation, (2) Inception of Cavitation, (3) Full Cavitation, (4) Supercavitation, and (5) Hydraulic Flip. The flow characteristics and processes within these major regimes vary depending on the manifold/orifice configuration and the selection of operating regime; the later depends on application. Lastly, the specific controlling flow and design variables are dependent on the flow characteristics from the manifold entrance to the contraction orifice exit. All of these processes result in energy losses, and the magnitude of the overall energy loss as well as the orifice exit jet quality determine the efficacy of any design to meet application requirements. Therefore, the essence of any application utilizing sudden contraction manifold/orifice designs is the definition of the free jet exit characteristics such as jet: spreading characteristics, velocity profile, direction, pressure fluctuations, flowrate variations, and exit breakup characteristics. These characteristics are the initial input to the prediction of downstream global and spatial processes such as mixing, atomization, and combustion characteristics.

Empirically derived hydraulic process prediction of both discharge coefficient and inception of flow regimes currently depend on steady-state relationships that have been shown by experiment to describe these processes. However, from the onset of inception of cavitation through supercavitation, steady-state flow conditions do not exist. This is the result of the collapse of vapor bubbles that produce strong overpressures at varying frequencies. The issue; however, is whether the instabilities in the flow measurably impact the steady-state hydrodynamic processes. Experimental data have shown that the principal impact of these perturbations is to affect hydraulic flip at either the contraction orifice entrance within the inception of cavitation flow regime, or at orifice reattachment at the orifice exit within the supercavitation flow regime. Consequently, the impact of pressure perturbation should be directed to its triggering hydraulic flip in both flow

1

regimes. Further, since operation in supercavitation is important to many applications, the details of the "reattachment" and unsteady flow characteristics impact on the free jet, at the orifice exit, need to be defined in detail.

The importance to manifold/orifice configuration viability is directly linked to the avoidance of hydraulic flip, which is currently only qualitatively predictable. Prediction of such processes as those affecting hydraulic flip, as well as the orifice exit characteristics defining the initial boundary conditions of the free jet, in all probability must await the development/verification of detailed hydrodynamic CFD models.

The recent generation of empirical correlations has allowed limited verification of hydraulic CFD code predictions and status of their development. However, the data necessary to verify code prediction of orifice exit characteristics and hydraulic flip are lacking. As stated above, complete verification allowing for prediction of the global and spatial processes as well as hydraulic flip is vital to the goal of achieving predictive capability of spatial and global spray distributions. Due to the importance of achieving reliable hydraulic CFD models, a brief discussion is included of attempts to verify CFD code prediction with experimental data.

W. H. Nurick - May 2011

2.0 MANIFOLD/SUDDEN CONTRACTION ORIFICE CONFIGURATIONS

There are a myriad of potential manifold/orifice configurations, as shown by Idelchik [1]. This report describes a selected number of configurations used primarily in rocket engine and diesel engine injectors. The selected manifold/orifice configurations are noted in Fig. 1 and can be divided into two general categories: (1) where all the manifold flow enters the contraction orifice (i.e. $W_1=W_2$); and (2) where only a portion of the manifold flow enters the contraction orifice and the remainder continues to flow downstream via the manifold (i.e. $W_1 \neq W_2$).
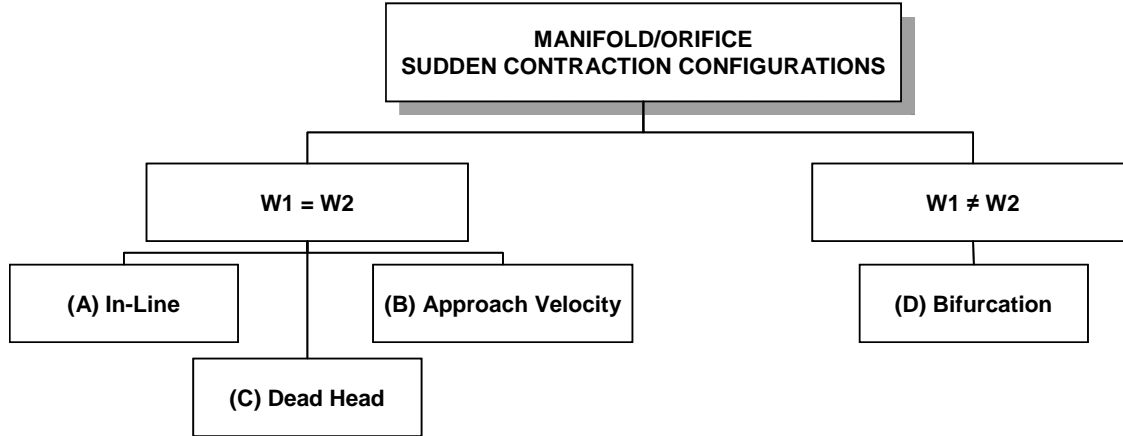
Figure 1: Manifold/Sudden Contraction Orifice Configurations Categories

All of these configurations are illustrated in Fig. 2, and the contraction orifice entrances are sharp edge. As shown in Fig. 2, the in-line (A), approach velocity (B), and dead head configurations (C) conform to (1) above, while the single branching bifurcation orifice configuration (D) conforms to (2). For the in-line and dead head configurations, the orifice entrance flow is axisymmetric while for the other configurations the entrance characteristics are asymmetric.

In the in-line (A) and the dead head 90° (C) configurations, the manifold flow accelerates axially symmetrically to enter the sudden contraction orifice; while for the other two configurations (B and D), as well as the dead head configuration for turning angles other than 90°, the flow entering the orifice is highly asymmetric. Obtaining axially symmetric flow at the entrance is difficult to achieve even with an in-line configuration, since even small manufacturing irregularities can cause flow tripping resulting in vortex generation at the entrance. The 90° dead head configuration presents even more challenges, since the inlet flows are opposed and stagnation occurs when they meet. This requires that both flows are exactly equal to result in symmetric flow into a 90° contraction orifice.

For the branching manifold/orifice configuration the inlet manifold flow is bifurcated, and a portion of the total flow enters the sharp edge abrupt contraction while the remainder flows downstream within the manifold. For this configuration the flow entering the contraction orifice is axially asymmetrical The approach velocity

3

configuration is a special case of the branching configuration wherein the exit manifold is terminated downstream of the injection orifice; and while all the flow enters the abrupt contraction injection orifice, this configuration results in a portion of the flow to experience reverse flow in the downstream manifold, redirecting that portion of the flow to accelerate as it enters on the downstream side of the orifice.

W1 = W2 CONFIGURATIONS

A: In-Line Configuration

D_1, V_1

Vena-Contracta

Reattachment

D_2, V_2

B: Approach Velocity Configuration

D_1, V_1

Reattachment

Vena-Contracta

D_2, V_2

C: Dead-Head Configuration

D_1, V_1 D_3, V_3

Reattachment

Vena-Contracta

D_2, V_2

W1 ≠ W2 CONFIGURATIONS

D: Flow Bifurcation Configuration

D_1, V_1 D_3, V_3

Reattachment

Vena-Contracta

D_2, V_2
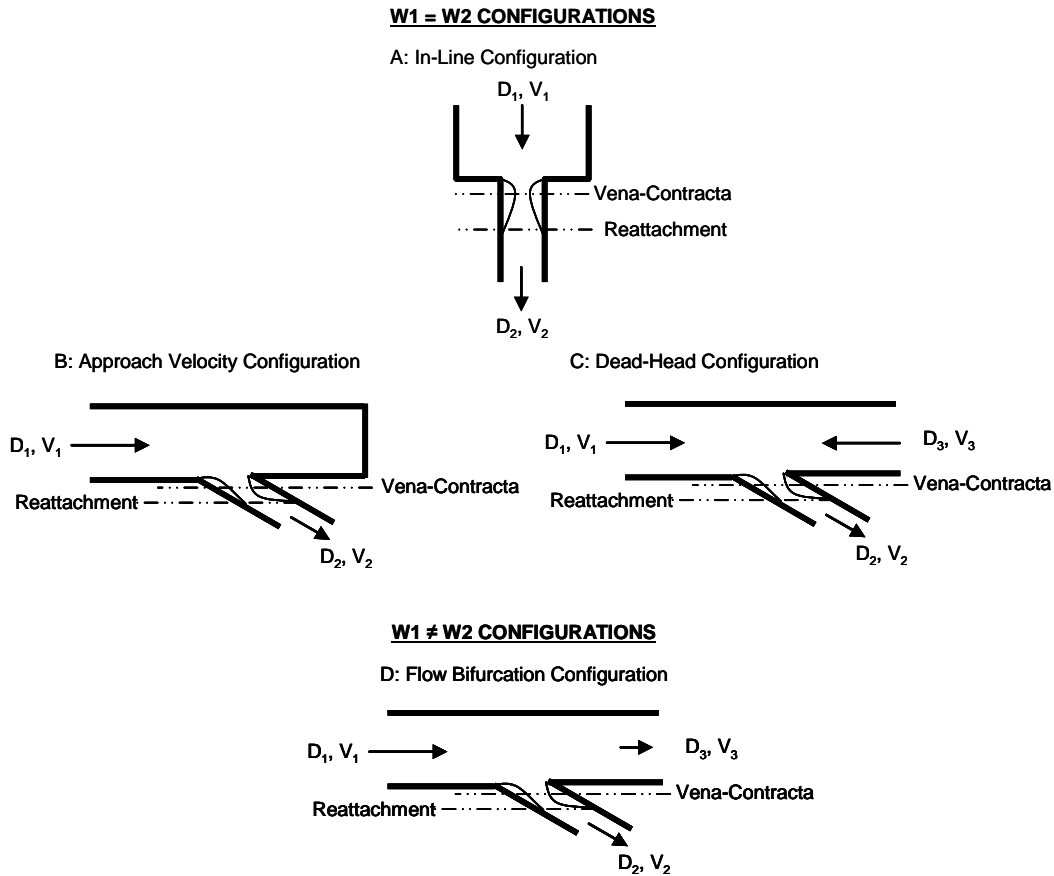
Figure 2: Manifold/ Sudden Contraction Orifice Configurations

It is not surprising that for each configuration and flow regime there are unique process differences. This fact is clearly shown and described in this report.

4

3.0 FLOW REGIMES

The flow regimes considered herein are: non-cavitation, inception of cavitation, full cavitation, supercavitation, and hydraulic flip. These flow regimes are illustrated in Fig 3. In the non-cavitation regimes the discharge coefficient is controlled by Reynolds number; and typically for high Re number (> 1×10^4) C_d is ~ constant for a given L/D. Depending on the orifice L/D and Reynolds number, the fluid can flow full in the orifice or experience hydraulic flip. Assuming that hydraulic flip does not occur and the Reynolds number further increases (i.e. moving left approaching full cavitation), a fuzzy region appears at the orifice entrance where surface irregularities act as sites where dissolved gases in the fluid tend to form bubbles, then as Re further increases, larger bubbles are formed in the core region of any vortices that occur in this region. This flow region is termed inception of cavitation. These bubbles are short lived in that the liquid static pressure quickly increases as they move downstream and the bubbles implode, causing pressure perturbations near the entrance. If the pressure amplitude is sufficiently high, hydraulic flip can occur. Again, assuming that hydraulic flip does not occur as the Re number continues to increase, the static pressure at the orifice edge reaches the vapor pressure, and the flow separates, forming a vapor cavity which, depending on orifice L/D, reattaches downstream or total separation occurs. If reattachment occurs, the flow at the throat becomes constant (i.e. "choked") and discharge coefficient is now a function of the "full cavitation" index noted in Fig.3. Further lowering the cavitation index, C_d varies as indicated by the line between the intersection of non-cavitation and full cavitation flow regimes, and 0. As cavitation index is lowered, the vapor cavity lengthens and then jumps to reattach at the orifice exit. This condition is defined as supercavitation. At this point hydraulic flip can occur or will eventually occur as the cavitation index is further lowered. As discussed in this report, note that hydraulic flip can occur in the non-cavitation, the inception of cavitation and the supercavitation flow regimes.
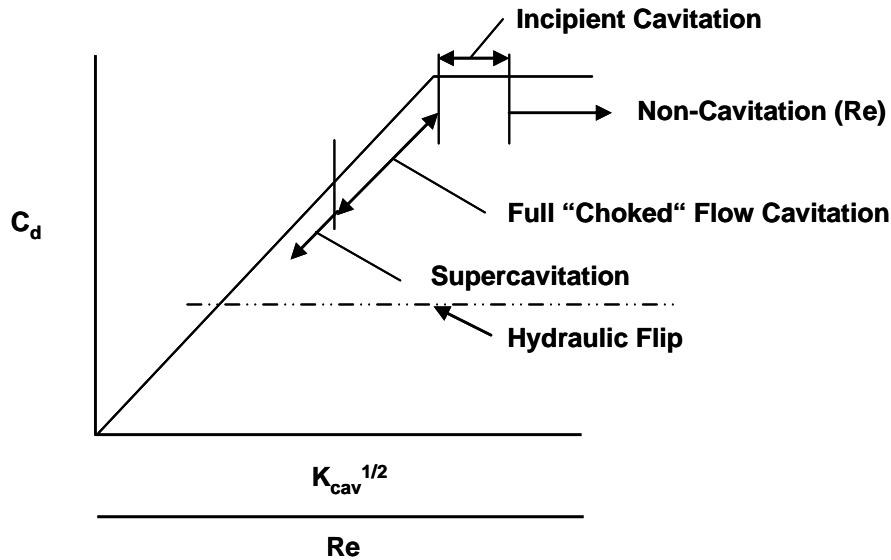
Figure 3: Major Flow Regimes in Sudden Contraction Orifice Flow

For all of the configurations, Idelchik [1] provides the largest body of data and correlations for the overall hydrodynamic pressure losses in non-cavitation flow regime. Nurick [2, 3, and 4] provides additional experimental results in the non-cavitation flow regime for small orifice/manifold area ratios. For the inception of cavitation, full cavitation, and supercavitation flow regimes, the three references of Nurick represent the largest single body of data and correlations available to date. The hydraulic flip results also represent a significant body of data in both non-cavitation and cavitation flow regimes.

The major divisions along the flow path from the manifold inlet to the orifice exit free jet are indicated in Fig. 4. These specific processes that occur only within a specified location within the flow path are important. For example, under some operating conditions the flow becomes unsteady due to pressure perturbations caused primarily by vapor bubble collapse. Although bubble collapse occurs throughout the orifice from its inlet to its exit flow path, the major impacts occur at the contraction orifice entrance during initiation of cavitation and at the orifice exit at supercavitation operating conditions. Consequently, within each of these divisions, specific process variables are impacted by the unsteady flow characteristics within these flow regimes and configuration geometry.
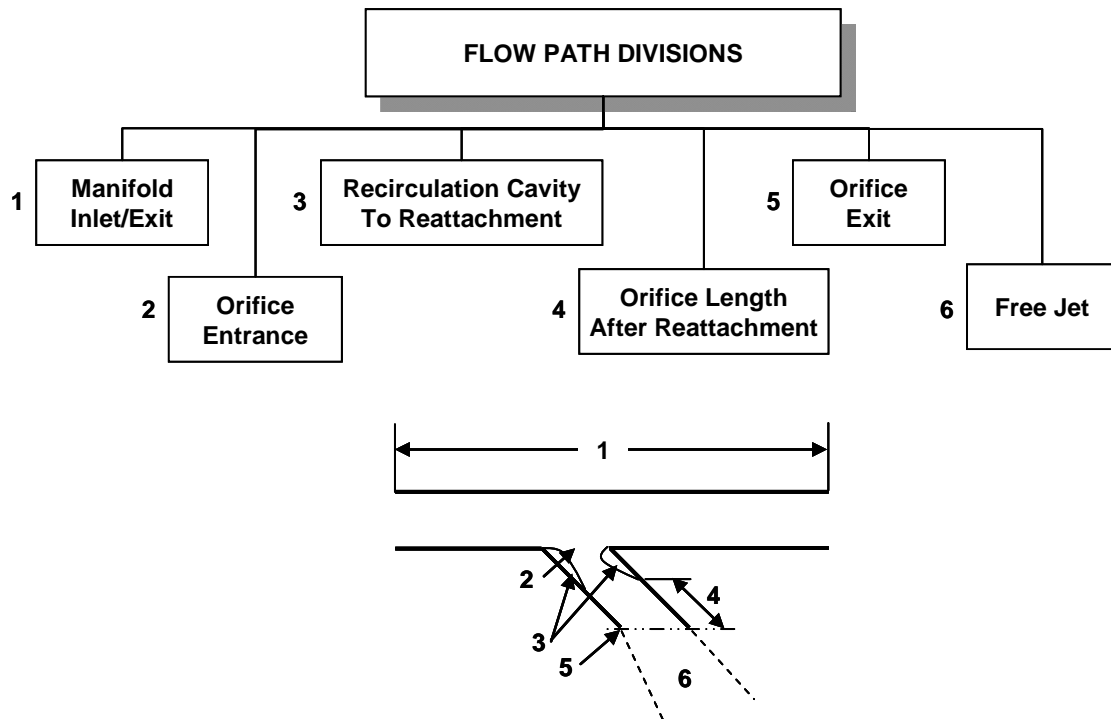
Figure 4: Major Flow Path Division in Manifold/Orifice Configuration

6

4.0 NON-CAVITATION FLOW

For the **in-line and approach velocity configurations,** since all of the manifold flow enters the injection orifice, the manifold inlet/orifice velocity ratio, based on continuity, is defined by Eq. 1.

$$\frac{V_1}{V_2} = \frac{A_2}{A_1} \tag{1}$$

In the **dead head configuration** W_1 represents the sum of the two apposing manifold inlets flows. Consequently, the velocity ratio for this configuration is:

$$\frac{V_1}{V_2} = \frac{1}{2}\frac{A_2}{A_1} \tag{2}$$

In the **branching configuration** the manifold/orifice velocity ratio is a function of both the area ratio and the flowrate ratio and is defined by Eq. 3.

$$\frac{V_1}{V_2} = \frac{W_1}{W_2}\frac{A_2}{A_1} \tag{3}$$

Consequently, in the bifurcation branching flow, the velocity ratio is no longer uniquely related to area ratio but varies as shown in Eq. 2 and 3. Further, while the flow characteristics in the contraction orifices are similar for these configurations there are unique differences.

4.1 OVERALL HYDRODYNAMIC LOSS COEFFICIENT

4.1.1 In-Line Orifice Overall Hydrodynamic Loss Coefficient
The accelerating flow entering a sudden contraction causes a separation of flow at the entrance, producing a recirculation zone that continues until reattachment is reached. The overall flow can be described by application of the Bernoulli equation as shown in Eq. 4. This equation assumes 1-dimensional flow, and the subscripts 1 and 2 refer to the manifold inlet and sudden contraction [of the?] orifice downstream of the reattachment point, respectively. The total head loss (HL) in this equation represents the change in the energy line that accounts for all non-recoverable losses (i.e., such as orifice contraction, expansion, and friction losses).

$$HL = \Delta P + \frac{\rho}{2g}\left(V_1^{\,2} - V_2^{\,2}\right) \tag{4}$$

Contraction/expansion losses include any entrance and reattachment losses. Therefore HL is equal to:

$$HL = HL_{1-r} + HL_{fr} \tag{5}$$

Note that the subscript 1-r represents the losses between the contraction orifice entrance and the reattachment point, and the subscript fr refers to friction losses to the orifice exit.

The total loss coefficient is defined by Eq. 6, all losses from the contraction orifice entrance to the orifice exit. It is easily shown that it is also equal to the right hand side (RHS).

$$KL_{TOT} = \frac{HL_{1-r} + HL_{fr}}{\frac{\rho V_2^{\ 2}}{2g}} = \frac{\Delta P}{\frac{\rho V_2^{\ 2}}{2g}} + \left(\frac{A_2}{A_1}\right)^2 - 1 \tag{6}$$

The individual loss coefficients are: first, the loss associated with the orifice entrance to reattachment as stated in Eq.7; and second, due to friction from the reattachment to the orifice exit, Eq 8:

$$KL = \frac{HL_{1-r}}{\frac{\rho V_2^{\ 2}}{2g}} \tag{7}$$

$$K_{fr} = f\frac{L}{D} \tag{8}$$

Experimental data [3] can show that the friction factor, as defined by the Blasius Equation, adequately predicts this loss.

$$f = 0.316\,\mathrm{Re}^{-0.25} \tag{9}$$

As noted by many researchers, for the in-line configuration, the minor loss coefficient is only a function of area ratio, as functionally stated in Eq. 10.

$$KL = f\left(\frac{A_2}{A_1}\right) \tag{10}$$

Further, experimental data shows that the loss coefficient at $A_2/A_1 = 0$ is 0.5 while for area ratio of 1, since no contraction occurs, is 0. Idelchik [1] assumes the general form of the Borda-Carnot head loss for a sudden expansion and applying the limits suggests the relationship of Eq. 10 to be:

$$KL = 0.5\left(1 - \frac{A_2}{A_1}\right) \tag{11}$$

Then, evaluating a large body of experimental data, Idelchik determined the best fit was that shown in Eq. 12.

$$KL = 0.5\left(1 - \frac{A_2}{A_1}\right)^{\frac{3}{4}}$$

(12)

A summary of several of the relationships describing the minor loss coefficient for in-line configurations is shown in Fig. 5. Note the significant variation in KL given by these correlations. It is surprising that even at this date the only agreement is the limit at area ratio of 0 and 1.
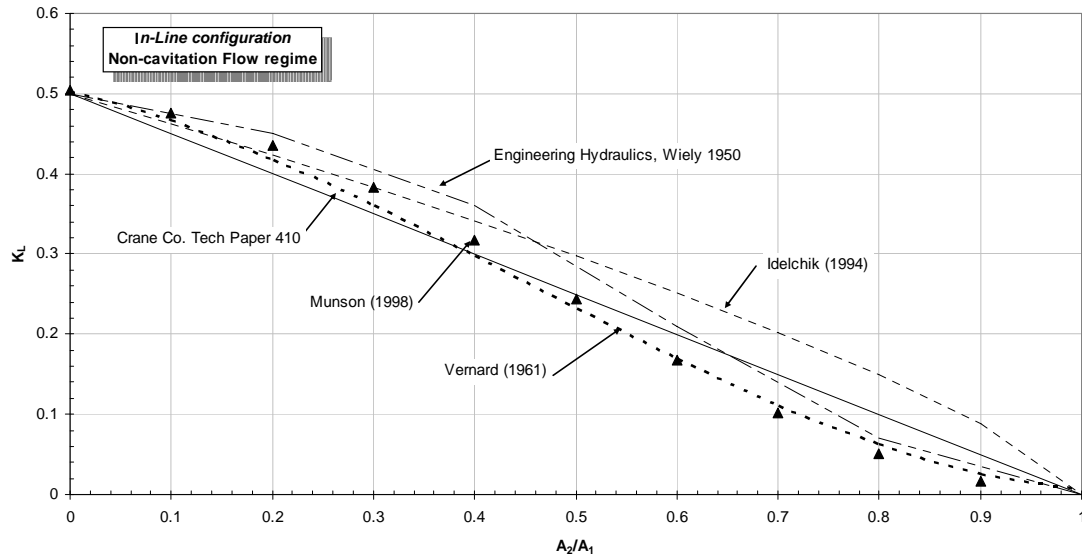
Figure 5: Comparison of In-Line Sudden Contraction Loss Coefficient Predictions

The Crane Co. [5] predictions (Eq. 11) are published in table form in the Standard Handbook for Mechanical Engineers [6]. The Engineering Hydraulics predictions [7] are published in the Chemical Engineers Handbook [8]. Idelchik's correlation can be found in his text [1]. Vernard's prediction [9] is based on the assumption that the contraction portion of the entrance loss is linear between the two limits. The correlation of Munson [10] correlates reasonably with Idelchik at the lower area ratio and Vernard at the higher area ratio values. There appears to be no comparison as to the accuracy of any of the predictive equations at this time.

After a century of study it is surprising that the value of the loss coefficient for sudden contraction is still not defined with any greater accuracy than that indicated in Fig. 5. Use of the Munson correlation appears to be a reasonable average between the above data for high Reynolds numbers (Re > $1x10^4$).

9

$$KL = -0.021 + 0.585 \left[1 + \exp \left(\frac{A_2 / A_1 - 0.705}{0.233} \right) \right]^{-2.29} \qquad (13)$$

4.1.2 Dead Head Orifice Hydrodynamic Coefficient

In the deadhead configuration, the inlet flow is split and flows in equal parts from each side of the manifold toward the contraction orifice. Consequently the velocity ratio defined by Eq. 2 substituted into Eq. 4 results in:

$$\frac{HL_{1-r} + HL_{fr}}{\dfrac{\rho V_2^{\,2}}{2g}} = \frac{\Delta P}{\dfrac{\rho V_2^{\,2}}{2g}} + \left(\frac{A_2}{2A_1} \right)^2 - 1 \qquad (14)$$

The left hand side (LHS) of Eq. 14 is the total loss coefficient which is composed of both the minor loss coefficient, KL, and the friction loss coefficient, KL_{fr}. The relationship for KL is valid for all configurations if KL can be shown to be a constant over the range of orifice kinetic energy and head loss for a given area ratio. Data [4] shows that for the dead head configuration a linear relationship exists, as shown in Fig. 6.
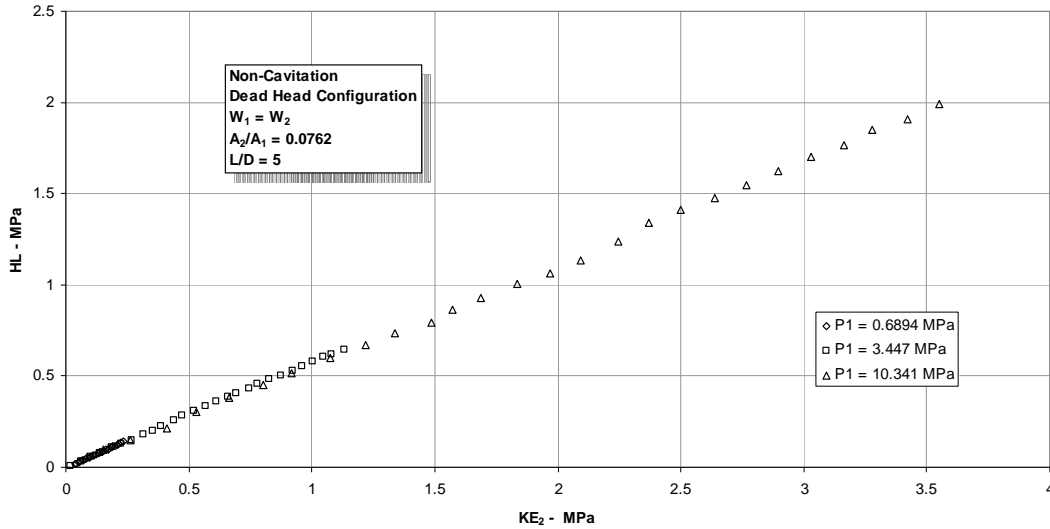
Figure 6: Relationship between Contraction Head Loss and Orifice Kinetic Energy

Note that the value of the discharge coefficient in the non-cavitation flow regime, for L/D of 5, area ratio of 0.0766 in Appendix A, is 0.8. Converting to KL using Eq. 15 results in $KL = 0.472$ since $KL_{fr} = 0.09$ (Blasius Eq.).

$$KL = \frac{1}{C_d^{\,2}} - 1 - KL_{fr} \qquad (15)$$

10

For turning angle between 60° and 90° the values of KL are nearly identical to those of the in-line configuration. However, at turning angle $> 90^o$ KL increases, showing that, unlike the in-line configuration, the entrance losses are a function of turning angle.

4.1.3 Approach Velocity Orifice Hydrodynamic Coefficient
Over the same range of parameters as the dead head configuration, the approach velocity loss coefficient is identical to that of the dead head and in-line configurations. In addition, the linear relationship between orifice kinetic energy and head loss is also identical. The data plots for the approach velocity configuration in addition to the dead head configuration are included as Appendix B.

4.1.4 Branching Orifice Hydrodynamic Loss Coefficient
The branching orifice configuration flow between the manifold and the contraction orifice is governed by the same equation as for the in-line configuration, Eq. 4 and 5. Eq. 6, however, must be in terms of the velocity ratio since the manifold flow is bifurcated. This results in Eq.16:

$$\frac{HL_{1-r} + HL_{fr}}{\dfrac{\rho V_2{}^2}{2g}} = \frac{\Delta P}{\dfrac{\rho V_2{}^2}{2g}} + \left(\frac{V_1}{V_2}\right)^2 - 1 \tag{16}$$

For this configuration the loss coefficient (HL_{1-r}) is a function of velocity ratio, area ratio, and the turning angle as functionally indicated in Eq. 17; and is supported by Idelchik [1]. Consequently, a linear relationship for KL for this configuration must include all three variables.

$$KL = f(V_1 / V_2, A_2 / A_1, \theta) \tag{17}$$

Of particular interest is whether the relationship between HL_{1-r} and $\rho V_2{}^2/2g$ can be considered constant for a given velocity ratio (equivalent to area ratio for in-line configurations). Data [4] results indicate that when velocity ratio is held constant the loss coefficient is constant over the entire operating range of $\rho V_2{}^2/2g$ as shown in Fig.7. In addition note that while the velocity ratios are constant for a given angle over the range in HL, they are not the same value for all turning angles (Fig 7). This type of linear relationship is found for all angles over a wide range in velocity ratio and orifice kinetic energy.

The data [4] supports the notion that a relationship can be developed to relate loss coefficient as a function of velocity ratio for all turning angles similar to that of the in-line orifice configuration, and that for the branching orifice configuration, for small area ratios, the loss coefficient is independent of area ratio and is consistent with in-line results [2]. However, for large area ratios, area ratio is an independent variable.

11
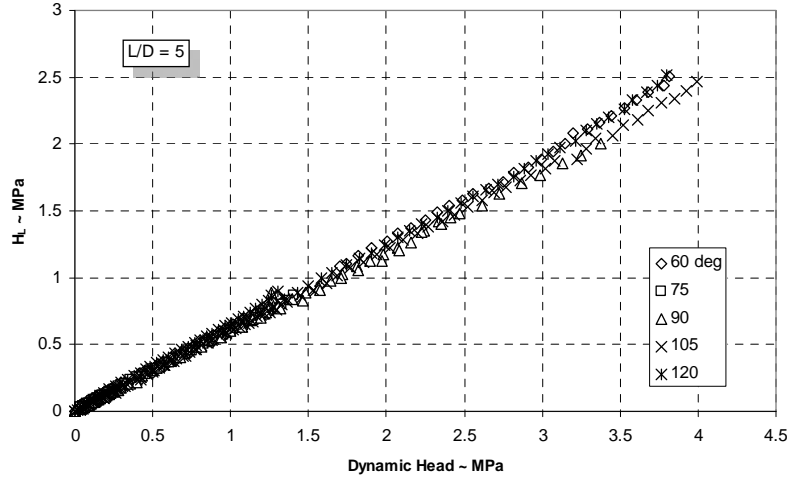
Figure 7: Relationship between Contraction Head Loss and Orifice Kinetic Energy

Eq. 18 represents the KL correlation [4] modified so that the friction component of the data is subtracted to represent only the minor loss coefficient. This correlation is valid for the small area ratio branching orifice configuration.

$$KL = A\left(\frac{V_1}{V_2}\right)^2 + B\left(\frac{V_1}{V_2}\right) + C \qquad (18)$$

Where:

$$A = -0.0105(\theta) + 1.974$$
$$B = +0.0376(\theta) - 3.3468$$
$$C = -0.002(\theta) + 0.681$$

Eq. 18 is presented in graphical form in Fig. 8 and compared with the in-line configuration to illustrate that, as A_2/A_1 approaches 0 the loss coefficient approaches 0.5, which is consistent with physical reasoning if the turning losses are negligible. The magnitude of turning losses for this configuration is discussed later.

Comparison of both Idelchik [1], converted from the manifold to the orifice exit kinetic energy basis, and Nurick's correlations, both for 90° turning angle, are shown in Eq 19 and 20.

$$Nurick : KL = 0.53 + \left(\frac{V_1}{V_2}\right)^2 \qquad (19)$$

$$Idelchik : KL = 1 + \left(\frac{V_1}{V_2}\right)^2 \qquad (20)$$

Of particular interest is that Idelchik's prediction does not asymptote at KL ~ 0.5, as would be expected as the velocity ratio approaches 0, unless in his experiments the flow turning losses are not negligible. Data presented later in this report shows that turning losses are indeed negligible for all configurations except for the 75° and 90° branching configuration at the lowest upstream pressure tested (i.e. 0.689 MPa). Another possibility is that Idelchik's data is for larger area ratios.
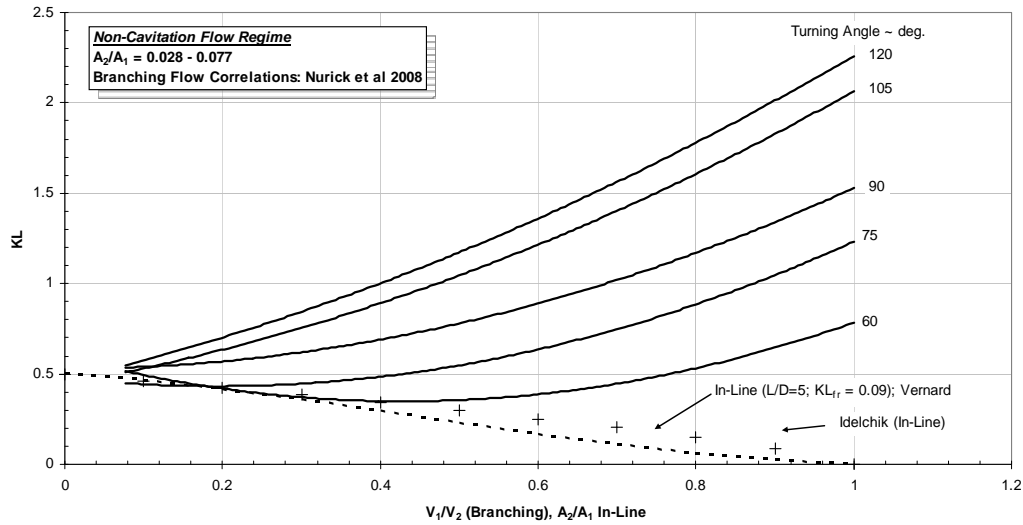
Figure: 8: Branching Flow Sudden Contraction Loss Coefficient

A comparison of 90° turning angle predictions of both Idelchik [1] and Costa [11] in Fig. 9 suggest that at V_1/V_2 of 1 (i.e., $A_1 = A_2$) the loss coefficient is ~ 1.25; while for the small diameter ratio [4] of area ratio 0.077, the loss coefficient increases to 1.5. This trend is consistent with in-line predictions also shown in Fig 9. Consequently, for high Reynolds number, KL is independently a function of area ratio in addition to velocity ratio and turning angle for branching flow as indicated earlier in Eq. 17.
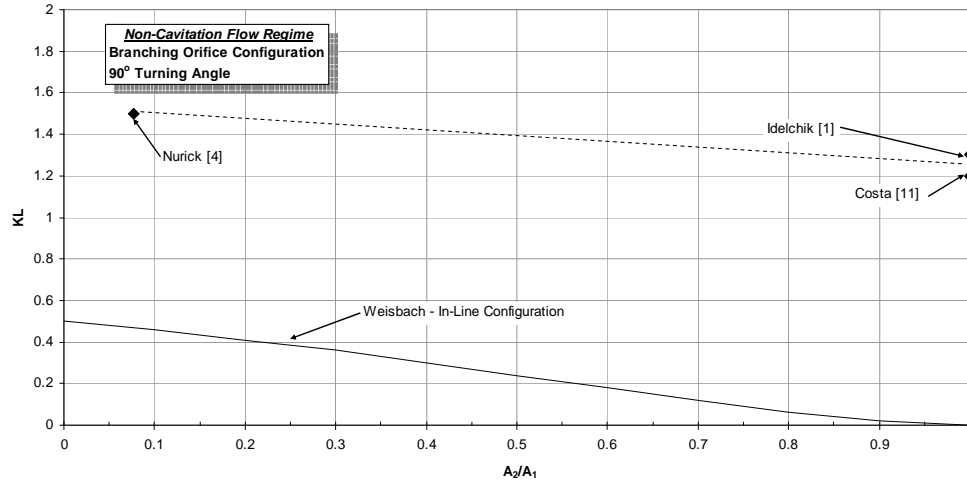
Figure 9: Comparison of Loss Coefficient for 90° T-Junction at $V_1/V_2 = 1$

4.2 CONTRACTION COEFFICIENT

The coefficient of contraction for the manifold axis in-line configuration is well documented in the literature. The earliest work is that of Weisbach [12] for non cavitation flow conditions when flow is accelerated by an abrupt change (i.e., sharp edge) in flow area where the acceleration causes the flow to form a recirculation eddy along the orifice boundary with a minimum flow area at the vena-contracta. The contracted accelerated central flow velocity is maximized at the minimum area (i.e., vena-contracta), then decelerates as the flow expands to full orifice flow. A sketch taken from Vernard [9], Fig. 10, illustrates these flow characteristics.
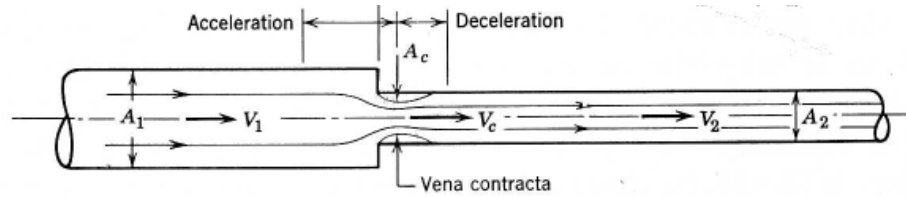
Figure 10: Abrupt Contraction for In-Line Configuration [9]

The contraction coefficient C_c is defined as the ratio of the orifice area to the core flow area at the vena-contracta or:

$$C_c = \frac{A_c}{A_2} \qquad (21)$$

14

4.2.1 In-Line Flow Contraction Coefficient

The relationship between the ratio of manifold inlet velocity and the orifice exit velocity is for in-line configuration in terms of the manifold/orifice area ratio, as determined by Weisbach's [12] defined in Eq. 22. This is a best fit equation for his experimental data for **high Reynolds number** ($> 1 \times 10^4$).

$$C_c = 0.3147 \left(\frac{A_2}{A_1} \right)^4 - 0.1278 \left(\frac{A_2}{A_1} \right)^3 + 0.1502 \left(\frac{A_2}{A_1} \right)^2 + 0.0451 \left(\frac{A_2}{A_1} \right) + 0.617 \qquad (22)$$

The Weisbach results are considered the standard for contraction coefficient with sharp-edge sudden- contraction orifice configurations at high Reynolds number. However; the contraction coefficient is extremely sensitive to the orifice sharpness defined as the radius of curvature divided by the orifice diameter (i.e., r/D). This impact has been experimentally evaluated by several researchers. For example, Hamilton [13] that shows that no vena-contracta can form when r/D is:

$$r / D \geq 0.14 D \qquad (23)$$

Nurick [2] then utilized Hamilton's result to include the impact of smaller values of r/D on inlet rounding; Eq. 24.

$$(C_c)_{r/D} = \left[\left(\frac{1}{(C_c)_{r/D=0}} \right)^2 - 11.4 r / D \right]^{-\frac{1}{2}} \qquad (24)$$

Recent results by Echouchene and Belmabrook [14] show that for low Reynolds numbers ($< 10^4$), C_c is impacted by Reynolds number over the entire range of r/D; Fig. 11.
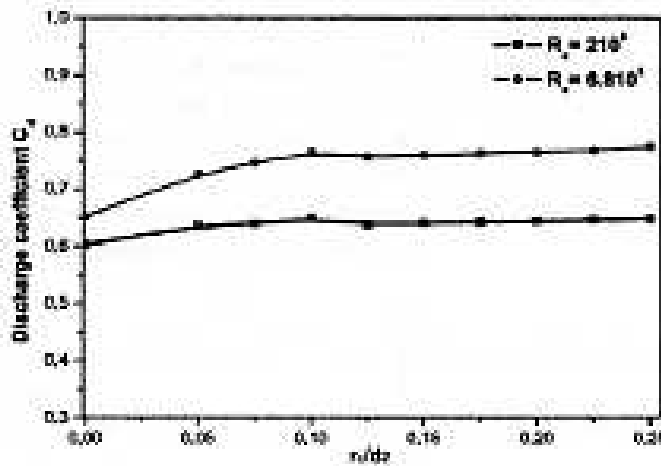
Figure 11: Discharge Coefficient vs. Inlet Corner Radius [14]

15

It should be noted that the contraction coefficient remains constant for both non-cavitation and cavitation at high Reynolds number turbulent flow; and, therefore, is dependent only on area ratio for this configuration.

4.2.2 Dead Head Contraction Coefficient
Since for this configuration the manifold inlet flow is divided into two apposing streams, the ratio of inlet-to-orifice exit velocity is not directly interchangeable with area ratio, as shown in Eq. 2. Consequently Weisbach's correlation would not be expected to directly apply. However, the data over a wide range in turning angle (60° to 120°) shows that the contraction coefficient is constant within experimental accuracy at 0.62, as noted in Appendix B, and is consistent with the in-line contraction coefficient for small area ratios.

4.2.3 Approach Velocity Contraction Coefficient
The definition of the velocity ratio for the approach velocity configuration is identical to the in-line configuration, Eq. 1, and is, therefore, interchangeable; so it would be expected that the Weisbach relationship may be applicable. The results of testing [4] over a wide range in turning angle (60° to 120°) again show that the contraction coefficient is constant within experimental accuracy at 0.62 for small area ratio. This can be noted in Appendix B. This value is consistent with the in-line contraction coefficient for small area ratios.

4.2.4 Branching Flow Contraction Coefficient
For the branching flow configuration, the velocity ratio is dependent on both the flowrate and area ratio, as noted in Eq. 3; and therefore the Weisbach relationship would not be expected to apply. For branching flow in the cavitation flow regime, Nurick [4] published contraction coefficient correlations over a range in turning angles as a function of velocity ratio. While the value of contraction was obtained under cavitation conditions, the results show the exact same characteristics between cavitation and non-cavitation, as was found for the in-line configuration. Consequently the [4] results are considered valid in both flow regimes. The contraction coefficient relationship is:

$$\left(C_c\right)_{r/D=0} = A\left(\frac{V_1}{V_2}\right)^2 + B\left(\frac{V_1}{V_2}\right) + C \tag{25}$$

Where:
$$A = -0.0001808(\theta)^2 + 0.04078(\theta) - 2.3191$$

$$B = 0.000139(\theta)^2 - 0.0355(\theta) + 2.0328$$

$$C = 0.614$$

The values of C_c with variations in velocity ratio using Eq. 25 are shown in Fig. 12 and are compared with the non-cavitation axial in-line configuration C_c variations. Note that V_1/V_2 for axial in-line configuration is equal to A_2/A_1. Of particular interest is that all configurations and angles converge at low values of velocity ratio and, in fact, as angle decreases for branching flow configuration, the value of C_c tends to equal that of axial in-

line configuration. Note that for branching orifice the minimum velocity ratio is at 100% of the flow through the contraction branching orifice and is equal to A_2/A_1.
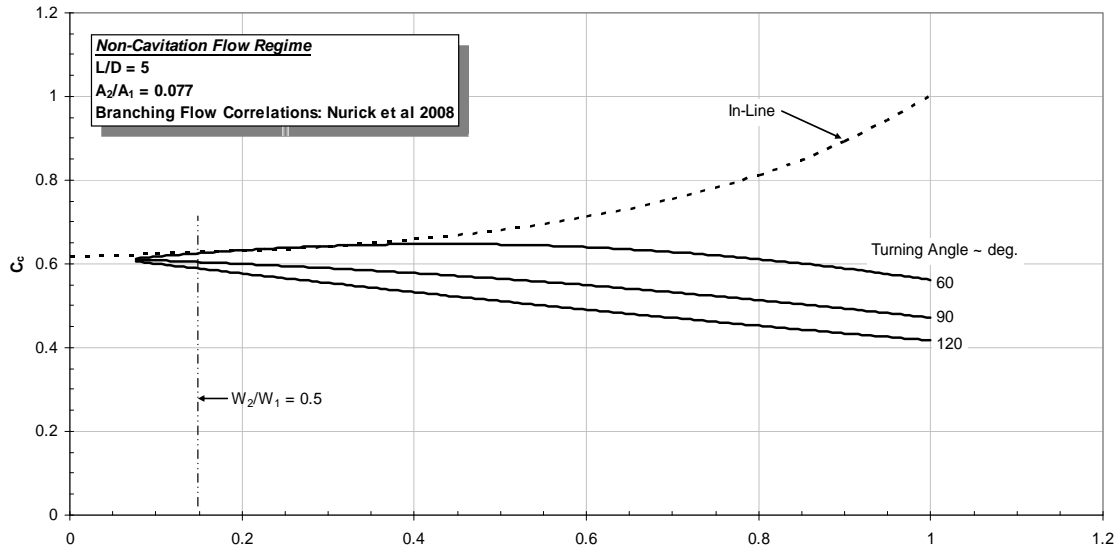
Figure 12: Comparison of C_c for Branching Flow with Axial In-Line Configuration

The independent impact of angle on C_c is most probably the result of the asymmetric flow characteristics at the orifice entrance. CFD analysis prediction of separation characteristics, shown in Fig. 13, for 60° turning angle 2D orifice configuration, indicates that the separation characteristics at the entrance on the upstream and downstream side vary as the flowrate ratio varies.
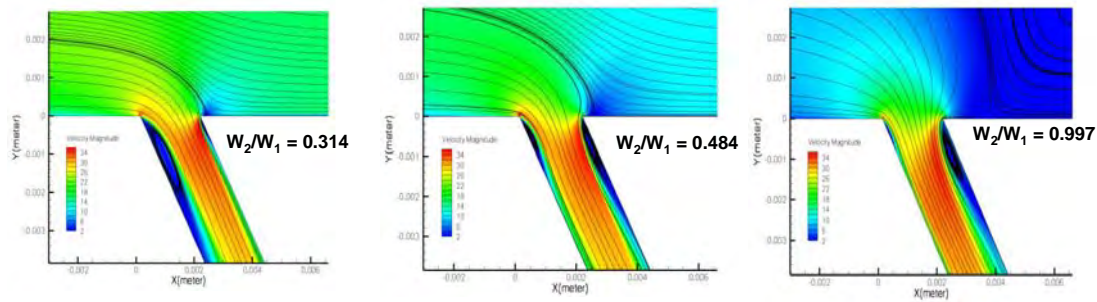
Figure 13: CDF Flow Characteristics for 60° Turning Angle 2D Orifice

Note that the separation is primarily on the upstream edge for flowrate ratios less than 0.5 and on the downstream side for flowrate ratios greater than 0.5. Experimental measurements to date are lacking in substantiating these CFD predictions.

4.3 MANIFOLD EXIT FLOW CHARACTERISTICS LOSS COEFFICIENT

Manifold losses for in-line configurations are limited to pipe friction losses and based on both the L/D and Reynolds number of the feeder orifice. For branching manifold/orifice configurations, manifold losses are those that occur between connective downstream sudden-contraction orifices; or, for approach velocity configurations, the turning and stagnation losses downstream of the contraction orifice. Currently there is no data for manifold losses associated with either the dead head or approach velocity configurations, so this discussion is limited to branching orifice configurations.

4.3.1 Branching Flow Manifold Loss

This analysis shows that at low flowrate ratios the manifold losses would be expected to be small. However, as the flowrate ratio approaches 0.5, the eddy formation increases in intensity, with multiple eddies forming as the flowrate ratio approaches 1. This characteristic is supported by Idelchik [1]. A qualitative example of manifold losses determined by CDF analysis is shown in Fig. 14.

The only known correlation for manifold loss coefficient in branching orifice configurations is that of Idelchik [1]. Idelchik, for $A_2/A_1 > 0.4$ and $A_2/A_1 < 0.4$, makes no distinction between 0 and 90 degrees impact on KL_1 but does predict that pressure drop in the manifold is a strong function of flowrate ratio, as depicted in Fig. 15.
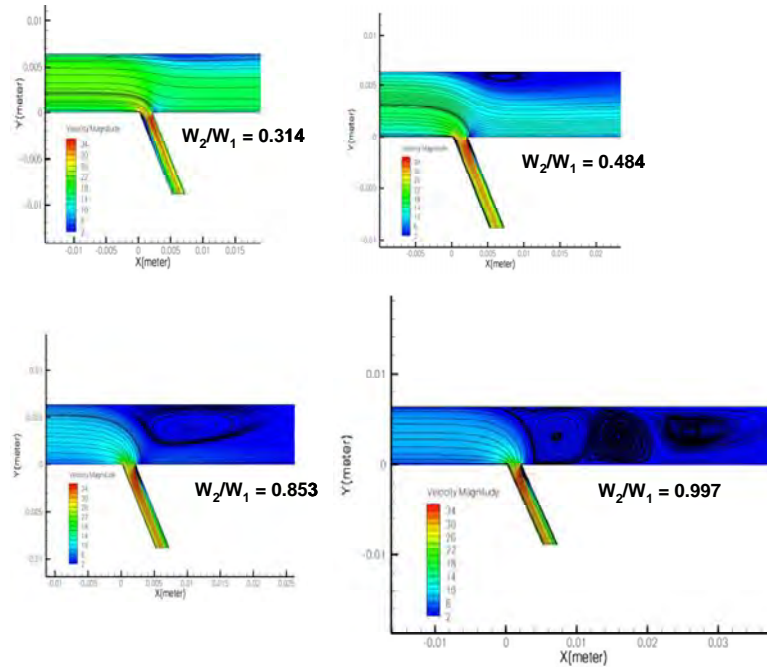
Figure 14: Branching Orifice Configuration Manifold Eddies with Increasing Contraction Orifice Flowrate Ratio

In addition to Idelchik's data, the data of Costa [11] for a T-junction configuration is also included in Fig. 15 and compares well with Idelchik for $A_2/A_1 > 0.4$ and flowrate ratios > 0.2. Note that in this Figure the manifold loss coefficient is based on the manifold inlet kinetic energy.
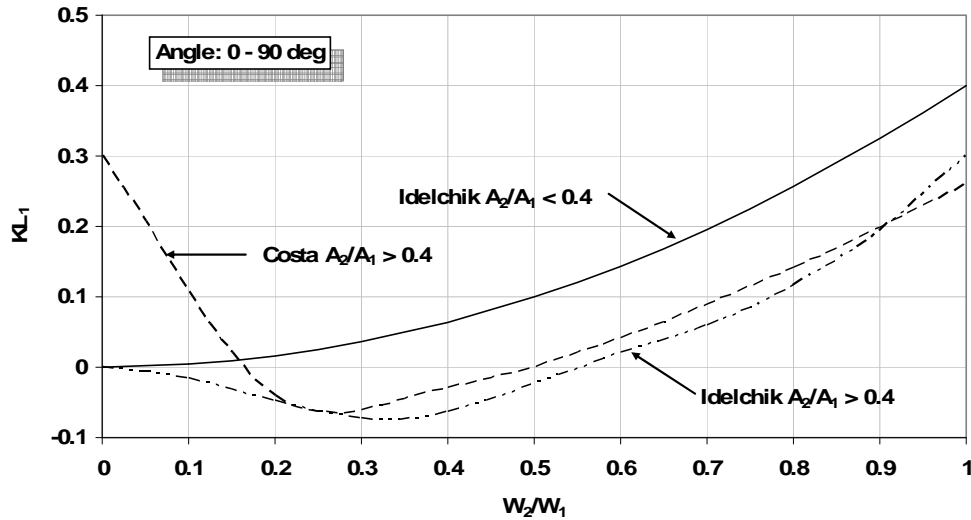
Figure 15: Impact of Flowrate Ratio on Manifold Loss Coefficient in Manifold/Orifice Deceleration – Idelchik [1] & Costa [11]

5.0 INCEPTION OF CAVITATION

As the Reynolds number in the non-cavitation flow regime approaches full cavitation, a fuzzy appearance of the flow at the entrance appears. According to Chaves et al [15] this is thought to be caused by small nozzle inlet imperfections that offer better conditions for cavitation inception. Chaves further states, as Reynolds number continues to increase, more and more cavities become active to increase the extent of cavitation. Another process shown to impact the inception of cavitation at the entrance is the generation of vortices of sufficient strength that the core pressure is at or below the fluid vapor pressure [16, 17]. The vapor bubbles quickly convert back to liquid as they proceed downstream where the local pressure increases. The conversion process of the vapor bubbles to liquid produces implosions producing high amplitude pressure waves in the orifice entrance region. The nearer the operation is to full cavitation the greater the number, and size, of the bubbles and, consequently, the greater the pressure perturbations. These implosions, if they produce sufficient pressure amplitude, are most likely the driving force for hydraulic flip (discussed under Hydraulic Flip, Chapter 9). Ganippa [18] photographed the inception of cavitation and its progression to full cavitation. Fig. 16 clearly shows individual vapor bubbles initially forming, then the formation of the fuzzy region that increases as Reynolds number increases.

19
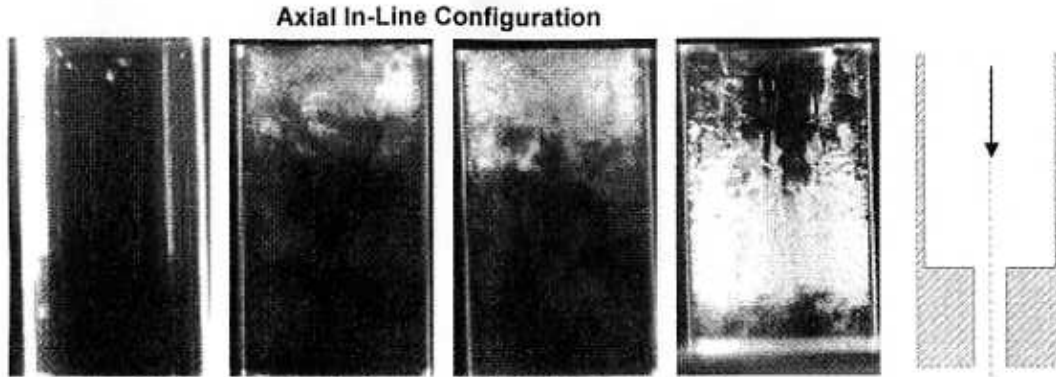
Figure 16: Sequence from Inception of Cavitation to Full Cavitation [18]

It should be noted that regardless of configuration, inception of cavitation occurs; however, the impact on C_d for most cases is small and is detectable only by the use of (1) transparent orifices for photographing the onset of the fuzzy region at the orifice entrance; as well as (2) high frequency pressure transducers near the entrance to record the increase in the magnitude and frequency of the perturbations.

An example of high frequency accelerometer measurements of incipient cavitation in a knife-edged calibration orifice used for determining the cavitation characteristics from valves is shown in Fig. 17 [19]. The abscissa is the cavitation index and the ordinate is noise intensity. These results show that in the non-cavitation flow regime the perturbations are low and begin to rise in amplitude as K_{cav} of about 2.5 indicating the inception of cavitation (their definition of sigma is the same as that of Eq. 29). Note that further decreasing the cavitation index toward full cavitation results in the continual increase in the amplitude of perturbations. Additionally, it is interesting that the amplitude of the perturbations increases with increase in upstream pressure. These results have also been supported by the work of Cla-Val [20].
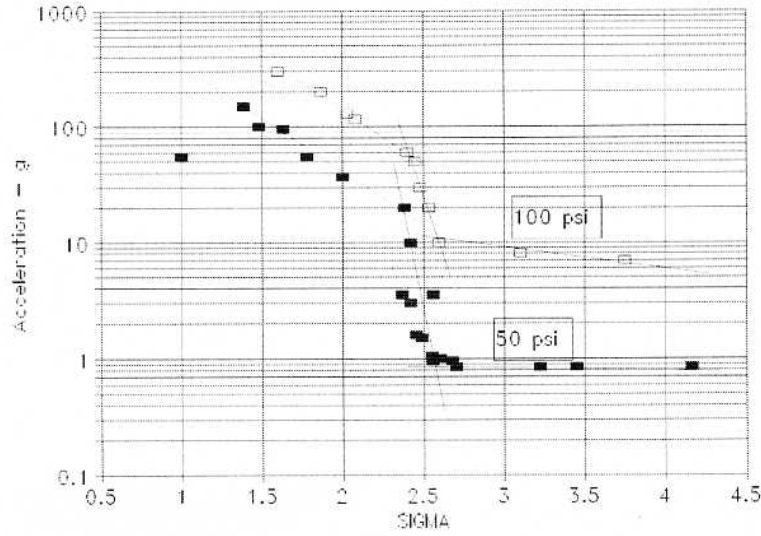
Figure 17: Utah State University Orifice Tests of Valve Incipient Cavitation [19]

5.1 IN-LINE MANIFOLD/ORIFICE CONFIGURATION

The region between full cavitation, as defined previously, and the appearance of the vapor bubbles is defined as inception of cavitation and was previously indicated in Fig.3. Note that both the cavitation index (defined in the Cavitation Flow Regime Section, Chapter 6) and the Reynolds number are plotted against discharge coefficient in Fig.3. This is due to C_d controlled by Re in the non-cavitation flow regime and the cavitation index in full cavitation flow regime. The corresponding value of Reynolds number at initiation of full cavitation is determined by Eq.26.

$$\mathrm{Re}_{IFC} = \frac{C_c D_2}{\mu} \sqrt{2g\rho(P_1 - P_v)} \qquad (26)$$

In the study by Numachi [21], where very short L/D orifices resulting in separation at the entrance were used, he investigated vapor formation due to surface irregularities. His result was based on vapor formation being initiated at a cavitation index (σ, Eq. 29) of ~ 2.5 for a wide range of A_2/A_1. These results were also verified by Gopalan, et al. [22] where cavitation in the core of vortices was observed photographically.

If the cavitation index includes losses (K_{cav} as defined in Eq. 30), then inception of cavitation would vary and be dependent on area ratio as shown in Fig. 18.

21
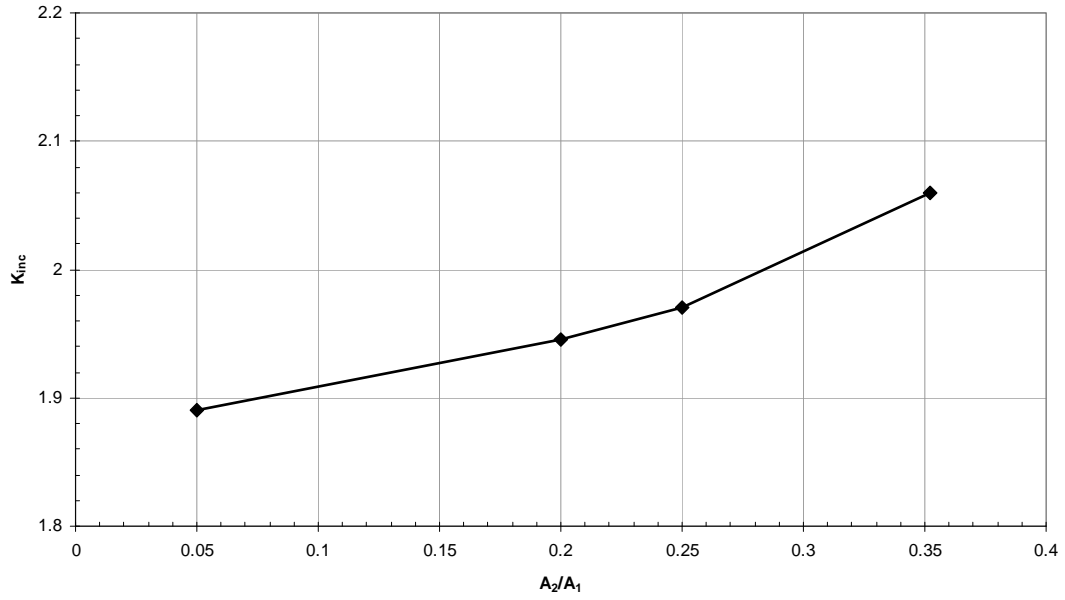
Figure 18: Values of Incipient Cavitation Index vs. Manifold/Orifice Area Ratio

Additional test results from Nurick [2] and Sou [23] of incipient cavitation, together with those of Numachi and Gopalan, Fig. 19, show the similarity between these data, suggesting that for low values of area ratio, the inception of cavitation occurs at about K_{cav} of ~ 2 (i.e., $K_{cav}^{1/2}$ ~ 1.42).

Pearce and Lichtarowicz [24] also studied inception of cavitation (i.e., defined as aeration) and found inception to occur at $K_{cav}^{1/2}$ ~ 1.53, which corresponds to the upper limit of Sou.
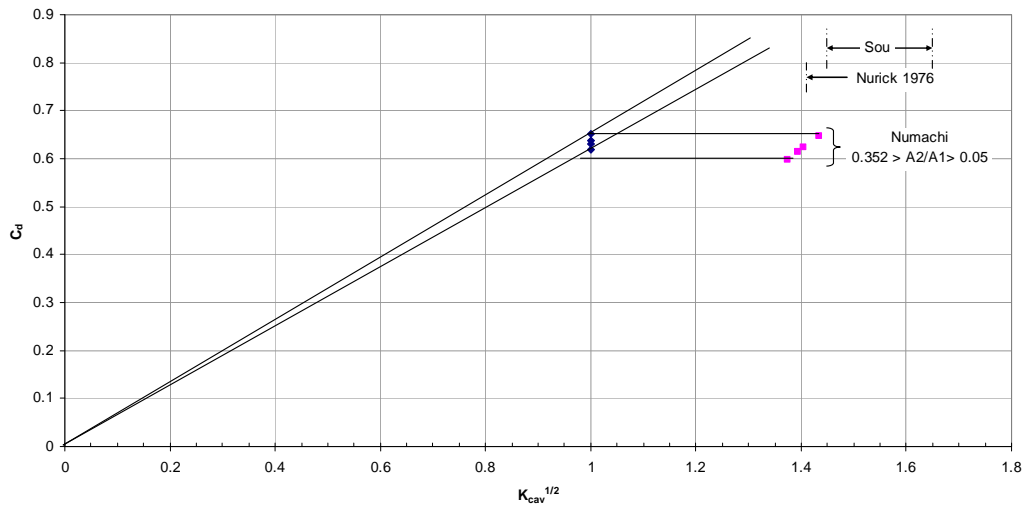
Figure 19: Comparison of Inception of Cavitation for Several Configurations

Based on a value of cavitation index K_{cav} for inception of cavitation of 2, Fig. 18, the corresponding Reynolds number for the inception of cavitation for small area ratios is defined by Eq 27:

$$\text{Re}_{INC} = \frac{C_d D_2}{\mu} \sqrt{g\rho(P_1 - P_v)} \qquad (27)$$

5.2 DEAD HEAD MANIFOLD/ORIFICE CONFIGURATION
While no data exists, it would be expected, based on both the in-line and the approach velocity configurations, that the inception of cavitation characteristics would be very similar.

5.3 APPROACH VELOCITY MANIFOLD/ORIFICE CONFIGURATION
The dynamics of the contraction orifice entrance is considerably more complex with the formation of vortices and significant asymmetric flow. Ganippa [18] also photographed a 90° turning angle approach velocity configuration illustrating that inception of cavitation is also initiated by the formation of individual vapor bubbles at the entrance that grow with increasing Reynolds number. In this case; however, the formation is asymmetric and tends to be initiated on the downstream orifice entrance edge.
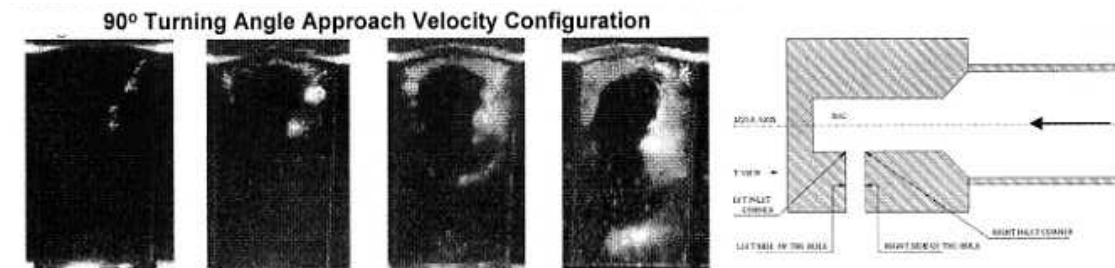
Figure 20: Sequence from Inception of Cavitation to Full Cavitation [18]

5.4 BRANCHING MANIFOLD/ORIFICE CONFIGURATION
While the processes will be similar, it is not known at this time if the contraction orifice characteristics impact inception of cavitation.

23

6.0 FULL CAVITATION FLOW REGIME

6.1 FLOW PROCESSES
In dynamic flow, if a fluid undergoes acceleration, causing local static pressures to drop below the vapor pressure, it will cause the formation of vapor bubbles, clouds, as well as fixed cavities in the low pressure region. In the absence of hydraulic flip in the inception of cavitation flow regime, with further lowering of the downstream pressure, vapor separation at the orifice entrance occurs, and a complete vapor cavity is formed in the region where the local pressure is below the vapor pressure. When this occurs the flowrate becomes fixed at the vena-contracta (i.e., choked, since this is the minimum flow area and is constant) and is no longer impacted by downstream pressure changes. In addition, as the downstream pressure is lowered below that required for initiation of full cavitation, the vapor cavity continually lengthens until the cavity extends to the orifice exit. As the cavity lengthens, the turbulence level of the flow and unsteady flow fluctuations increase due to the implosion of the vapor bubbles where local vapor conditions cannot be maintained.

6.2 CAVITATION INDEX DEFINITION
Cavitation indexes have been defined in several ways. Knapp [25] has defined cavitation index such that losses that occur between the orifice entrance and exit are not included, as shown in Eq. 28.

$$\sigma = \frac{P_2 - P_v}{\dfrac{\rho V_2^{\,2}}{2g}} \tag{28}$$

Nurick [2] utilized a different relationship after Hall [26] which, as shown in Eq. 29, includes all losses.

$$K_{cav} = \frac{P_1 - P_v}{P_1 - P_2} \tag{29}$$

These two definitions are the ones most commonly used in the literature. Other definitions in the literature are just variations of the above or are defined in terms of an intermediate pressure (i.e., at the vena-contracta or reattachment point), as well as substitution of P_2 for P_1 in the numerator in Eq. 29.

The relationship between Eq. 28 and 29 is:

$$K_{cav} = \frac{1}{1 - C_c^{\,2}\sigma} \tag{30}$$

6.3 DISCHARGE COEFFICIENT

6.3.1 In-Line Configuration
When the cavitation index is defined in terms of the overall pressure drop (Eq. 29), all losses from the manifold to the orifice exit are included. Then, utilizing the Bernoulli equation between the orifice inlet and the vena-contracta and the definition of the contraction coefficient (Eq. 21), as well as the cavitation index, the discharge coefficient relationship can be defined as:

$$C_d = \frac{C_c \sqrt{K_{cav}}}{\left[1 + \left(\frac{A_2}{A_1}\right)^2 C_c^{\,2}\left(K_{cav} - 1\right)\right]^{1/2}} \tag{31}$$

In this derivation, the core static pressure was assumed sufficiently close to the vapor pressure at the vena-contracta. The potential error of this assumption is minimal for engineering purposes (i.e., saturated liquid or saturated vapor). Further, it is easily shown that when the area ratio is "small," Eq. 32 reduces to Eq. 32.

$$C_d = C_c \sqrt{K_{cav}} \tag{32}$$

Depending on the allowable error, Eq. 33 can be utilized for area ratios over the cavitation operating range, shown in Fig. 21.
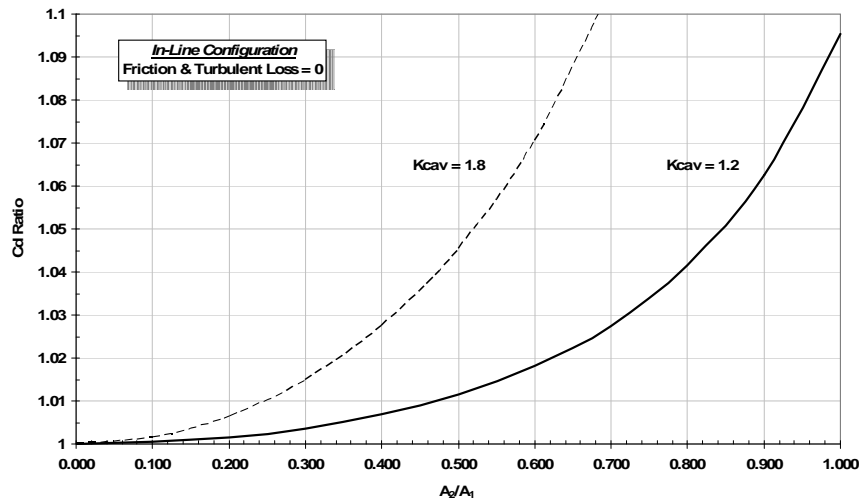
Figure 21: C_d Error Limits Using Eq. 31 vs. Eq. 32

Since the derivation of Eq. 31 and 32 includes all losses between the orifice entrance and exit, the orifice flowrate, which depends on the orifice pressure drop, must be consistent with Eq. 33.

$$C_d = \frac{W}{\rho A_2 \sqrt{\left(\dfrac{2g}{\rho}\right)(P_1 - P_2) + V_1^{\,2}}} \tag{33}$$

V_1 is assumed 0 for in-line configurations.

6.3.2 Dead Head Configuration

For the dead head configuration, since the manifold inlet flow is divided into two streams, the discharge coefficient is defined as:

$$C_d = \frac{C_c \sqrt{K_{cav}}}{\left[1 + \left(\dfrac{A_2}{2A_1}\right)^2 C_c^{\,2}\left(K_{cav} - 1\right)\right]^{1/2}} \tag{34}$$

For small area ratios, Eq. 34 also reduces to Eq. 32.

6.3.3 Approach Velocity Configuration

The discharge coefficient for the approach velocity configuration is identical to that of the in-line configuration, Eq. 32.

6.3.4 Branching Configuration

Using the definition of contraction ratio (Eq. 21), the relationship between area ratio and velocity ratio, and the Bernoulli equation written between the vena-contracta and the orifice exit, the relationship shown in Eq. 35 defines the discharge coefficient.

$$C_d = \frac{C_c \sqrt{K_{cav}}}{\left[1 + \left(\dfrac{V_1}{V_2}\right)^2 C_c^{\,2}\left(K_{cav} - 1\right)\right]^{1/2}} \tag{35}$$

Similar to the in-line configuration when the second term in the denominator is small relative to 1, Eq. 35 reverts to Eq. 32. Lastly, the determination of the actual operating conditions requires the same approach as that discussed for the in-line manifold/orifice configuration.

The error in C_d shown in Fig. 22 maximizes at velocity ratio of 1 where the flow starts to decelerate.
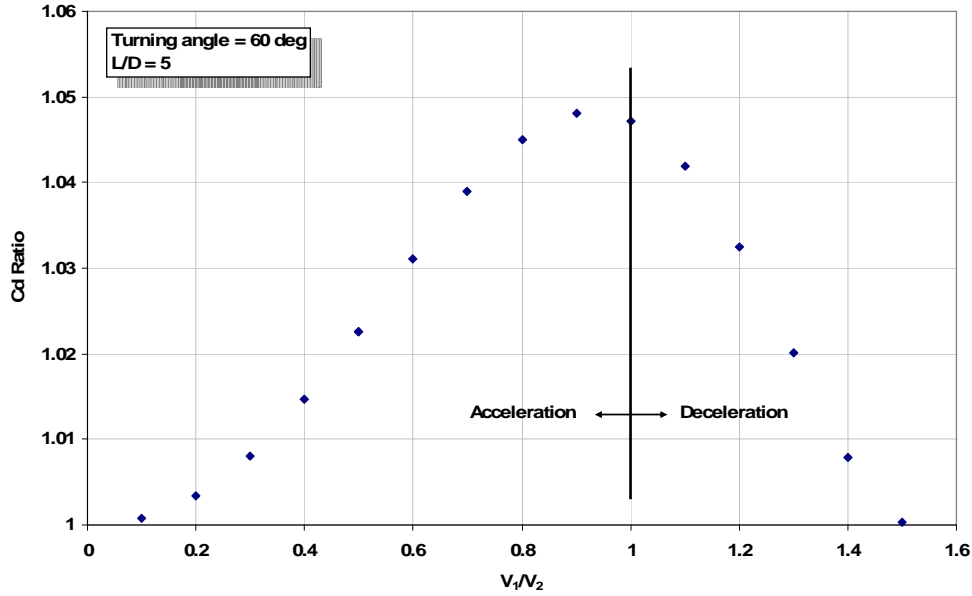
Figure 22: C_d Error Limits (Eq. 6/Eq. 19) vs. Velocity Ratio

6.4 INCEPTION OF FULL CAVITATION

The inception of full cavitation is defined at the intersection of the non-cavitation C_d with full cavitation. Two things simultaneously happen near this condition; the first is that a vapor cavity forms at the orifice inlet edge where the flow separates from the orifice boundary and forms a vena-contracta where the liquid flow area minimizes; then secondly, the flow expands as the local pressure increases until at the cavity reattachment the liquid flow fills the orifice and continues downstream to the orifice exit. At this condition, as stated above, the flow is "choked" where the flowrate is no longer impacted by downstream pressure.

6.4.1 In-Line Configuration

The prediction of discharge coefficient in non-cavitation flow regime is determined for in-line configuration by application of correlations defined in Appendix A. This value of C_d together with C_c defined in Section 4 then defines the cavitation index for inception of cavitation from Eq. 31. Since the non-cavitation loss coefficient is dependent on both Reynolds number and L/D, the inception of full cavitation is not a fixed value. The cavitation index at inception of full cavitation is plotted in Fig. 23 for several L/D at Re $\geq$ 10^4. Note that for each L/D the inception of cavitation is relatively constant until the area ratio is ~0.04 or greater, then drops dramatically.

27
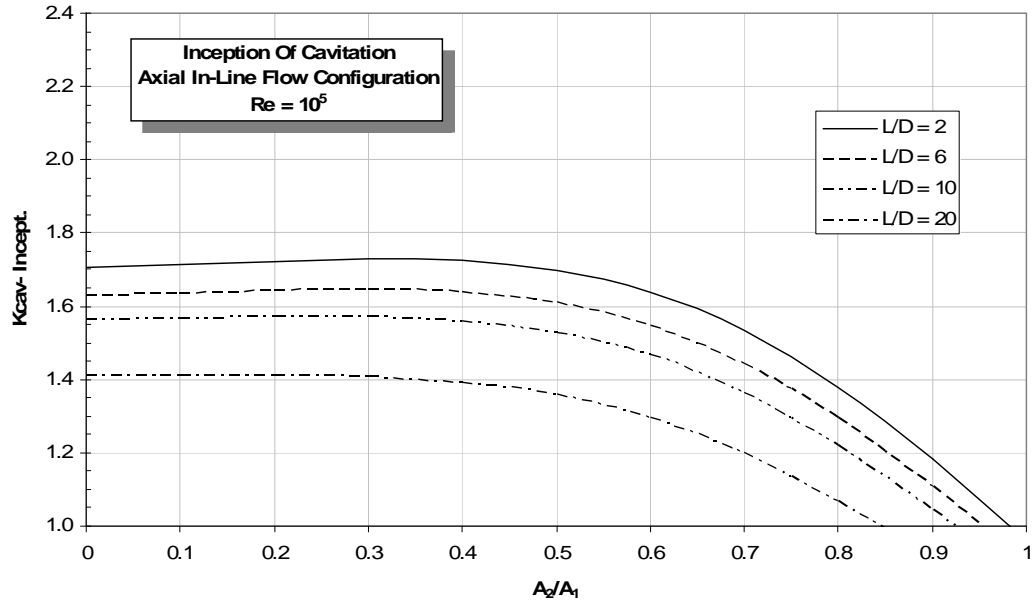
Figure: 23: Full Cavitation Inception for Several Orifice L/D

Reynolds number is also important to inception of cavitation and must be considered in determining the corresponding C_d at inception of cavitation. Experimental data from several published papers [2, 27, 28, and 29], at very low area ratios, is compared with prediction in Fig. 24.
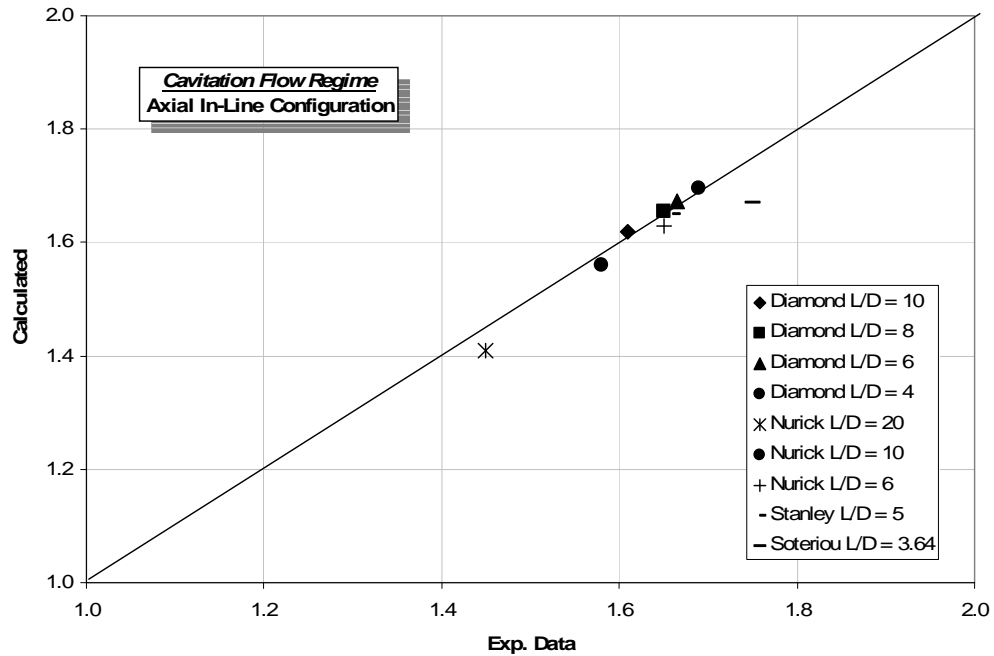
Figure 24: Comparison of Predicted Inception of Cavitation and Experimental Data

This approach to defining the initiation of full cavitation is similar to that proposed by Pearce and Lichtarowicz [24], and the predicted values given in Fig. 23 at small area ratio are also similar.

The comparison with experimental data shown in Fig. 24 is considered excellent, considering that small variations in orifice entrance r/D would result in large changes in cavitation inception. Of particular interest, however, is that inception of full cavitation for axial in-line configurations is dependent on the discharge coefficient in non-cavitation flow, which is also dependent on A_2/A_1, L/D and Re.

The pressure perturbations due to bubble collapse within the contraction orifice also impact initiation of full cavitation. For example, Ramamurthi et al. [30] has shown that both frequency and amplitude of perturbations at the orifice entrance result in a lowering of the discharge coefficient, and as a result, a lowering of the cavitation index where inception of cavitation occurs. This is expected since the C_c will be constant and lowering of the C_d lowers the intersection of the non-cavitation C_d with the cavitation line of slope C_c (Fig. 10 and Eq. 6).

Of further interest is that Pearce and Lichtarowicz [24], who also measured both the amplitude and frequency of disturbances for the region between inception and full cavitation, found: (1) at inception the frequency of disturbances is high, the amplitude low, and occurs in bursts; and (2) as full cavitation is approached, the frequency of disturbances decreases, the amplitude increases, and they are continuous.

6.4.2 Dead Head Configuration
The dead head configuration inception of full cavitation is identical to the in-line configuration.

6.4.3 Approach Velocity Configuration
The approach velocity configuration is identical to the in-line and dead head flow configurations.

6.4.4 Branching Configuration
Inception of cavitation is defined by the same variables as described in the axial in-line configuration. However, for branching flow both the overall loss coefficient and contraction coefficient are now functions of velocity ratio, L/D, and turning angle. The non-cavitation discharge coefficient for branching configuration is determined using Eq.36

$$C_d = \frac{1}{\sqrt{KL + KL_{fr} + 1}} \qquad (36)$$

Then utilizing the value of contraction coefficient based on branching flow, Eq. 25 together with C_d from Eq. 36 defines the value of inception of full cavitation from Eq. 31 or 32.

For turning angle of 60, 90, 120 degrees, and L/D of 5, the impact of velocity ratio on cavitation index at inception of cavitation was determined at constant Reynolds number of 10^5 for the branching orifice configuration, and the results are shown in Fig. 25. Similar curves can be generated for differing Re and L/D. This emphasizes the complexity of defining inception of cavitation since any variable that impacts C_d or C_c impacts the inception of cavitation.
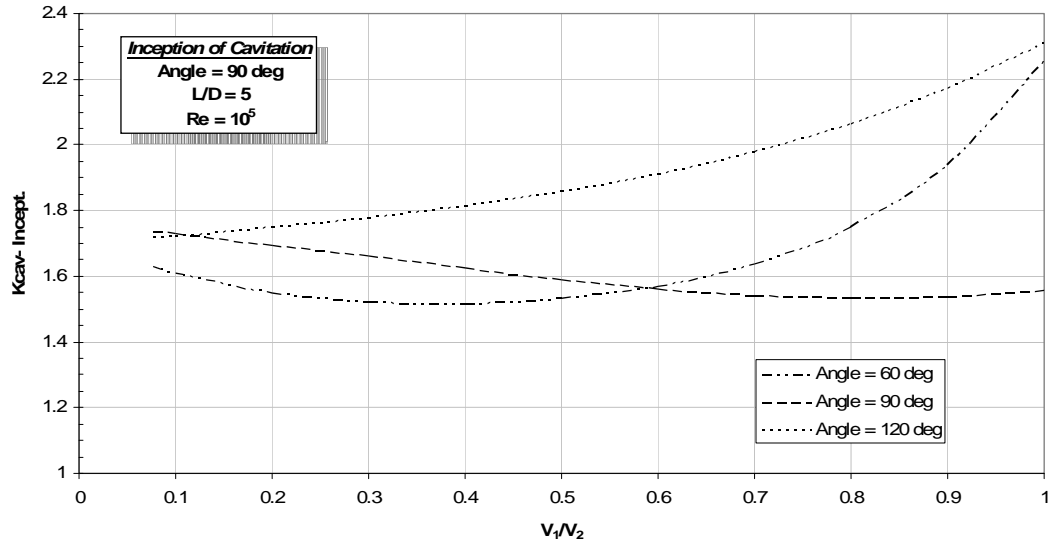
Figure 25: Impact of Velocity Ratio on Inception of Cavitation

In order to verify that inception of cavitation can be predicted, the data utilized in [4] was reevaluated to determine the inception of cavitation; and then the data was corrected using the equations discussed in this report to a common condition and plotted against prediction. Inception of cavitation was defined as where the discharge coefficient starts to deviate from the non-cavitation trend before attaining the constant value of C_c. The result for 90° L/D of 2 and 10 for Re = 10^5 is shown in Fig. 26. The data spread compared with the prediction is well within the data error and verifies that prediction of inception of cavitation can be made with high fidelity.

30
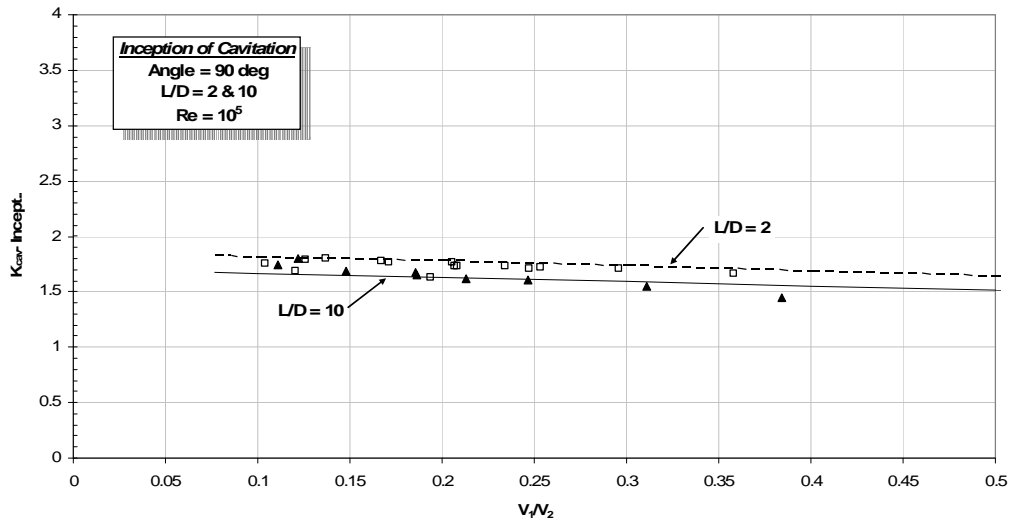
Figure 26: Comparison of Experimental Data with Prediction

If, as discussed for in-line configuration, turbulence at the orifice inlet due to bubble collapse at inception of cavitation is of sufficient magnitude then the inception of cavitation will change. It is hypothesized that for the high velocity cross flow data shown in Fig. 27, the unstable conditions near inception of cavitation are the result of unsteady pressure perturbation at the orifice entrance. Note that once hydraulic flip starts to occur, the flow becomes progressively more stable. The two levels of C_d are probably the transition between perturbation and no perturbation, although data to support this assertion is not available.
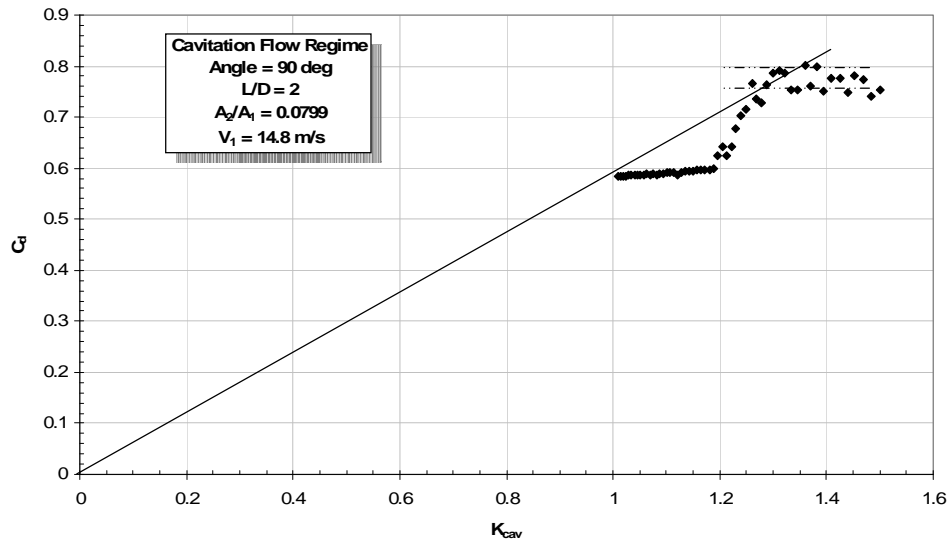
Figure 27: Unstable Flow Characteristics in 90⁰ Branching Flow

6.5 ENTRANCE LOSS COEFFICIENTS

In the cavitation regime, the upstream loss between the manifold and the vena-contracta can be determined, since the pressure, C_c, and velocity can be defined. That together with the total loss measured during testing allows determination of the upstream losses that can be equated to the turning, entrance, and acceleration losses to the vena-contracta. These entrance losses have been assessed and found to be small, since the acceleration process is extremely efficient. This major loss is that associated with deceleration to the reattachment and friction losses downstream. In general, these conclusions have been limited to axisymmetric entrance flow associated with in-line configurations.

6.5.1 In-Line Configuration

It is generally agreed that the entrances losses to the vena-contracta are small for the in-line flow configuration.

6.5.2 Dead Head Configuration

For the dead head configuration, depending on turning angle, the orifice entrance flow can be either axisymmetric or asymmetric. However, over a wide range in cavitation index and turning angle, the entrance losses are still small, as noted in Fig. 28. These levels of entrance loss were noted for upstream pressure between 0.689 - 10.34 MPa.
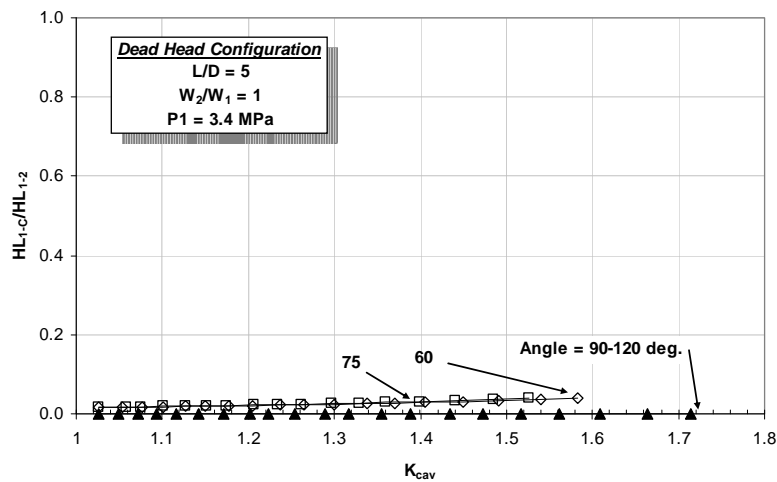
Figure 28: Ratio of Manifold to Vena-Contracta Divided by Total Head Loss for Dead Head Configuration

6.5.3 Approach Velocity Configuration

Although the flow is asymmetric for all flow conditions for the approach velocity configuration, the turning and eddy loss at the entrance was nevertheless small, as shown in Fig. 29. These results suggest that, for flow conditions where all the flow is directed to the contraction orifice, the entrance losses will be between 0 – 5%, depending on cavitation index. It should be noted that this is only true when the orifice entrance perturbations are small (i.e., < 1-5%). As with the dead head configuration, the entrance loss was small over the range in upstream pressure of 0.689 - 10.34 MPa.

32
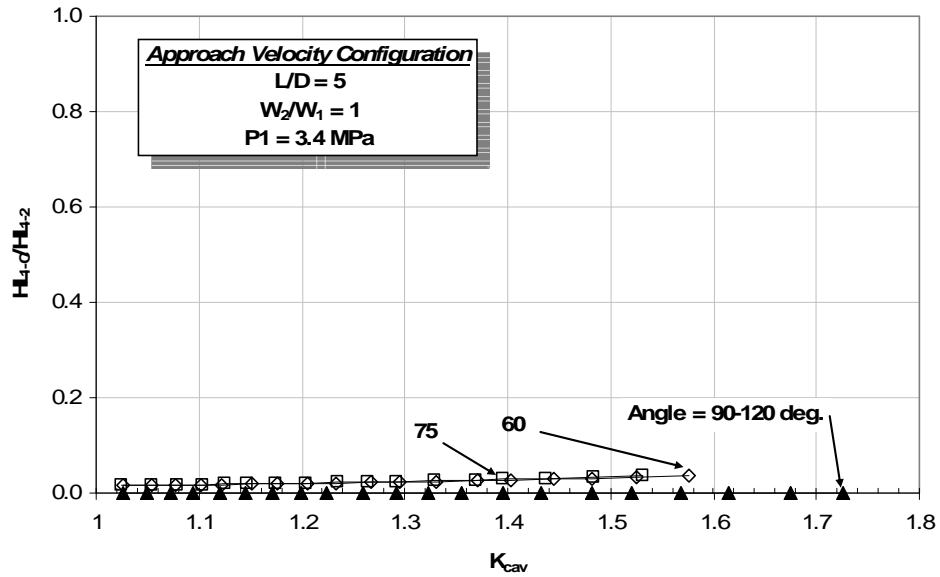
Figure 29: Ratio of Manifold to Vena-Contracta Divided by Total Head Loss for Approach Velocity Configuration

6.5.4 Branching Configuration

For the branching flow configuration, the entrance loss as shown in Fig. 30 is identical to that of the approach velocity configuration, in that the upstream loss is < 5% of the total loss. This is true only for the higher upstream pressures (i.e., 3.45 - 10.34 MPa)
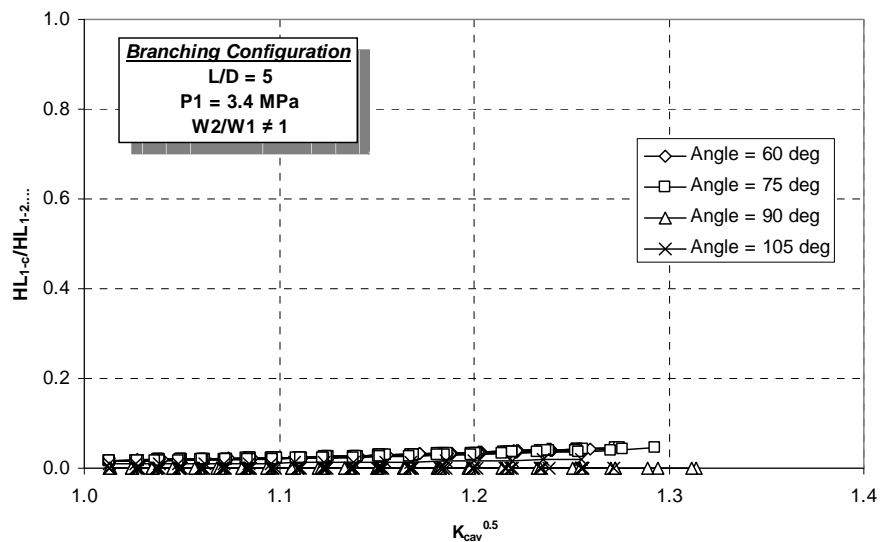
Figure 30: Ratio of Manifold to Vena-Contracta Divided by Total Head Loss for Branching Configuration

For upstream pressure of 0.689 MPa, the entrance loss is dependent on both cavitation index and manifold inlet-to-contraction orifice flowrate ratio, as shown in Fig. 31. This suggests that the turbulence at the entrance is significant and increases with increase in cavitation index as well as decrease in flowrate ratio. Further, these losses are small for 60° turning angle as well as for 105° and 120° turning angle and, in addition, at these obtuse turning angles the impact of flowrate ratio reverses.

A cross plot of flowrate ratio vs. C_d at constant cavitation index (Appendix C), for the 90° turning angle, shows that flowrate ratios > 0.4, C_d is independent of flowrate ratio. However, as flowrate ratio decreases, C_d becomes increasingly sensitive to flowrate ratio. At this time it can only speculated as to the processes controlling its characteristic, but the preliminary conclusion is that it is the result of separation characteristics near the downstream edge of the contraction orifice that result in significant entrance losses.
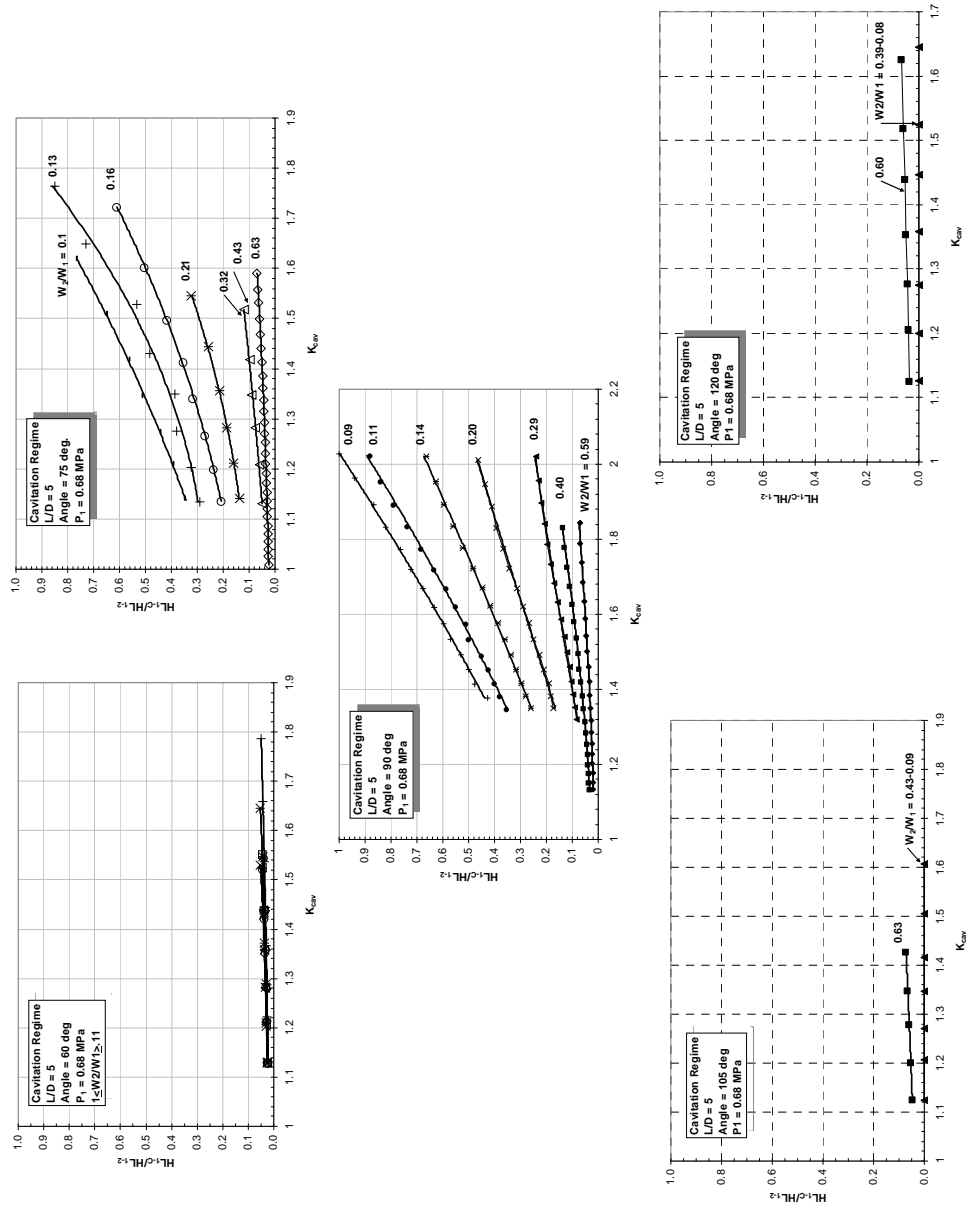
Figure 31: Branching Configuration Entrance Loss – Upstream Pressure 0.689 MPa

6.6 CONTRACTION COEFFICIENT

The coefficient of contraction, as discussed in Section 4, is constant for both non-cavitation and cavitation flow conditions. Consequently, Section 4.2 should be consulted for definitive values for all configurations.

35

7.0 SUPERCAVITATION

7.1 FLOW REATTACHMENT

7.1.1 In-Line Configuration

For inception of full cavitation, the cavity length is relatively constant at about $L_{cav}/D = 0.5$. Then, as bubble/cloud formation begins to form but choked flow cavitation has not been achieved, the bubble region lengthens at a modest rate. At cavitation ($K_{cav} \sim 1.8$) the cavity length begins to rapidly lengthen until the cavity reaches the orifice exit. At this point (i.e., supercavitation), the cavity will remain quasi-attached or separate. If quasi-attached, with further lowering of the cavitation index hydraulic flip occurs in most cases. This process has been well documented, and measurements of the cavity extent have been published in the literature. The recent works of Sato & Saito [30] and Stanley [28] are shown in Fig. 32.
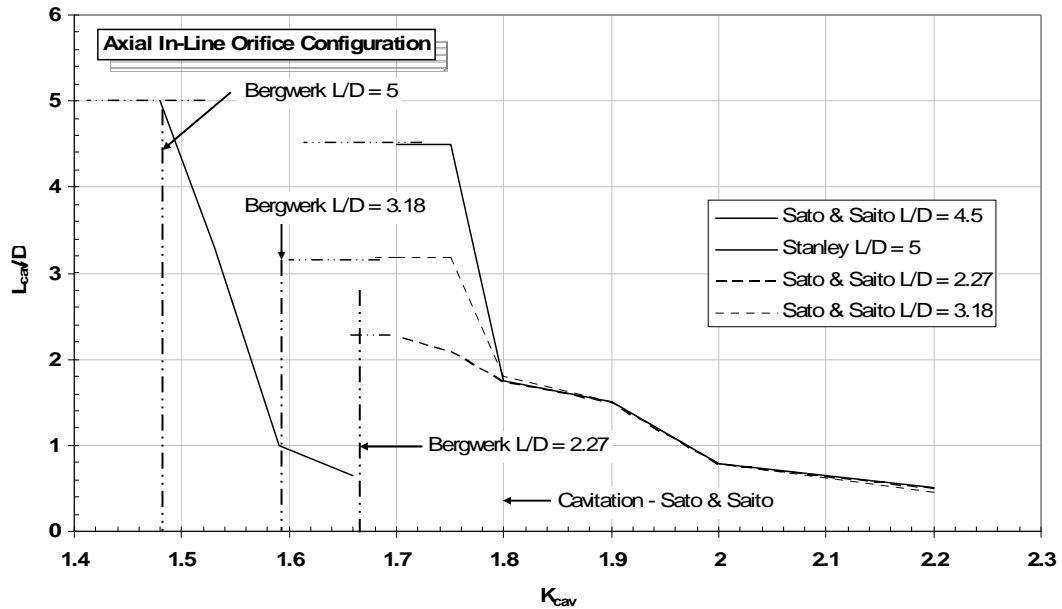
Figure 32: Impact of K_{cav} on Normalized Cavity Length [28 and 30]

The data shown in Fig. 32, where each data set represents a different L/D, clearly illustrates the impact of L/D and supports the above process description. The data also illustrates the operating range in cavitation index before hydraulic flip, Bergwerk [32]. For Sato & Saito [30], the operating range before hydraulic flip appears to increase with increasing L/D. Of interest is that for Stanley [28], at L/D of 5 the separation likely occurred at the onset of supercavitation; while for the Sato & Saito data, hydraulic flip did not immediately occur. The striking difference between the two studies potentially suggests different orifice entrance sharpness or exit finish. It is important to note that the cavity "jump" to the orifice exit occurs with very little change in pressure. This change

has been estimated as ~ 0.00.138 MPa. Therefore, small pressure perturbations downstream of the reattachment point could result in variations in the reattachment point. The attachment and recompression characteristics after choked flow cavitation is attained must change in order to increase the required pressure loss at recompression (i.e., flowrate is constant). It is hypothesized that this is achieved by the vapor cavity shape progressively becoming more abrupt and eventually approaching a backward facing step. The core flow would at some point separate, forming highly turbulent recirculation eddies between the vapor cavity reattachment and liquid reattachment. The degree of separation could account for the increased recovery loss. Turbulent losses due to recirculation eddies at reattachment have been measured by Sato & Saito and He & Ruiz [33]. He & Ruiz report that the dissipation increases as the flow moves downstream and may not be the dominant source of turbulence at the orifice exit.

7.1.2 Dead Head Configuration

Experimental results have indicated similar cavity lengthening as the cavitation index decreases, similar to that for the in-line manifold/orifice configurations. However, to date no measurements have been taken for comparison with the in-line manifold/orifice configurations.

7.1.3 Approach Velocity Configuration

Experimental results have indicated similar cavity lengthening as the cavitation index decreases, similar to that for the in-line manifold/orifice configurations. However, to date no measurements have been taken for comparison with the in-line manifold/orifice configurations.

7.1.4 Branching Flow Configuration

Experimental results have indicated similar cavity lengthening as the cavitation index decreases, similar to that for the in-line manifold/orifice configurations. However, to date no measurements have been taken for comparison with the in-line manifold/orifice configurations.

7.2 ONSET OF SUPERCAVITATION

7.2.1 In-Line Configuration Critical Cavitation

Bergwerk [30] studied the impact of L/D on the cavitation index at supercavitation, and his results and others [30], [23], and [2] are shown in Fig. 33. Bergwerk defined the critical cavitation number as that shown in Eq.37; however, for diesel injector conditions neglected the vapor pressure.

$$K_{crit} = \frac{P_2 - P_v}{P_1 - P_2}$$

(37)

This correlation has been converted to the same basis as Nurick in order for comparison with other data. The relationship is:

$$K_{cav} = K_{crit} + 1$$

(38)
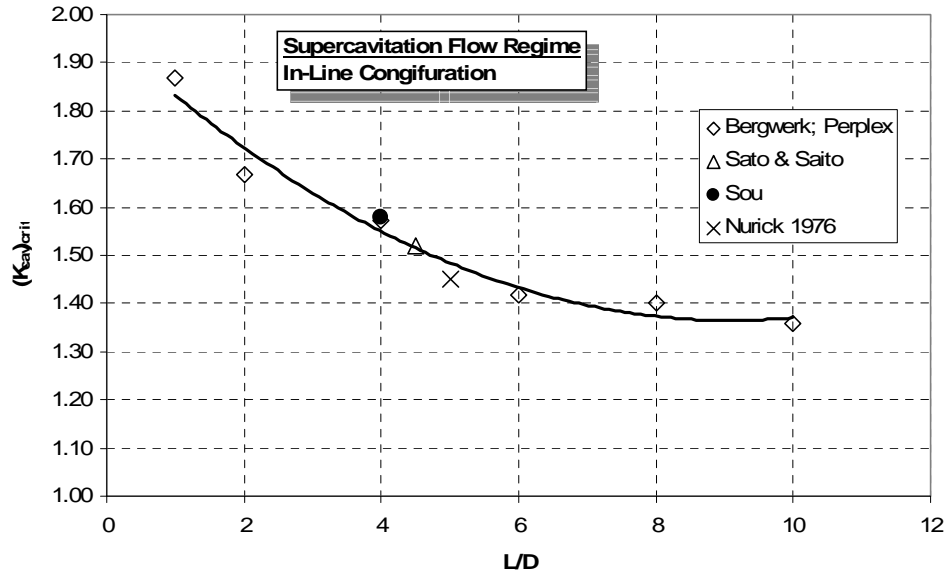
Figure 33: Impact of L/D on Critical Cavitation Index

Bergwerk's correlation defines the cavitation index where the cavity length reaches the orifice exit. Therefore, it is not surprising that this would be related to orifice L/D. For convenience in analysis, the Bergwerk data has been fit to that of Eq. 39.

$$K_{crit} = 1.8696 * \left(\frac{L}{D}\right)^{-0.1429}$$

(39)

As noted in Fig. 32, as the cavity approaches supercavitation it either "jumps" to this attached condition at the orifice exit or experiences hydraulic flip. Both conditions are known to occur. It is interesting that the Bergwerk definition of critical cavitation is the ratio of the adverse pressure force between the orifice exit and the vena-contracta to the overall pressure force, which is typically defined as the "pressure recovery factor".

7.2.2 Dead Head Configuration Critical Cavitation
To date no measurements have been taken.

7.2.3 Approach Velocity Critical Cavitation
To date no measurements have been taken.

7.2.4 Branching Configuration Critical Cavitation
Data from the study published by Nurick, et al. [4] also provides test results of the value of the cavitation index at critical cavitation for a 90° single branching orifice configuration at orifice diameters of 1.19 -2.03 mm. The data is provided in Fig. 34 and is compared with that of Bergwerk [32] for in-line axial manifold/orifice configurations. The values of critical cavitation are not significantly different from those of the in-line

axial orifice configuration for the 90° branching orifice. Critical cavitation values are also provided for L/D of 5 for turning angles of 60°, 75°, 105° and 120°.
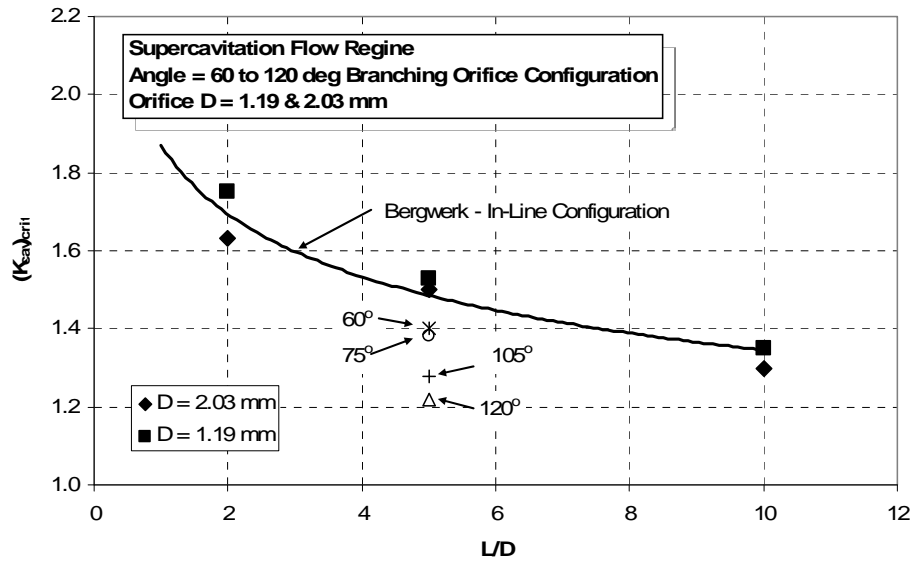
Figure 34: 90° Single Branching Flow Critical Cavitation

While the critical cavitation generally decreases with turning angle, the 90° turning angle appears to deviate. No definitive explanation can be offered at this time.

8.0 ORIFICE EXIT CHARACTERISTICS

The orifice jet conditions at the exit include the jet velocity and mass profiles, the frequency of the vapor bubble collapse and the resulting over pressure, as well as any rotational component of the flow. These flow characteristics are impacted by the differing manifold/orifice configurations (Fig. 1) that result in both axisymmetric and asymmetric orifice flow characteristics. To date there is only limited data available, and the database is insufficient for detailed design purposes. CFD developers have incorporated many of these variables in their codes but lack the precise experimental data necessary for verification of their predictions.

8.1 $W_1 = W_2$ FLOW CONFIGURATION

8.1.1 Orifice Exit Velocity Profiles
There are substantial differences in the flow characteristics at the entrance and throughout the orifice, depending on whether the flow is axisymmetric or asymmetric. At ideal conditions, the axial in-line configuration results in symmetric flow into the orifice and throughout the flow to orifice exit. Asymmetric flow caused by flow turning, or imperfections in the entrance condition, result in a significant difference in the bubble/cloud formation as well as development of a vapor cavity from inception of

39

cavitation to supercavitation, orifice entrance separation, and flow characteristics within the orifice to the orifice exit. When the flow undergoes turning (i.e., approach velocity and branching configurations) to enter the orifice contraction, separation becomes asymmetric at the entrance, resulting in separation on the downstream side of the orifice (i.e., relative to the manifold flow) or upstream side of the orifice depending on both turning angle and manifold/orifice operating condition.

The asymmetry continues throughout the flow to the orifice exit, resulting in highly asymmetric velocity/mass profiles. This is supported by Ganippa [18] with photographs of the cavitation characteristics from the three configurations at varying K_{cav}, Fig. 35. They are: (1) axial in-line, (2) 90° turning angle approach velocity and (3) 80° approach velocity configurations. The above-described flow characteristics are clearly indicated in these pictures of the bubble, cloud, and cavity formation. For the axial in-line configuration, the flow at the exit is axisymmetric, and the jet quality depends on the extent of cavitation. At inception of cavitation, bubble formation is initiated all around the sharp edge entrance, and bubble formation increases until a 360-degree cavity is formed at cavitation (i.e., choked flow conditions) that is attached to the orifice wall. Then the cavity lengthens as the exit pressure is lowered until it extends to the exit. For the approach velocity configurations (80 and 90 degrees), while the bubble formation is initiated at the sharp edge, depending on the turning angle, initial formation of bubbles and clouds occurs on either the downstream or upstream edge of the orifice sharp edge entrance. The clouds and subsequent cavity formation do not completely encircle the orifice and may or may not be attached. At supercavitation the cavities are attached to the wall but still do not completely encompass the entire circumference.
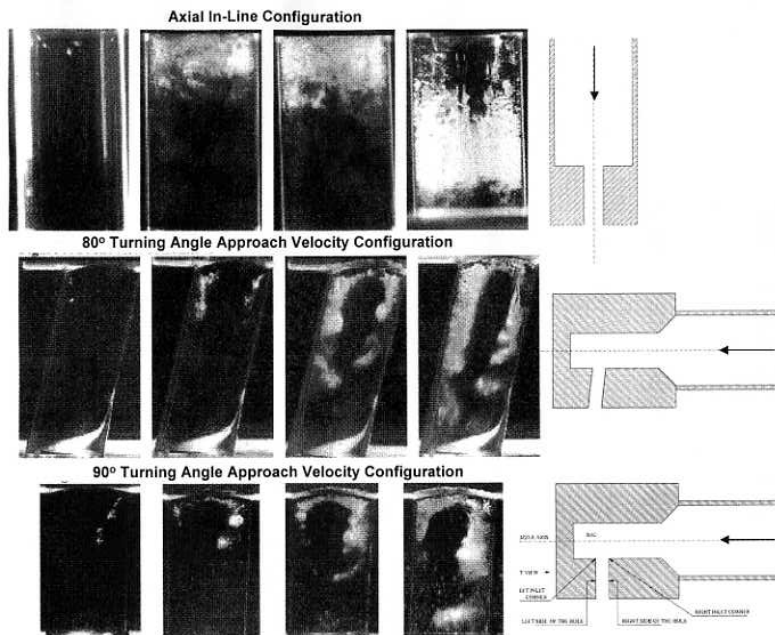
Figure 35: Impact of In-Line Configuration on Cavitation Characteristics [18]

Even with the asymmetric behavior or the flow and significant differences in cavitation formation, as qualitatively indicated in Fig. 35, the overall flow characteristics as shown in Fig. 36 follow the one-dimensional model proposed in Eq. 6. However, turning angle does impact C_c, initiation of cavitation, as well as flow sensitivity to hydraulic flip. A summary of the impact of turning angle on cavitation characteristics for the Approach Velocity configuration is included in Appendix B.
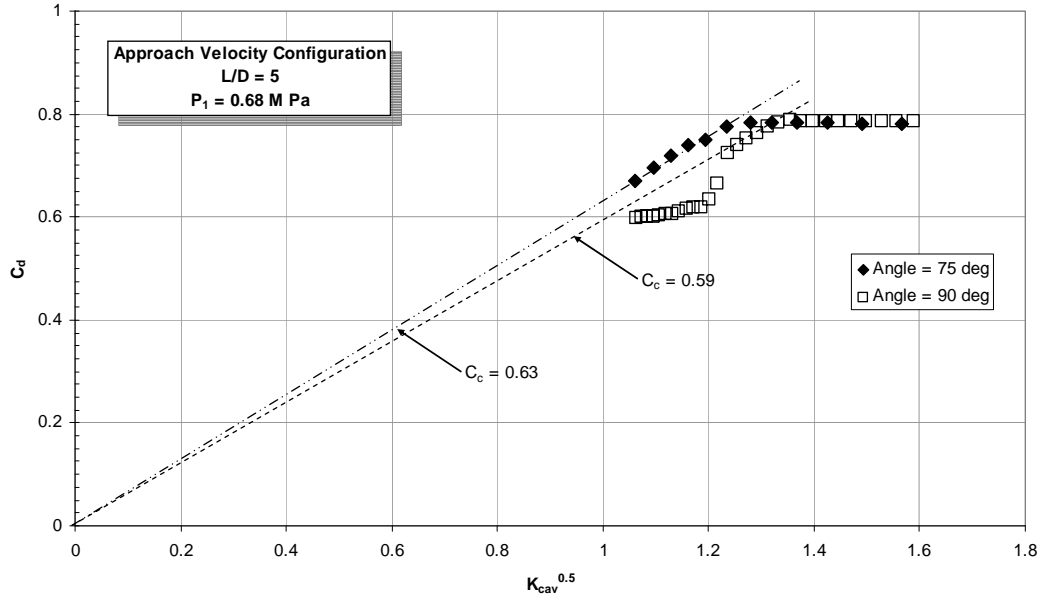
Figure 36: Flow Characteristics In-Line Approach Velocity Configuration

Stanley et al. [28] have measured the velocity profile near the orifice exit from an axial in-line configuration at several values of cavitation index. Stanley's results, Fig. 37, show that the velocity profile is not completely uniform and that the uniformity decreases as the cavitation index decreases. The authors attribute this to slight manufacturing imperfections in orifice symmetry. This highlights the sensitivity of orifice exit velocity characteristics to orifice entrance manufacturing tolerances.
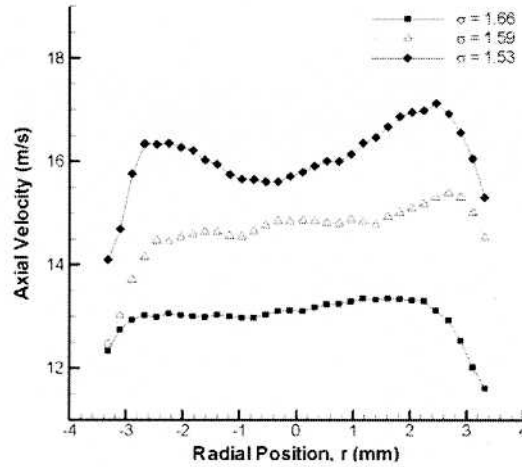
Figure 37: Orifice Exit Velocity Profile for differing Cavitation Index [28]

As noted by Sou et al. [23] in Fig. 38, the lateral component of velocity (U) in cavitation, $\sigma = 0.78$, is near zero but increases significantly in supercavitation $\sigma = 0.65$. Therefore, the flow is directed toward the side wall, which is also suggested by Stanley [28].
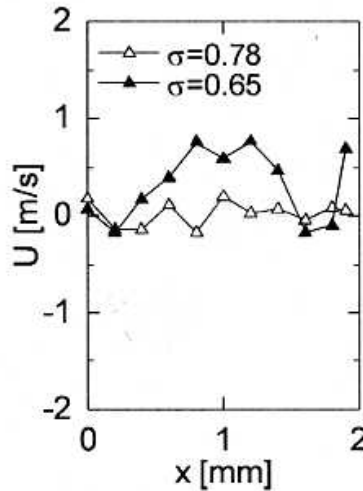
Figure 38: Orifice Exit Velocity Profile for Differing Cavitation Index [23]

The general conclusion is that all in-line configurations have some asymmetry in orifice exit velocity profile and that the asymmetry increases with a decrease in K_{cav}. No velocity profile measurement data is currently available for the approach velocity configuration; however, the photographs of Ganippa, Fig. 35, strongly suggest that the exit non-symmetric flow conditions will be significantly greater.

42

8.1.2 Orifice Exit Turbulence Intensity and Pressure Perturbation
Of particular interest is the disappearance of the bubbles and clouds as the flow proceeds
downstream. This is the result of the local static pressure increasing to a condition that
the bubbles and clouds must convert back to a liquid. This process results in collapse of
the vapor, resulting in significant pressure perturbations of turbulence intensity leading to
unsteady flow conditions. In supercavitation, pressure perturbations due to vapor
bubble/cloud collapse at the orifice exit, causing an unsteady oscillation in the back
pressure; the frequency depending on the mean rate of bubble/cavity collapse rates at the
orifice exit. Measurements have shown that these perturbations result in frequency and
overpressure that are a function of the cavitation parameter and length of orifice; Tamaki
et al. [342], Sato & Saito, Sou, and Zajac [35]. The frequency of the pressure oscillations
as measured by Zajac (for 90-degree Approach Velocity configuration) and Sou et al.
(axial in-line configuration) are reported as between 1-4 KHz.

Sou et al. results, Fig. 39, show that the impact of cavitation index is similar to the
velocity profile in that as cavitation index decreases, the turbulence intensity increases.
Note that the flow regime for σ = 0.78 is cavitation, and 0.65 is in supercavitation. In
addition, although these results are for an axial in-line configuration, the lateral
turbulence intensity is significantly greater toward the right side wall. Again, this is
hypothesized by the author as the result of imperfection in manufacture at the orifice
inlet.
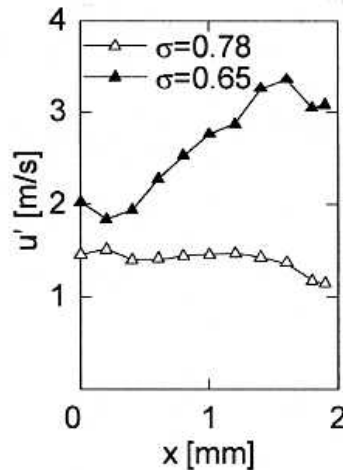
Figure 39: Impact of Cavitation Index on Turbulence Intensity at Orifice Exit [23]

Sou further states that, based on Fig. 40 results, the strong turbulence intensity reaches
the orifice exit only in supercavitation. Sou, however, does not provide any comment on
the magnitude of the pressure perturbations.
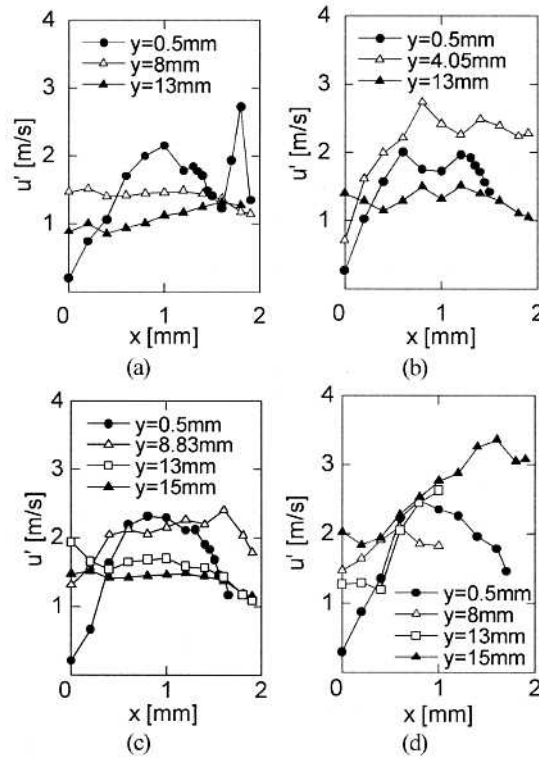
Figure 40: Orifice L Turbulence Intensity at different Cavitation Flow Regimes [23]

He & Ruiz [33] measured the turbulence intensity along the orifice length and found that it is higher after the vapor region in the liquid reattachment region. Their results, shown in Fig. 41, for the orifice centerline flow show the highest turbulence intensity at about 38 mm; then it decreases as the flow proceeds to the exit. Note the difference in turbulence level between non-cavitation and cavitation.
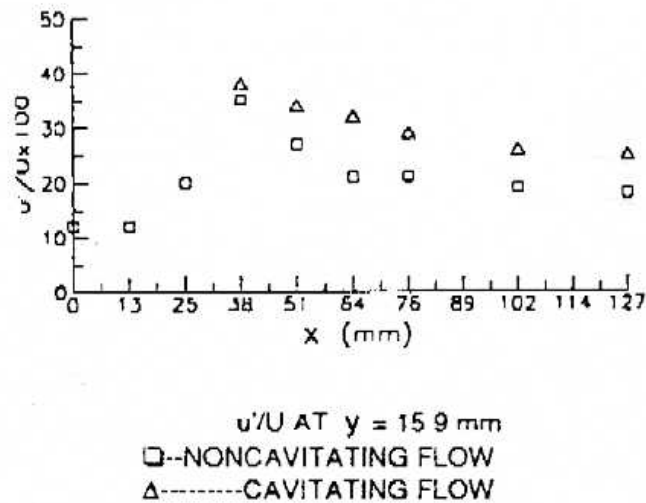
Figure 41: Comparison of Non-Cavitation & Cavitation Turbulence Intensity [33]

Koivula's [36] results show that, due to shock waves produced by the collapse of vapor cavities, the frequency of oscillations decreases from 8 KHz at inception of cavitation to ~900 Hz at supercavitation, and the overpressure increases significantly. In addition, Koivula data, Fig 42, shows that at non-cavitation the pressure perturbations and frequency at incipient cavitation are low and increase markedly as, what he states as "developed cavitation," which in all probably is supercavitation. The maximum overpressure measured was ~ 9 bars (~ 0.88MPa). Even higher shock pressures from bubble collapse have been measured by Takahashi [34], approaching 27.2 MPa.
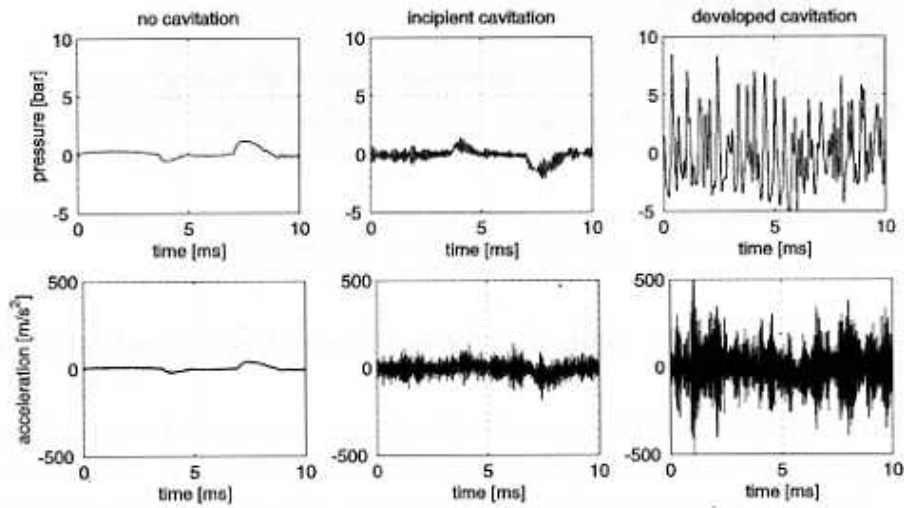
Figure 42: Bubble/Cavity Collapse Pressure and Frequency [36]

These results strongly suggest that bubble/cavity collapse at the orifice exit can cause perturbation of sufficient magnitude to cause the attachment point to move upstream; the amount depending on the over pressure. Further, this will be periodic with the collapse frequency. It would be expected that the pressure requirement would be greater than that required to move the attachment point to the orifice exit. This process was first reported by Pearce and Lichtarowicz [24] and confirmed by Chaves [15] where both researchers found the flow oscillating between non-cavitation and cavitation.

Zajac [35], building on the pioneer work by Rupe [38], measured the stagnation pressure and turbulence intensity in the free jet 5 orifice diameters downstream of the orifice exit. The measurements of Rupe with axial in-line configurations show that at this free stream L/D, the change in these parameters between the orifice exit and 5 diameters is minimal and therefore a good representation of the exit conditions. Fig. 43 provides Zajac's centerline stagnation pressure and turbulence ratios as a function of orifice L/D for the Approach Velocity branching configuration (see inset in Fig. 43). These results show that for L/D > ~25 the centerline stagnation pressure ratio and turbulence intensity are constant.
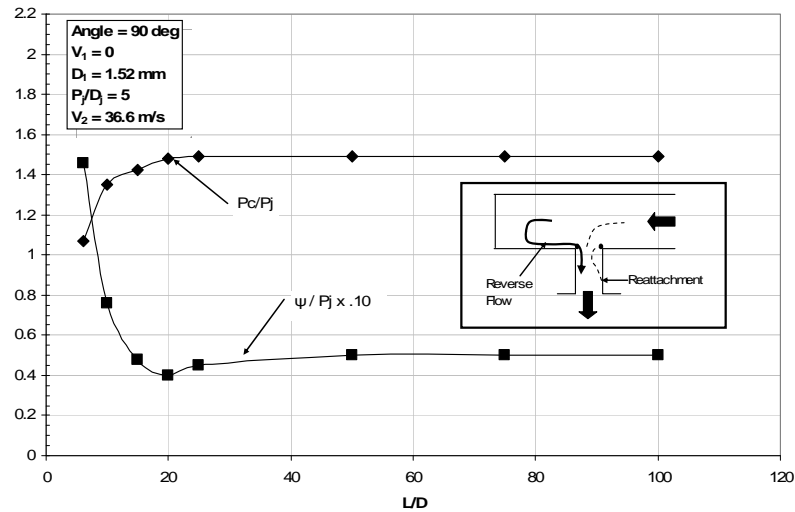
Figure 43: Cavitation Flow - Approach Velocity Orifice Configuration [35]

It is clear from the above discussion that the details of the two-phase flow and implosion characteristics are incomplete at this time. They simply indicate its existence and that the potential impacts are significant. There is, however limited data for comparison of CFD simulation predictions.

In addition, unsteady behavior has also been observed in branching flow configurations at high cross and orifice flow velocity in the data of [4]; discussed later in this Report (i.e., Branching Orifice Configuration, Section 10.2)

8.1.3 Orifice Exit Vortex Characteristics

It has been established that vortex motion is introduced in both the orifice entrance and potentially in the recompression region. However, little definitive data is available to describe vortex strength and angular velocity vectors sufficient for prediction. Photographs from Soteriou [16] for the axial in-line configuration did not show any secondary flows producing vortex motion at the orifice entrance, while for the unequal miter and Approach Velocity type configurations, significant vortex motion occurred. The results, while illustrating that vortex motion does occur, presented no measurement data. Sato & Saito [30] have shown that at the reattachment point there is considerable eddy generation producing its own reverse flow characteristics as well as lateral velocity components that result in vortex motion. This velocity component is close to the mean velocity in the orifice throat. If this vortex maintains to the orifice exit, then a swirl component to the exit jet will occur.

He & Ruiz [33] provide experimental data of mean velocity components throughout the orifice length. Fig. 44 shows results illustrating the difference in mean velocity before and after the reattachment. In this case there is little difference; however, note the lateral component in cavitation. Although the vortex strength is small, it does exist.

46
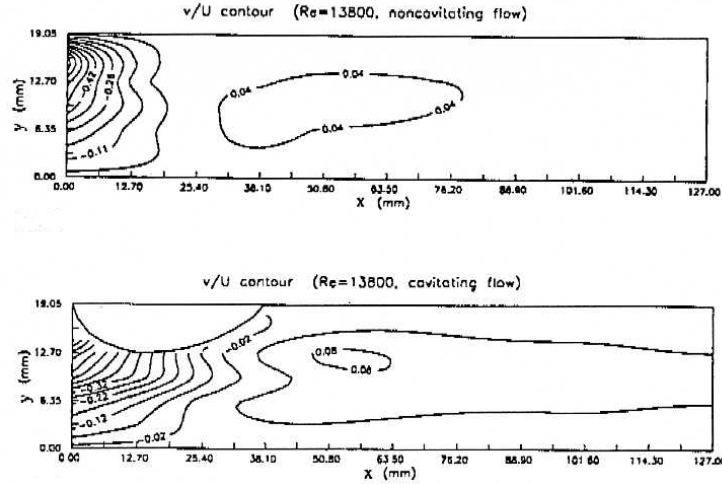
Figure 44: 2-Dimensional Contours of Mean Velocity in Orifice [33]

8.2 W₁ ≠ W₂ CONFIGURATION

Measurements of orifice exit jet characteristics for branching flow in the cavitation flow regime are almost nonexistent. The only data that is available defining the velocity profile is related to the T-Junction configuration [35], where all passages are of the same diameter. Consequently, the flow entering the branching orifice is decelerating at all conditions.

8.2.1 Exit Jet Velocity and Mass Profile

No experimental data exists for branching flow configuration.

8.2.2 Orifice Exit Turbulence Intensity and Pressure Perturbation

Zajac [35] also studied the impact of L/D on turbulence intensity for a 90° branching orifice configuration. Turbulence intensity measurements over a range in velocity ratio for L/D's between 6 and 25 are shown in Fig. 45.
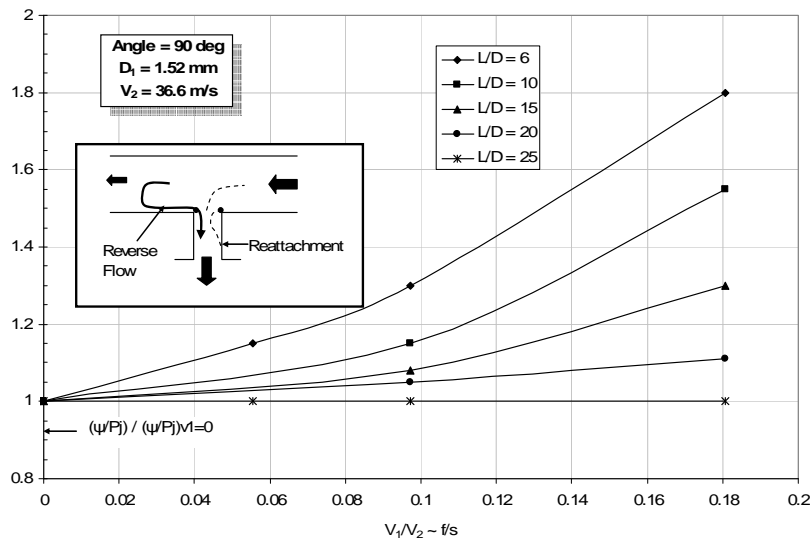
Figure 45: Normalized Turbulence Intensity vs. Cross Velocity for Several L/D [35]

47

For these tests the orifice velocity was maintained constant at 36.6 m/s, resulting in the variation in velocity ratio. It is apparent that both velocity ratio and L/D are significant independent variables in the generation of turbulence intensity at the orifice exit.

The data in Fig. 46 shows an asymmetric profile that maximizes on the downstream side, indicating that for these conditions the manifold/orifice entrance separation is occurring on the upstream side of the entrance.
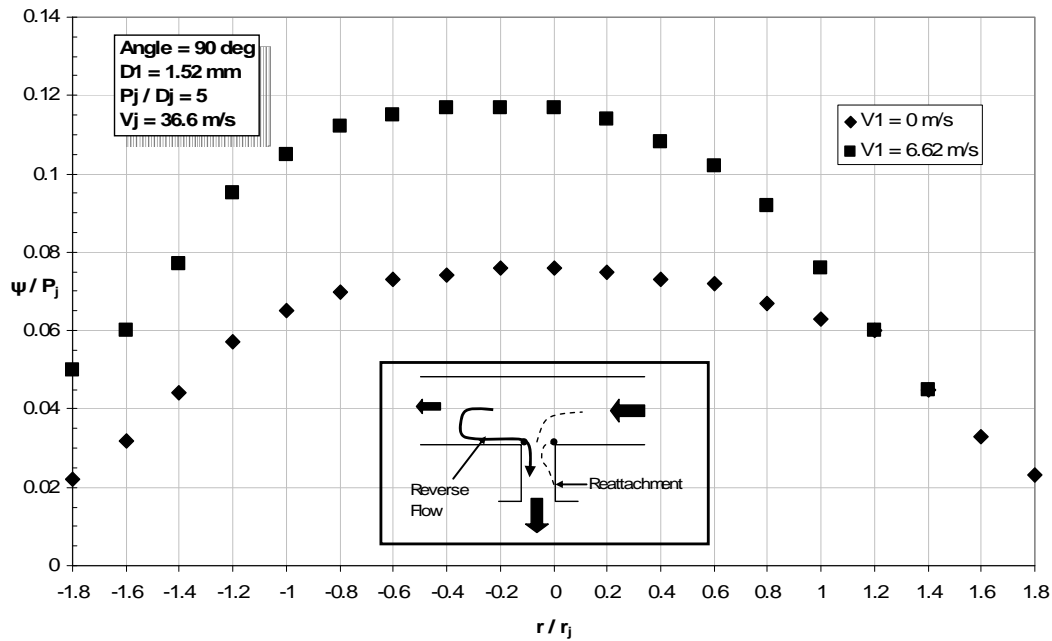
Figure 46: Turbulence Intensity vs. Radial Location at Two Cross Velocities - L/D = 10, $W_2/W_1 = 0.86$ [35]

8.2.3 Orifice Exit Vortex Characteristics
No experimental data exists for branching flow configuration.

9.0 HYDRAULIC FLIP

Hydraulic flip can and does occur in only three flow regimes: (1) non-cavitation, (2) within the inception of cavitation to inception of full cavitation, and (3) at or within the supercavitation flow regime. Once full cavitation is achieved and before reaching supercavitation, hydraulic flip does not occur. However, predicting the actual occurrence of hydraulic flip in either the non-cavitation or cavitation flow regime has not to date been achieved with any degree of certainty.

While mechanisms for hydraulic flip in various flow regimes have been postulated, actual prediction is currently problematic. This difficulty is partly the result of the complexity of the flow characteristics that currently are not mathematically described to a degree sufficient for direct application, despite the fact that the processes are considerably different in each of these flow regimes and irregularities in the surface at the orifice entrance. It is, therefore, not surprising that no single model can describe the extent of hydraulic flip. Due to the lack of detailed process data, the prediction of hydraulic flip is currently limited to an indication of where hydraulic flip might occur, not that in fact it will.

The following discussion, therefore, attempts to provide guidelines for each manifold/ orifice configuration where hydraulic flip is likely to occur, as well as design and flow conditions where it is unlikely that hydraulic flip will occur.

9.1 IN-LINE CONFIGURATION

The largest single body of experimental data for in-line manifold/orifice configurations is that of Diamond [27]. In order for direct comparisons to be made with other studies, Diamond's data was first reevaluated to determine if it conformed to the cavitation model of Nurick [2]. Typical results from Diamond's published results for L/D = 10 and orifice size of 2.37 mm (largest orifice size evaluated by Diamond) for four different fluid combinations are shown in Fig 47.
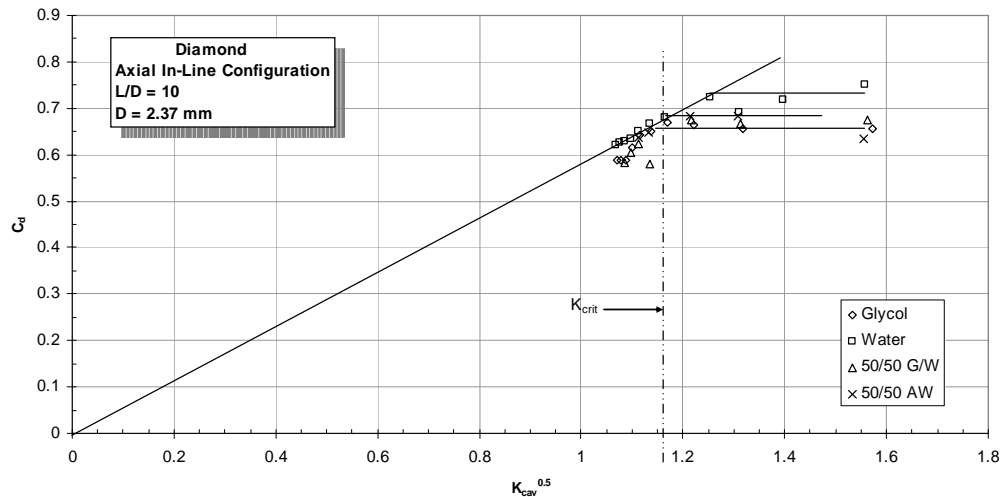
Figure 47: Cavitation Characteristics for Several Fluid Combinations [27]

In Fig. 48 the data for the smallest orifice size evaluated by Diamond is also shown (0.787 mm). In both cases the data shows that, for water, where the K_{IC} is clearly higher than K_{crit}, no hydraulic flip occurs, and the data conforms to the Nurick [2] relationship.
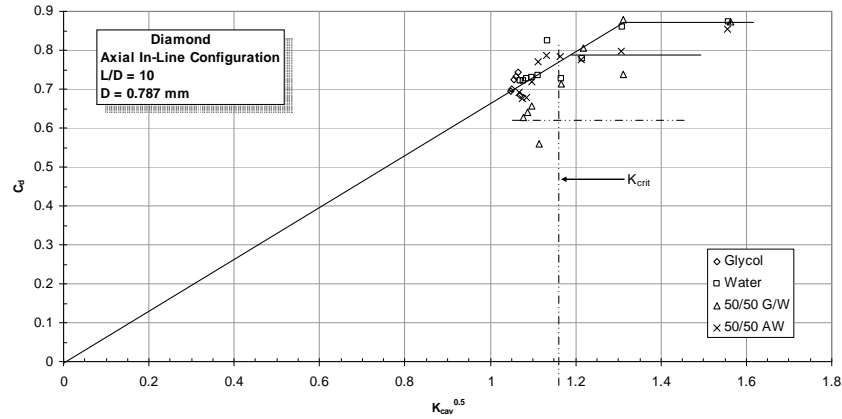
Figure 48: Cavitation Characteristics for Several Fluid Combinations [27]

What is difficult to assess is why the discharge coefficient in non-cavitation varied with fluid type, although the Reynolds number was always $> 10^4$ where it should be constant. In fact the C_d in almost all cases dropped to at or below the K_{crit} value. At this condition hydraulic flip appears to have occurred at or below the K_{crit}.

The lowering of the non-cavitation flow discharge coefficient, in the case where the orifice configuration remains identical, can only occur as a result of changes in the entrance conditions such as "partial' hydraulic flip (Soteriou [29]), where separation occurs on only one side of the orifice; or the Re number reaches the non-cavitation separation criteria (Bergwerk [32]). Partial hydraulic flip is known to occur in both non-cavitation and cavitation flow regimes. However, for the Re of this study no hydraulic flip would be expected to occur at L/D = 10.

In the case where partial hydraulic flip occurs in the non-cavitation flow regimes, it is still possible that this condition will remain as cavitation is approached wherein, since K_{IC} is ≤ than K_{crit}, full separation can occur at or below this value. Further note that for the 0.787 mm data for water, the discharge coefficient increases to a value of 0.87, which is higher than that predicted by accepted relationships; and further that the contraction coefficient also increases from 0.58 to 0.67. These characteristics have also been noted by Ramamurthi [30] in his study of hysteresis. The cause for this lowering of discharge coefficient for different orifice sizes could occur if the entrance roundness for the smaller orifice were increased.

Since the water data conforms to both the [2] criteria for cavitation and the non-cavitation discharge coefficient characteristics, only the Diamond water data is considered further for a general correlation of hydraulic flip in cavitation. Factors that impact the non-cavitation discharge coefficient characteristics (i.e., entrance roundness, partial or

complete hydraulic flip in the non-cavitation) other than L/D are considered as mitigating at this time. Water data for D = 2.37 mm diameter orifice with varying L/D are shown in Fig. 49.
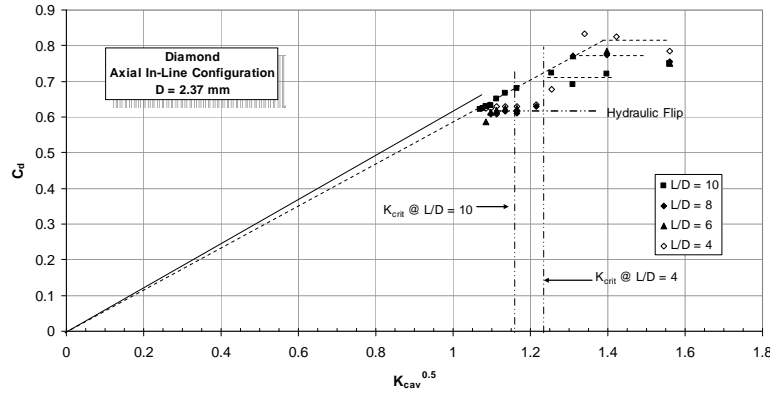
Figure 49: Impact of L/D on Hydraulic Flip Characteristics [27]

The C_d characteristics as a function of L/D in non-cavitation are consistent with published correlations; however, the contraction coefficient is slightly lower than predicted but is within experimental error. For all L/D's where hydraulic flip occurs, it occurs at K_{crit} consistent with the data of Bergwerk [32].

FLUENT utilizes Eq. 40 to predict hydraulic flip in the supercavitation flow regime.

$$K_{HF} = 1 + \frac{1}{\left(1 + \dfrac{L}{4D}\right)\left(1 + \dfrac{2000}{\mathrm{Re}_h}\right)e^{70r/D}} \qquad (40)$$

FLUENT notes that for r/D > 0.05, hydraulic flip is deemed impossible and K_{HF} = 0. However, the source or derivation of this relationship is unknown. For Re = 10^4, r/D = 0, the K_{HF} for various L/D in addition to Bergwerk K_{crit} are predicted to be:

Table 1: K_{HF} for Various L/D Predictions

L/D	K_{HF}	K_{crit}
4	1.42	1.53
6	1.33	1.45
8	1.28	1.39
10	1.24	1.35

For this correlation, hydraulic flip always occurs below the critical cavitation, as defined by Bergwerk. The issue with this correlation is that hydraulic flip is always predicted to occur, even for L/D = 20 where no hydraulic flip occurs. Obviously a limit should be indicated where hydraulic flip will not occur. It should be noted, however, that for large L/D the predicted value of K_{HF} approaches 1, which by definition is considered separated.

While hydraulic flip is mentioned in numerous publications, little to no data is available where the above-mentioned variables have been systematically varied. A summary of several studies available in the literature that cover a wide range in L/D and orifice size is provided in Table 2. It is clear from Table 2 that the data is lacking to complete the matrix; and, further, it is obvious that this information can only be used as a guideline. One of the major issues in interpretation is when the measured C_d varies considerably in the non-cavitation flow regime contrary to that predicted by Lichtarowicz for $Re \geq 10^4$. This anomaly appears more often for small orifice sizes where C_d values are 0.7 consistent with PHF. Anomalies also occur due to local entrance irregularities and minor entrance roundness as well as both orifice entrances pressure perturbations, ΔP, frequency and hysteresis related to startup process and flow variation procedure.

Table 2: Occurrence of Hydraulic Flip - In-Line Manifold/Orifice Configurations Non-Cavitation Flow Regime

SOURCE	D ~ mm	L/D							
		2.14	3	3.64	4	6	8	10	20
Nurick [2]	3.18					No HF		No HF	No HF
Diamond [27]	2.37				No HF	No HF	No HF	No HF	
	1.78				No HF	No HF	No HF	No HF	
	1.51				No HF	No HF	No HF	No HF	
	1.51				PHF	PHF	THF	THF	
	1.32				PHF	PHF	THF	THF	
	1.02				PHF	PHF	THF	PHF	
	0.787				PHF	PHF	THF	?	
Gelalles [47]	0.635	THF							
	0.508		PHF						
	0.381		PHF*						
Soteriou [29]	0.279			No HF**					

* L/D = 3.3 ** Fluid Oil

In overall terms, Table 2 shows that both the orifice diameter and L/D are important variables as well as orifice entrance irregularities (i.e.,partial hydraulic flip (PHF)). For a "perfect" entrance design, the inlet flow would be axisymmetric, resulting in total hydraulic flip (THF); however, the large amount of data showing PHF suggests achieving a "perfect" entrance is difficult to realize in practice. It appears that for large orifice sizes -- sizes greater ~1.52 mm -- no hydraulic flip occurs in the L/D range of 4 to 20. No data is available for shorter L/D's. The process of PHF is not well understood in terms of the variation of C_c with Re number and the stability of the separation region. As noted in the sketch, Fig. 50, the flow separates from one side, while the opposite side still retains the liquid separation recirculation cavity with a vena-contracta. Consequently, it would be expected that the C_c for PHF would be < THF. This could also increase losses, thereby lowering the C_d.
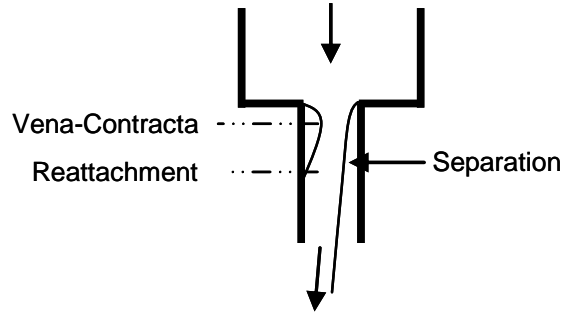
Figure 50: Sketch of Partial Hydraulic Flip (PHF) Characteristics

The data summarized in Table 2 indicates that hydraulic flip in the cavitation flow regime is not random but ordered relative to both geometry and operating conditions. Further, although not indicated in Table 2, according to Ramamurthi [30] when the turbulence intensity due to bubble collapse at the entrance to the orifice results in an over pressure that reduces the discharge coefficient sufficient to result in $K_{IFC} < K_{crit}$, then hydraulic flip will occur. It should be noted, however, that hydraulic flip may not occur at the predicted condition due to hysteresis, entrance imperfections, etc.

9.2 DEAD HEAD CONFIGURATION

Hydraulic flip for this manifold/orifice configuration appears to occur only for turning angle of 90°, see Appendix B. Table 3 provides a summary of the conditions and value of cavitation index, at hydraulic flip, for L/D of 2, 5, and 10. Note that hydraulic flip did occur in the three-flow regime stated above.

Table 3: Dead Head Hydraulic Flip Characteristics

D_2 = 1.02 mm   Angle = 90°

K_{crit}	L/D	P_1 MPa	NC	IC	SC	K_{IFC}
1.72	2	0.689	DH			1.82
		3.45			1.72	
		6.89			1.64	
		10.34			1.72	
1.48	5	0.689	DH			1.77
		3.45			1.48	
		6.89			1.48	
		10.34			1.48	
1.37	10	0.689		1.56		1.54
		3.45				
		6.89				
		10.34				

D_2 = 2.04 mm

K_{crit}	L/D	P_1 MPa	NC	IC	SC	K_{IFC}
1.72	2	0.689	DH			1.72
		3.45		1.93		
		6.89			1.64	
		10.34			1.54	
1.48	5	0.689	DH			1.84
		3.45			1.48	
		6.89				
		10.34				
1.37	10	0.689				1.54
		3.45				
		6.89				
		10.34				

For L/D of 2 and 5, hydraulic flip occurred in the non-cavitation flow regime at P_1 of 0.689 MPa. At higher P_1 hydraulic flip did not occur in non-cavitation flow regime. At

L/D = 10 hydraulic flip only occurred at inception of cavitation for the 0.04 in orifice diameter.   There were only two incidents of hydraulic flip within the inception of cavitation flow regime, and the values are within those expected for this flow regime.

There is insufficient data at this time to attempt a hydraulic flip model for this configuration, but it would be expected that hydraulic flip in the inception of cavitation flow regime would be based on the orifice entrance characteristics; while within the supercavitation flow regime it would be based on the orifice exit characteristics.

9.3 APPROACH VELOCITY CONFIGURATION

The hydraulic flip characteristic for the approach velocity configuration is almost identical to the dead head (see Appendix B). Northrup [39] also studied 90° turning angle at 0 cross velocity and found similar results. Specifically, L/D = 3 and D_2 = 1.32 mm resulted in hydraulic flip occurring at K_{HF} = 1.57, which is slightly below K_{crit} = 1.61.

Table 4: Approach Velocity Hydraulic Flip Characteristics

D_2 = 1.02 mm

K_{crit}	L/D	P_1 MPa	NC	IC	SC	K_{IFC}
1.72	2	0.689	AV			1.82
		3.45			1.72	
		6.89			1.64	
		10.34			1.72	
1.48	5	0.689		AV		1.78
		3.45			1.48	
		6.89			1.48	
		10.34			1.48	
1.37	10	0.689		1.56		1.64
		3.45				
		6.89				
		10.34				

Angle = 90° D_2 = 2.04 mm

K_{crit}	L/D	P_1 MPa	NC	IC	SC	K_{IFC}
1.72	2	0.689	AV			1.79
		3.45		1.93		
		6.89			1.64	
		10.34			1.54	
1.48	5	0.689			1.48	1.82
		3.45				
		6.89				
		10.34				
1.37	10					1.51
		3.45				
		6.89				
		10.34				

Chew [38] results for L/D = 2 and $D_2 \sim$ 1.09 mm, where the manifold exit was closed so that the configuration was consistent with the approach velocity configuration, indicated hydraulic flip for P_1 > 0.689 MPa of $K_{HF} \sim$ 1.68.   When P_1 was < 0.689 MPa, the hydraulic flip was in the inception of cavitation flow regime between 2 and 2.5.   In addition, hydraulic flip also occurred in the non-cavitation flow regime at the lowest P_1.

9.4 BRANCHING CONFIGURATION

The available hydraulic flip data for branching configurations is very limited, and only two studies available in the open literature offer any insight into hydraulic flip for this configuration.   For branching configurations, mechanisms have been postulated by Northrup [39], Chew [40] and Nurick, et al. [4].

In the Nurick, et al. study using variable turning angle configuration, the upstream pressure was constant, and the exit pressure varied during a test resulting in constant

manifold input flowrate and variable orifice flowrate and W_2/W_1. In branching flow the velocity ratio can be varied from test to test, thereby allowing evaluation of this variable on hydraulic flip. A summary of these results is given in Table 5. Note that hydraulic flip was found only for the L/D of 2 and 5. At 0.689 MPa, upstream pressure hydraulic flip occurred in the non-cavitation flow region, identical to the other two configurations. All other occurrences were in supercavitation.

Table 5: Branching Hydraulic Flip Characteristics

D_2 = 1.02 mm   Angle = 90°

K_{crit}	L/D	P_1 psig	NC	IC	SC	K_{IFC}
1.72	2	0.689	BR			1.82
		3.45			BR	
		6.89			BR	
		10.34			BR	
1.48	5	0.689			BR	1.77
		3.45				
		6.89				
		10.34				
1.37	10	0.689				1.54
		3.45				
		6.89				
		10.34				

D_2 = 2.04 mm

K_{crit}	L/D	P_1 psig	NC	IC	SC	K_{IFC}
1.72	2	0.689	BR			1.72
		3.45			BR	
		6.89			BR	
		10.34			BR	
1.48	5	0.689			BR	1.84
		3.45				
		6.89				
		10.34				
1.37	10	0.689				1.54
		3.45				
		6.89				
		10.34				

Figures 51 and 52 are plots showing the cavitation index for L/D of 2 and 5, where hydraulic flip occurred. In all cases hydraulic flip occurred at or near the critical cavitation as defined by Bergwerk.
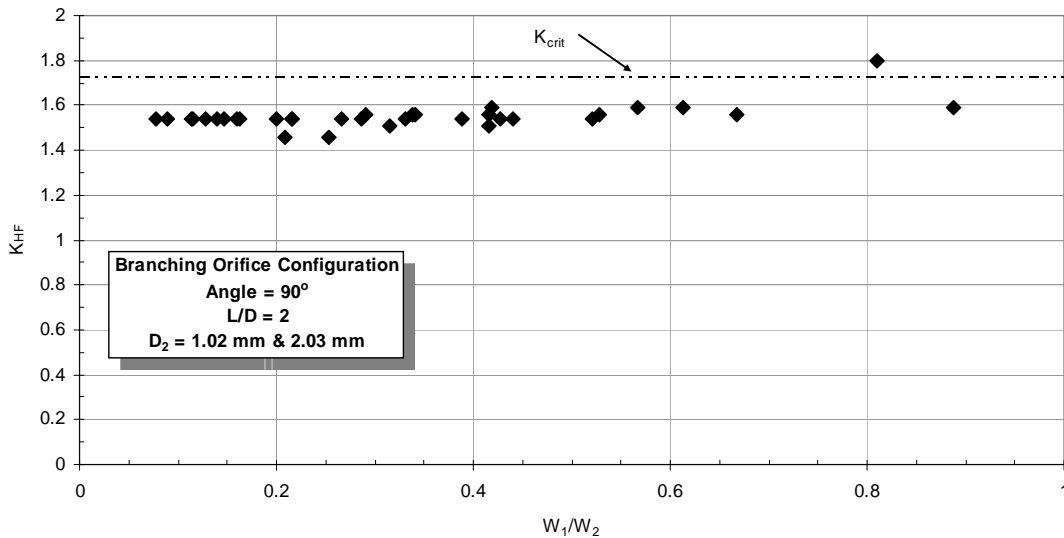
Figure 51: Hydraulic Flip for Branching Orifice Configuration; L/D = 2
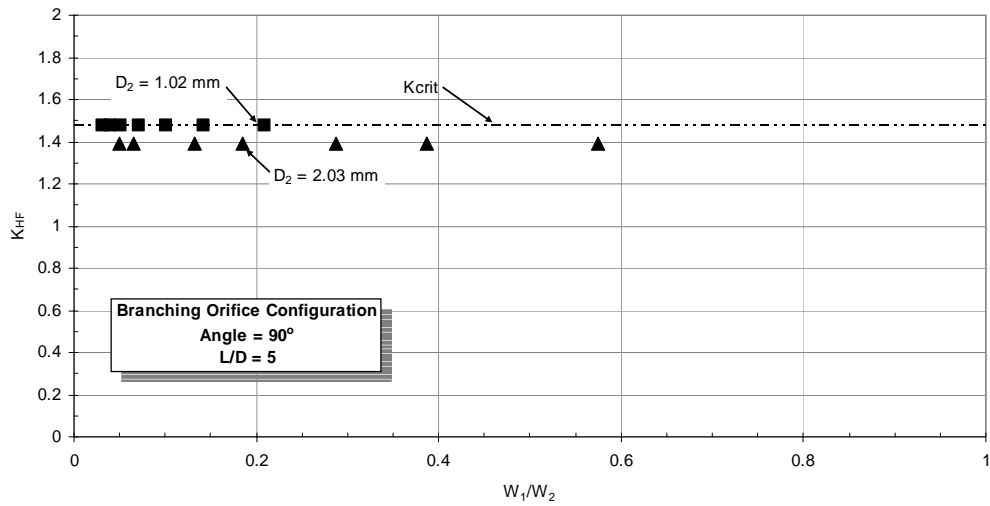
Figure 52: Hydraulic Flip for Branching Orifice Configuration

The Northrup experimental results [39] are incomplete in that the flowrate ratio is not provided, but separation occurred with variation in cross velocity of 3.05 - 6.1 m/sec at K_{HF} between 1.49 – 1.33, respectively. This would be consistent with the above results.

Chew [40] also utilized a 90° turning angle configuration in which the upstream pressure was varied at constant exit pressure and the bypass flowrate varied to maintain the orifice flowrate constant. His results are presented in Fig. 53 and show that hydraulic flip occurs in supercavitation and at KHF ~ 1.54, which is consistent with that shown in Fig. 51.
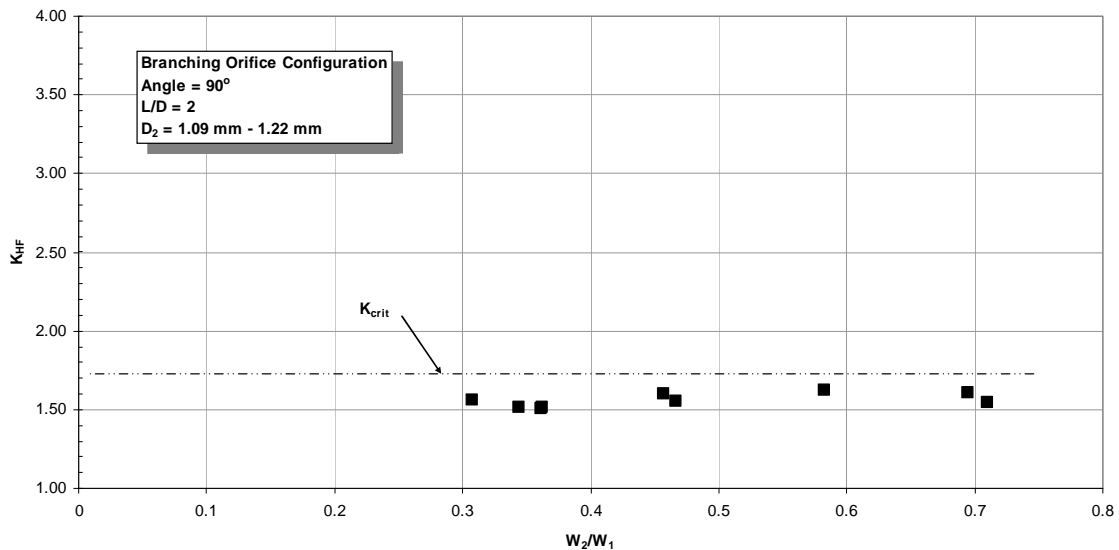
Figure 53: Hydraulic Flip for Branching Orifice Configuration Chew [40]

What is known is that turning of the flow from the manifold to enter the sharp edge orifice contraction suppresses separation. An exception appears to be a 90° turning angle. Hydraulic flip occurs in the non-cavitation flow regime up to inception of cavitation Hydraulic flip data from the [4] study shows that hydraulic flip did not occur for turning angles of 60, 75, 105 and 120 degrees. However at 90°, turning angle hydraulic flip did occur.

9.5 SUMMARY OF HYDRAULIC FLIP PREDICTIVE STATUS
The complexity of the dynamics of the separation process and interaction with geometry makes any comprehensive model of hydraulic flip unlikely until sufficient data are made available to separate the various impacts. However, the controlling mechanisms are likely to be dependent on the flow regime where hydraulic flip occurs. This will require separate models for each flow regime. In addition hydraulic flip is very sensitive to small variations in manufacturing tolerances at the orifice entrance impacting the ability of the contracting flow to achieve reattachment of the contraction/expansion flow within the orifice L/D restrictions as well as pressure perturbations (i.e., both amplitude and frequency) at the contraction orifice entrance. Without exact *a priori* knowledge of the magnitude and location of these variables, prediction of hydraulic flip can only be indicated as a possibility and verifiable only upon testing. Multiple orifices on any given design add another level of potential difficulty in predicting hydraulic flip for any specific orifice. Obviously, building a design and finding hydraulic flip in any given orifice can significantly impact unit cost depending on the required fix.

It is instructive to note that the selection of the cavitation index, defined by Equation 30 for hydraulic flip in the supercavitation flow regime, is based on the equivalency between it and the pressure recovery factor.

10.0 STATUS OF CDF HYDRAULIC CODE PREDICTION VERIFICATION

10.1 IN-LINE CONFIGURATION
Verification of CFD simulation hydraulic models has been conducted over the last 15 years. These studies have verified the one-dimensional model of Nurick [2] as well as the initiation of cavitation. The earliest work, 1997, involved a two-dimensional model of Schmidt, et al. [41], where the discharge coefficients as a function of the cavitation index were compared with theory. The results of this comparison are shown in Fig. 54.
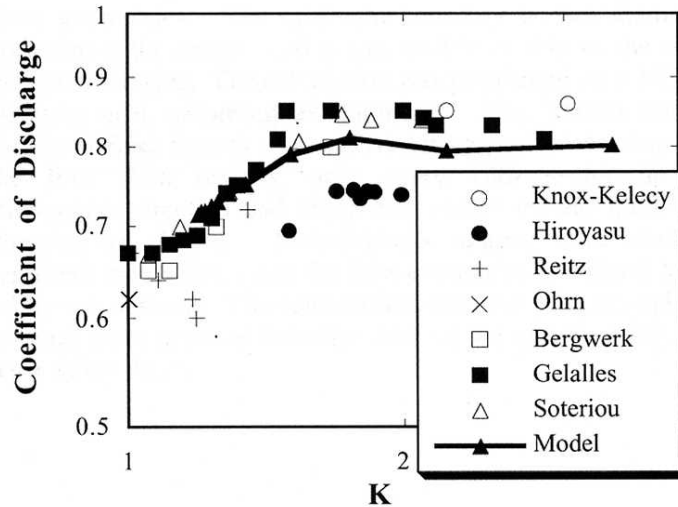
Figure 54: Experimental Coefficient of Discharge Comparison with Theory [41]

In 2005 Tepes [42], utilizing the FLUENT v6.1 model, compared the Nurick [2] data with the CFD simulation predictions and found that both the one-dimensional model proposed by Nurick as well as the inception of cavitation were correctly predicted.

Palau, et al. [43] in 2007 conducted a study to compare the FLUENT v6.1 hydraulic CFD code simulation predictions with a wide range of configurations. Included in this study was the work of Nurick [2] for both circular and rectangular orifices. The comparison of the simulation with experimental data is shown in Figures 55 and 56 for the circular and rectangular orifices, respectively. Note the excellent comparison.

While the above studies have shown that the discharge coefficient and inception of cavitation can be predicted by CFD, there are still a significant number of other variables that need to be verified. These include the length of the cavity with cavitation index, the recompression characteristics, and the orifice exit characteristics (i.e., velocity and mass profile, turbulent intensity, and vorticity) as well, and the turbulent intensity at the orifice entrance. In order to make this comparison, additional experimental data will be required. However, in some cases limited data is available for specific geometry and operating conditions and is discussed in this Report. A comprehensive study of hydraulic flip employing well-defined orifice geometry and finishes is required to fully identify the conditions where they occur. Once the "ideal" orifice geometry hydraulic flip characteristics are determined, an additional study to determine the impact of variations from "ideal" will provide the broader base for predicting hydraulic flip from axial in-line configurations. In the interim, the data of Nurick [4] and Diamond [27] showing hydraulic flip conditions should be compared with CFD code simulation predictions. The limited data showing velocity profiles at the orifice exit should also be used to verify that the CFD code is providing reasonable profiles with experimental data.
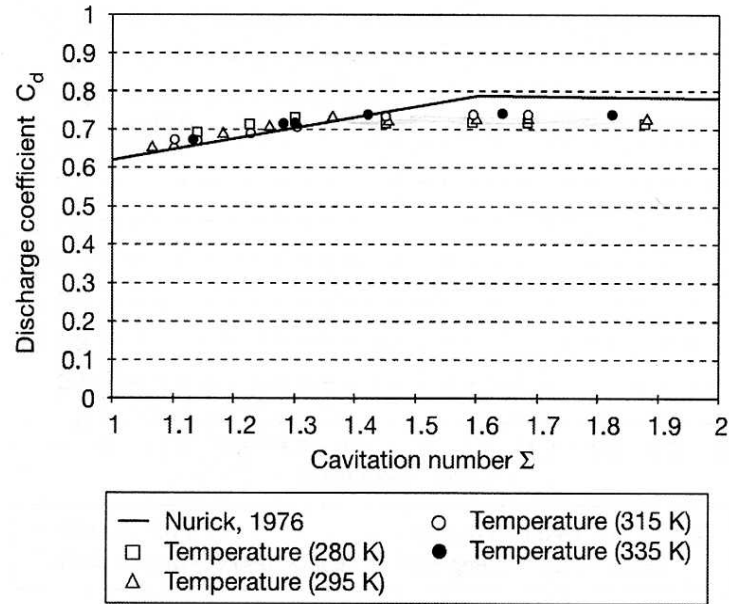
**Figure 55: Comparison of Circular Orifice Data with FLUENT v6.1 [43]**
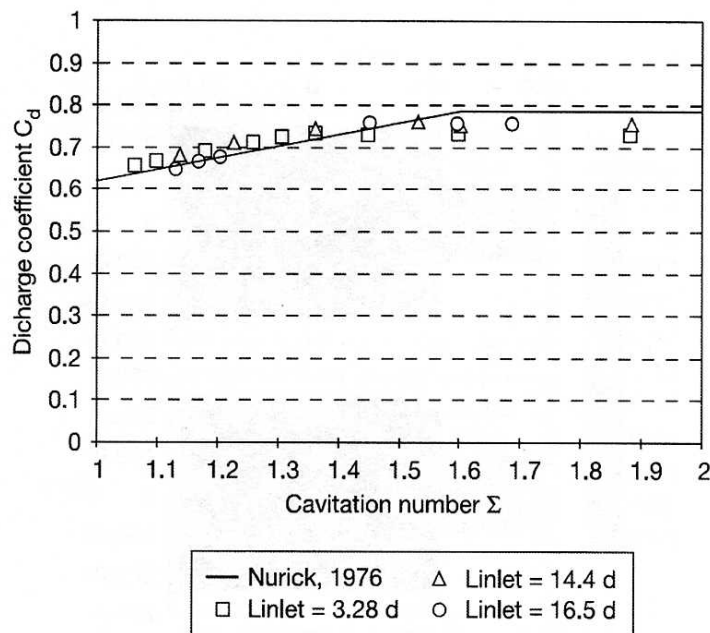
Figure 56: Comparison of Rectangular Orifice Data with FLUENT v6.1 [43]

It is clear that full verification of CFD simulation predictions requires additional experimental data, especially related to the orifice exit characteristics.

10.2 BRANCHING CONFIGURATION

The only study found is by Xu, et al. [42], which utilized the data presented in Nurick [2] and a 3D two-phase Navier-Stokes solver developed by Bunnell and Heister [45]. Xu utilized the Nurick definition for cavitation. The simulation provided information on the discharge coefficient in the cavitation region, as indicated in Fig. 57.
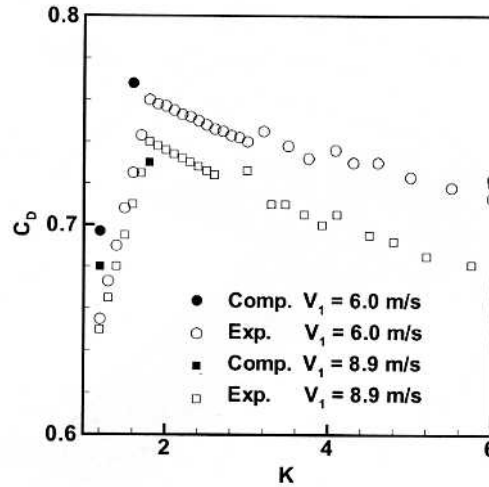
Figure 57: Comparison of Discharge Coefficient with Simulation [45]

The simulation results provide excellent comparison with the experimental data, in addition to predicting inception of full cavitation at ~ 1.8.

11.0 SUMMARY

11.1 SUMMARY OF STATUS OF CFD MODEL DEVELOPMENT

The potential power of CFD analysis cannot be overstated. It can potentially provide the user with the ability to perform design studies that can result in significant reduction in development time and cost. What must be established first is that the hydraulic CFD code can predict the hydraulic characteristics in the orifice as well as the manifold and the orifice exit flow characteristics, which are the initial boundary conditions for the free jet characteristics. The free jet characteristics then provide the initial conditions at jet impingement, etc, to the eventual spatial mixing and spray formation. The final spatial spray distributions then dictate the eventual combustion performance and combustor wall heat transfer compatibility. And finally, the detailed spatial orifice, free jet, impingement and formation processes provide the detailed process information necessary for development of and understanding of the interaction of the complete designand processes leading to final spatial spray formation, as well as the combustion process within the combustion chamber on the sensitivity of the final design to provide stable combustion. Combustion stability is the most difficult of all the other processes occurring within the combustion chamber to predict. However, without detailed knowledge of the processes

between propellant inlet into the injector manifold and the spatial spray formation, prediction of combustion stability will remain at the current empirical prediction level.

It is important to understand that exhaustive experimental data are not required to validate CFD model simulation predictions. Careful selection of the test conditions, especially including limit case conditions, can provide the verification necessary for assessment of the validity of CFD model prediction. The existing experimental data for the jet and droplet size determination database, as well as combustion stability and performance, can be reevaluated to include the orifice exit conditions as long as the hardware design and input conditions are known. Currently, these predictions can only be used if the exact geometry and input conditions for which the data was generated match. Consequently, the key to including this data in CFD analysis is knowledge of the orifice exit flow characteristics. Lastly, although limited, the comparisons of simulation prediction and experimental data discussed in this report clearly show that CFD analysis has the potential to provide excellent simulation of orifice hydraulic and exit flow characteristics.

ACKNOWLEDGEMENTS

12.0 NOMENCLATURE

ACRONYMS and SYMBOLS

A, B, C	Constants Defined in Eq. 18 & 25
A_1	Manifold Area
A_2	Orifice Area
A_2/A_1	Area Ratio
A_c	Vena-Contracta Area
CFD	Computational Fluid Dynamics
C_c	Contraction Coefficient, A_2/A_c
C_d	Discharge Coefficient
D_1	Manifold Passage Diameter
D_2	Contraction Orifice Diameter
ΔP	Overall Pressure Drop
f	Orifice Friction Factor
HL	Total Head Loss
HL1-c	Head Loss; Orifice Entrance to Vena-Contracta
HL_{1-r}	Head Loss; Orifice Entrance to Reattachment
HL_{1-2}	Head Loss; Orifice Entrance to Exit
HL_{fr}	Orifice Friction Head Loss
K_{cav}	Cavitation Index Eq. 29
K_{crit}	Value of K_{cav} at inception of Supercavitation
K_{IFC}	Value of K_{cav} at Inception of Full Cavitation
K_{INC}	Value of K_{cav} at Inception of Cavitation
K_L	Entrance to Reattachment Loss Coefficient
KE	Kinetic Energy
KL	Minor loss coefficient
L	Orifice LengthL_{cav} Vapor Cavity Length
L/D	Orifice Length/Diameter Ratio
LHS	Left-Hand Side
P_1	Manifold Inlet Pressure
P_2	Back Pressure Downstream of Contraction Orifice Exit
P_c	Pressure at Vena-Contracta
P_v	Fluid Vapor Pressure
PHF	Partial Hydraulic Flip
r/D	Contraction Orifice Entrance Radius/Orifice Diameter
Re	Reynolds Number
Re_{IFC}	Reynolds Number at Inception of Cavitation
RHS	Right-Hand Side
THF	Total hydraulic flip
TI	Turbulence Intensity at Orifice Exit
V_1	Manifold Entrance Velocity
V_2	Contraction Orifice Velocity based on Continuity
V_1/V_2	Velocity Ratio

V_c	Vena-Contracta Velocity
W_1	Manifold Inlet Flowrate
W_2	Contraction Orifice Flowrate

GREEK

ρ	Liquid Density
θ	Turning Angle
μ	Fluid Viscosity
σ	Cavitation Index; Eq. 28

13.0 REFERENCES

1. Idelchik, I. E., 1994. Handbook of Hydraulic Resistance. 3rd edition (translated). CRC Press, Inc., Boca Raton, FL.
2. Nurick, W. H, "Orifice Cavitation and its Effect on Spray Mixing," Trans. ASME, J. Fluids Engineering, 7, 681-687, 1976
3. Nurick, W. H., Ohanian, T., Talley, D. and Strakey, P., "Impact of L/D on 90 Degree Sharp-Edge Orifice Flow with Manifold Passage Cross Flow," Submitted to J of Fluids Engineering
4. Nurick, W. H., Ohanian, T., Talley, D.G., Strakey, P. A., "The Impact of Manifold-To-Orifice Turning Angle on Sharp-Edge Orifice Flow Characteristics in Both Cavitation and Non-Cavitation Turbulent Flow Regimes," Journal of Fluids Engineering, Vol. 130, Nov., 2008
5. "Flow of Fluids," Crane Co., Tech Paper 410
6. Balumeister & Marks, Standard Handbook for Mechanical Engineers, 7th Ed., McGraw-Hill Book Co.
7. Engineering Hydraulics, Wiley, New York, 1950
8. Perry, R. H., and Chilton, C. H., Chemical Engineers Handbook, McGraw-Hill, 5th Edition, 1963
9. Vernard, J. K., "Elementary Fluid Dynamics" John Wiley & Sons, 3rd Edition, 1963
10. Munson, B. R., Young, D. F., and Okiishi, T. H., Fundamentals of Fluid Mechanics, John Wiley and Sons Inc., 3rd Ed
11. Costa, N., P., Maia, R., and Pinho, F., T., "Edge Effects on the Flow Characteristics in a 90 deg Tee Junction," Trans of the ASME, Vol. 128, November, 2006
12. Weisbach, J., "Die Experimental Hydraulik," 1855Standards of the Hydraulic Institute, 8th ed., Hydraulic Institute, NY, 1947
13. Hamilton, J. B., "The suppression of Intake Losses by Various Degrees of Rounding," Univ. of Wash. Engr. Expt. Sta., Bull., 51, 1929
14. Echouchene, F., and Belmabrouk, H., "Computation of Cavitating Flows in a Diesel Injector," IOP Conf. Series: Materials Science and Engineering, 13 (2010) 012035

15. Chaves, H., Knapp, M, Kubitzek, A., Obermeier, F, and T. Schneider, Experimental Study of Cavitation in the Nozzle Hole of Diesel Injectors Using Transparent Nozzles, SAE Paper 950290, March 1955

16. Soteriou, C., Andrews, R., Torres, N., Smith, M., and Kunkulagunta, R., "Through the Diesel Nozzle Hole – A Journey of Discovery II," ILASS-Europe 2001, Zurich, 2-6 Sept., 2001

17. Menter, F., 1994. "Two Equation Eddy-Viscosity Turbulence Models for Engineering," AIAA J, 32, pp. 1598-1605.

18. Ganippa, L. C., Bark, G., Andersson, S., and Chomiak, J., 2004, "Cavitation: A Contributory Factor in the Transition from Symmetric to Asymmetric Jets in Cross-Flow Nozzles," Exp. Fluids, **36**, pp. 627–634.

19. Rahmeyer, W., and Cain, F., "Calibration and Verification of Cavitation Testing Facilities Using an Orifice," Utah State University, Logan Utah

20. "Noise, Vibration, Cavitation, Prevention," Cla-Val Technical Products Department

21. Numachi, F., Yamabe, M., and Oba, R., "Cavitation Effect on the Discharge Coefficient of the Sharp-Edge Orifice Plate," Journal of Basic Engineering, Trans of ASME, Mar. 1960

22. Gopalan, S., and Katz, J., "Flow structure and modeling issues in the closure region of attached cavitation," Physics Of Fluids Volume 12, Number 4 April 2000

23. Sou, A., Tomiyama, A., Hosokawa, S., Nigorikawa, S., Maeda, T., Cavitation in a Two-dimensional Nozzle and Liquid Jet Atomization, JSME Inter. Journal, Series B, V49, No. 4, 2006

24. Pearce, I. D., Lichtarowicz, A., "Discharge Performance of Long Orifices with Cavitation Flow," 2nd Fluid Power Sym. $4^{th} – 7^{th}$ Jan. 1971, Guildford

25. Knapp, R. T., Daily, J. W., and Hammitt, F. G., "Cavitation," McGraw-Hill New York, 1970

26. Hall, G., W., "Analytical Determination of Discharge Characteristics of Cylindrical-Tube Orifices," J. Mech., Engr. Sci., Vol. 5, No.1, 1963

27. Diamond, P., M., "Characteristics of Flow in Short Tubes, with Special Reference to Hydraulic Flip," M. S. Thesis, Univ. of Buffalo, 1954, (Applied Mechanics Reviews 267, 1964

28. Stanley, C, Rosengarten, G, Milton, B, Barber, T, "Investigation of Cavitation in a Large-Scale Transparent Nozzle," University of New South Wales, Australia, F2008-SC-001, 2008

29. Soteriou, C., Andrews, R., and Smith, M., "Direct Injection Diesel Sprays and the Effect of Cavitation and Hydraulic Flip on Atomization," SAE 950080

30. Ramamurthi, K., and Patnaik, S., R., "Influence of Periodic Disturbances on Inception of Cavitation in Sharp-Edged Orifices," Experiments In Fluids 33, 2002

31. Saito, Y and Sato ,K, "Cavitation Bubble Collapse and Impact in the Wake of a Circular Cylinder," Fifth International Symposium on Cavitation, Osaka, Japan, November 1-4, 2003

32. Bergwerk, W., "Flow Pattern in Diesel Nozzle Spray Holes," Proceedings of the Institution of Mechanical Engineers, 173(21), pp 655-660, 1959

33. He, L., Ruiz, F., "Effect of Cavitation on Flow and Turbulence in Plain Orifices for High-Speed Atomization" Atomization and Sprays, Vol. 5, pp569-584, 1995

34. Tamaki, N., Shimizu, M., Nishida, K., and Hiroyasu, H., "Effect of Cavitation and Internal Flow on Atomization of a Liquid Jet" Atomization and Sprays, Vol. 8, pp 179-197, 1998

35. Zajac, L., J., "Correlation of Spray Dropsize Distribution and Injector Variables," Rocketdyne, North American Rockwell R-8455, NASA Jet Prop. Lab., Pasadena, CA, Contract NAS7-726

36. Koivula, T., "On Cavitation in Fluid Power," Proc. Of 1st FPNI-PhD Symposium, Hamburg, Germany, 2000, pp371-382

37. Takahashi, K., Matsuda, H., and Miyamoto, H., "Cavitation Characteristics of Restriction Orifices (Experiment for Shock Pressure Distribution by Cavitation on Restriction Orifices and Occurrence of Cavitation at Multiperforated Orifices due to Interference of Butterfly Valve)" CAV 2001, Session A9.006

38. Rupe, J. H., "On the Dynamic Characteristics of Free-Liquid Jets and a Partial Correlation with Orifice Geometry," Technical Report No, 32-207, JPL, Pasadena. California, January 15, 1962

39. Northup, R. P., "Flow Stability in Small Orifices," American Rocket Society, 30 Nov. 1951, Annual Mtg. of the ASME, Atlantic City N. J.

40. Chew, T., J., "Hydraulic Flip Behavior In Typical Liquid Rocket Operating Regimes," AD-764 730, Air Force Rocket Propulsion Laboratory Edwards Air Force Base, California, July 1973

41. Schmidt, D., P., Rutland, and Corradini, M., L.., "A Fully Compressible Two-Dimensional Model of High-Speed Cavitating Nozzle," Atomization and Sprays, 9, 156-168

42. Tepes, P., "Numerical Simulation of Unsteady Turbulent Cavitating Flow," Universitat Politècnica de Catalunya. Departament d'Enginyeria Mecànica, Bartcelona, Spain, Disertation May 2005

43. Paal, G., Pinho, F., Maia, R., "The Effect of Corner Radius on the Energy Loss in 90o T-Junction Turbulent flows," Conference on Modeling Fluid Flow (CMFF'06), The 13th International Conference on fluid Flow Technologies, Budapest, Hungary, Sept. 6-9, 2006

44. Xu, C., Heister, S. D., and Blaisdell, G.A., "Simulation of Cavitated Flow in Orifices Fed by a Manifold," Atomization and Sprays, vol.14, 2004

45. Bunnell, R. A., Heister, S. D., and Collicott, S. H., "Cavitating Injector Flows: Validation of Numerical Models and Simulations of Pressure Atomizers," Atom. and Sprays, Vol. 9, 1999

46. Lichtarowicz, A., Duggins, R, and E. Markland, Discharge Coefficients for Incompressible Non-Cavitating Flow through Long Orifices, Journal of Mechanical Engineering Science, 7:2, 1965.

47. Gelalles, A. G., Marsh, E. T., "Effect of Orifice Length-Diameter Ratio on the Coefficient of Discharge of Fuel-Injection Nozzles," Tech Notes No 369, National Committee for Aeronautics, Langley Memorial Aeronautical Laboratory, mar. 1931

14.0 APPENDICES

14.1 APPENDIX A - SHARP EDGE ENTRANCE ORIFICE DISCHARGE COEFFICIENT IN NON-CAVITATION

Lichtarowicz [46] represent the most comprehensive study of discharge coefficient in long orifices over a substantial range in L/D. The proposed correlation for Reynolds number up to 10^4 and L/D to 10 is:

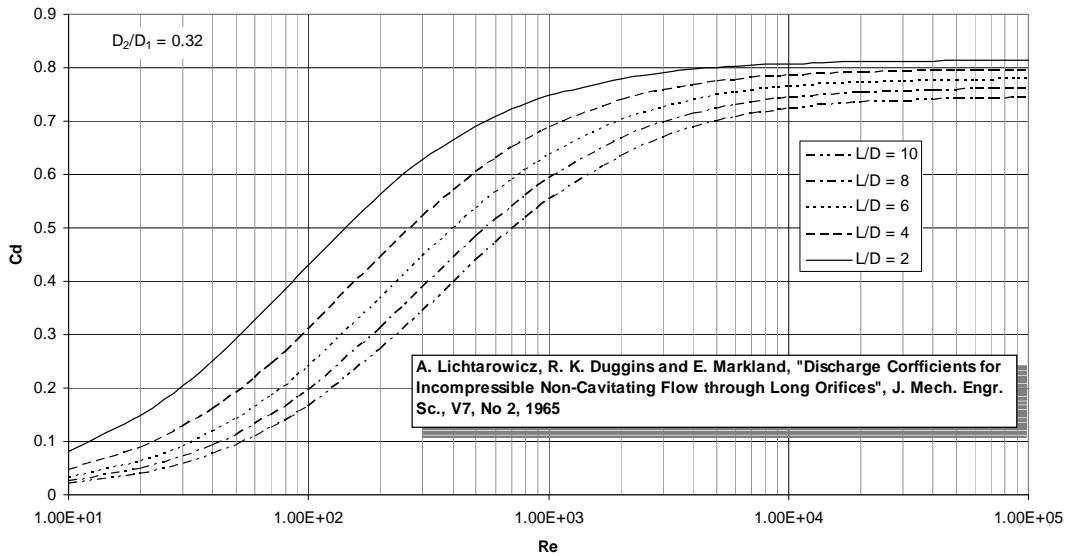$$1/C_d = \sqrt{1-\beta^4}\left[\frac{1}{C_d\max} + \frac{20}{\mathrm{Re}_h}\left(1+2.25\frac{L}{D}\right) - \frac{0.005\dfrac{L}{D}}{1+7.5\left(\log\mathrm{Re}_h - 3.824\right)^2}\right] \quad (1)$$

And:

$$Cd\max = 0.827 - 0.0085\frac{L}{D} \quad (2)$$

$$\beta = D_2 / D_1 \quad (3)$$

Typical values of discharge coefficient as a function of Re are shown in Fig. A1.

Figure A1: Reynolds Number vs. Discharge Coefficient for L/D = 2-10

14.2 APPENDIX B - DEAD HEAD AND APPROACH VELOCITY CONFIGURATIONS CAVITATION CHARACTERISTICS
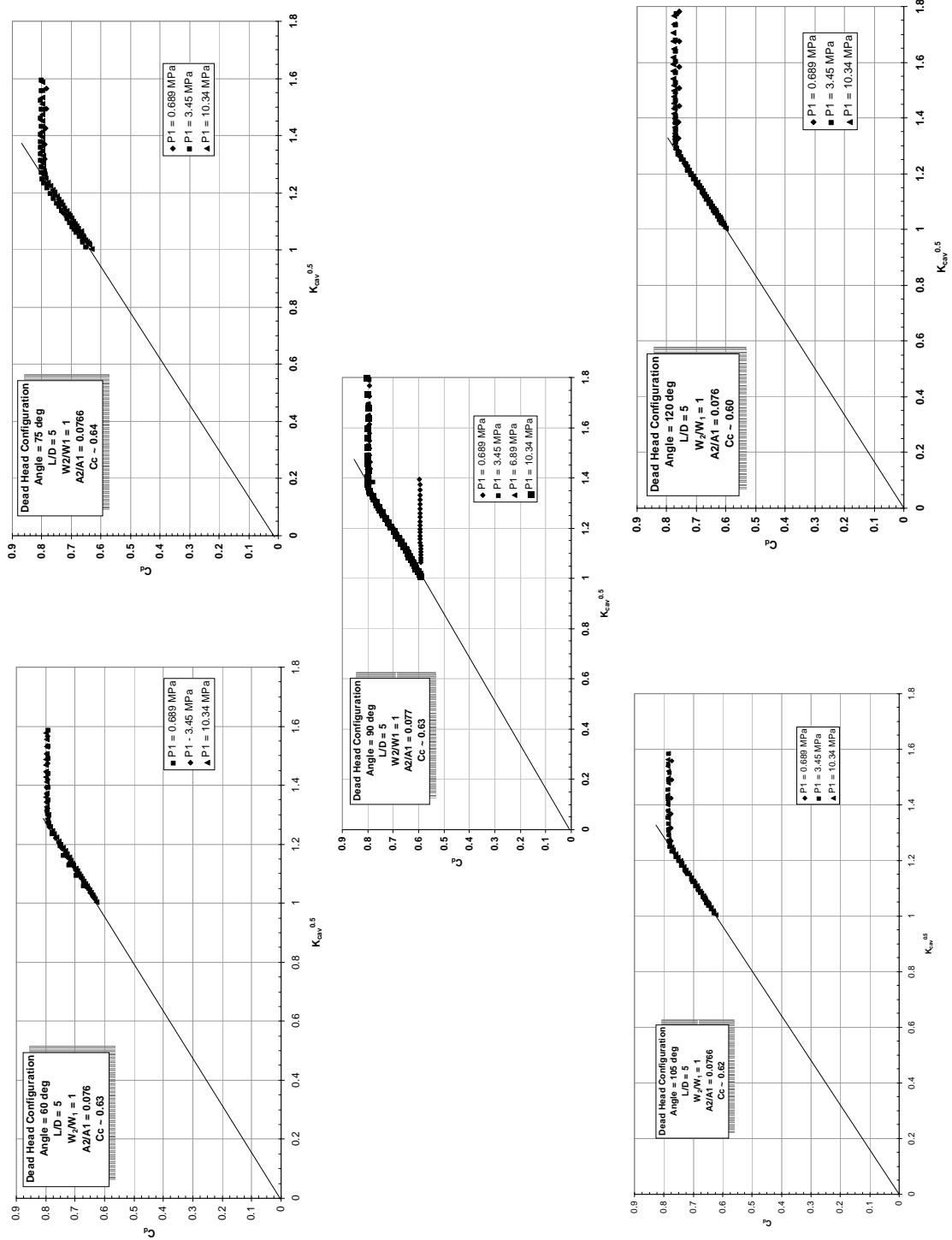
14.2.1 Dead Head Configuration

As shown in Fig. B1 for the dead head configuration, the manifold input flow is divided into two portions wherein the flows must turn before entering the contraction orifice. It is easily seen that only for a 90° turning angle can axisymmetric flow occur.
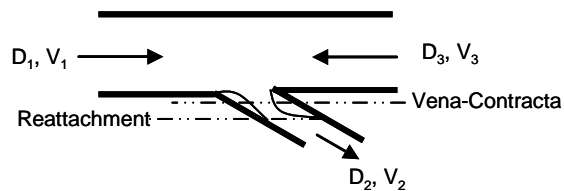

Figure B1: Dead Head Configuration

The measured hydraulic flow characteristics for the dead head configuration are shown in Fig. B2. Note that only at a 90° turning angle hydraulic flip occurred at the lowest value of upstream pressure.

Figure B2: Hydraulic Flow Characteristics for the Dead Head Configuration

The impact of turning angle on KL for both the dead head and approach velocity configurations is shown in Fig. B3.
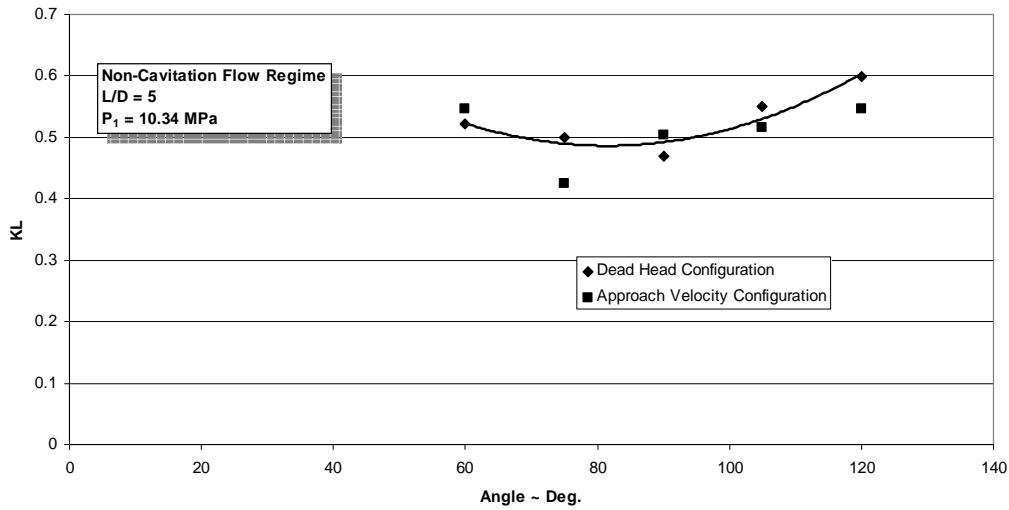
Figure B3: Impact of Turning Angle on Loss Coefficient

The best fit Equation for the impact of turning angle on loss coefficient for both configurations is:

$$KL = .00008\theta^2 - 0.0129\theta + 1.094 \qquad\qquad (B1)$$

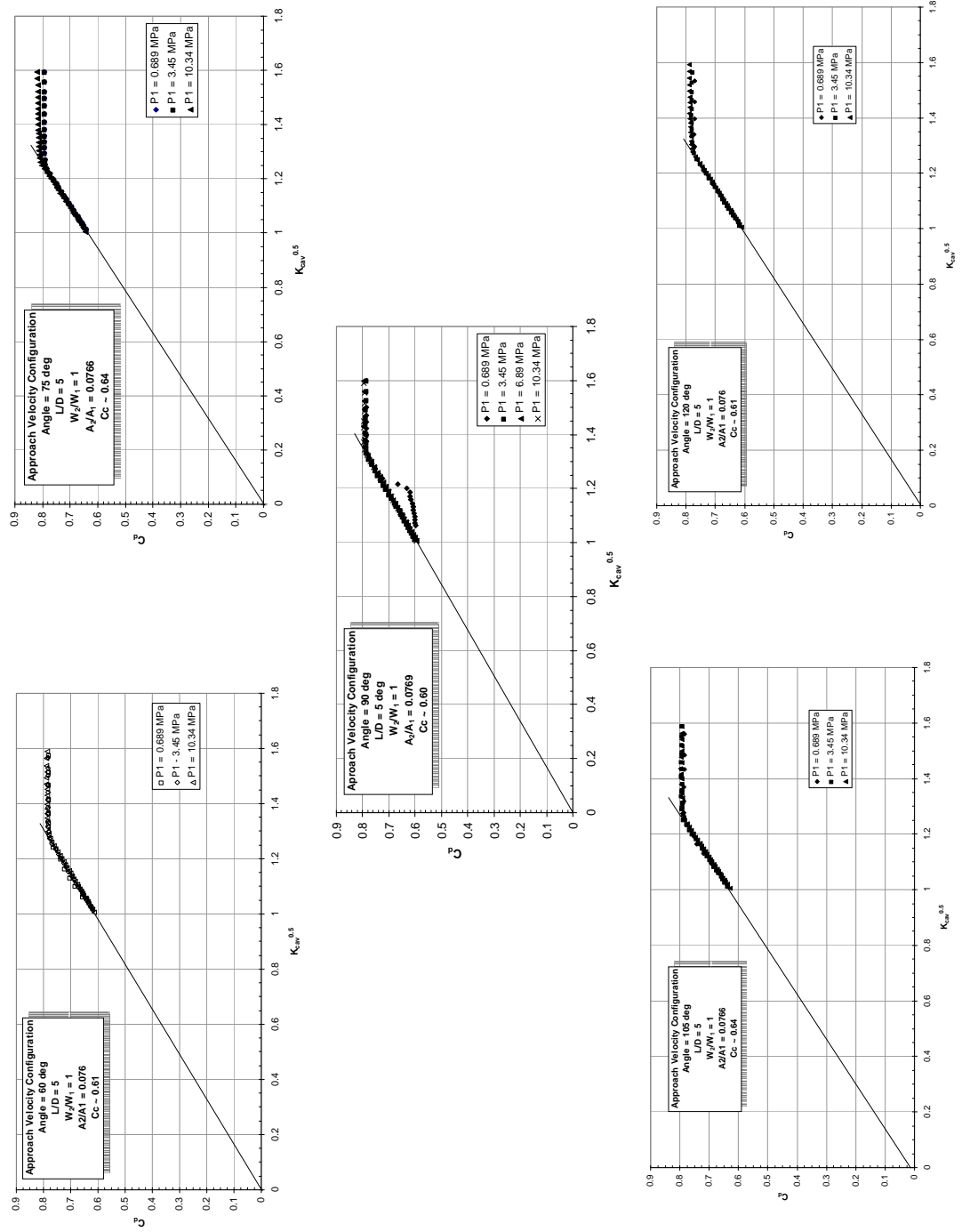### 14.2.2 Approach Velocity Configuration

The approach velocity configuration, as shown in Fig. B4, is fed from one side of a manifold and turns to enter an orifice. The manifold is terminated downstream of the orifice so that 100% of the manifold inlet flow, flows into the orifice. In addition to turning, the termination of the manifold flow causes a reverse flow eddy in the downstream section of the manifold, contributing to the asymmetric flow characteristics within the orifice.
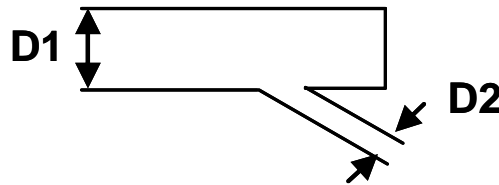
Figure B4: Approach Velocity Configuration

Ganippa [18] noted that the cavitation bubble and vapor generation was significantly different between axial and approach velocity configurations of 80° and 90° turning angles. It was instructive to determine if the overall hydraulic characteristics also varied. The data plots shown in Figures B5 and B6 illustrate that these differences do not impact the overall hydraulic losses but do result in a small change in contraction coefficient and

inception of full cavitation. Note that upstream pressure did not impact the discharge coefficient or the inception of cavitation at each turning angle. However, for the 90° turning angle, at the lowest upstream pressure (i.e., 0.689 MPa), hydraulic flip occurs at the critical value of cavitation index as defined by Bergwerk [32] for L/D = 5.

Figure B5: Hydraulic Flow Characteristics for Approach Velocity Configuration

70

Upper chart:
- Box label: **Approach Velocity Configuration** L/D = 5, $A_2/A_1 = 0.076$, Cd ~ 0.78, $W_2/W_1 = 1$
- Annotation: Axial In-line Configuration [Nurick 1976] L/D = 6, Cd ~ 0.8
- Y-axis: C_d (0.5 to 0.8)
- X-axis: Angle ~ Deg (0 to 140)

Lower chart:
- Box label: **Approach Velocity Configuration** L/D = 5, $A_2/A_1 = 0.076$, Cd ~ 0.78, $W_2/W_1 = 1$
- Annotation: Axial In-line Configuration [Nurick 1976] Cd ~ 0.8
- Y-axis: K_{inc} (1 to 2)
- X-axis: Angle ~ Deg (0 to 140)
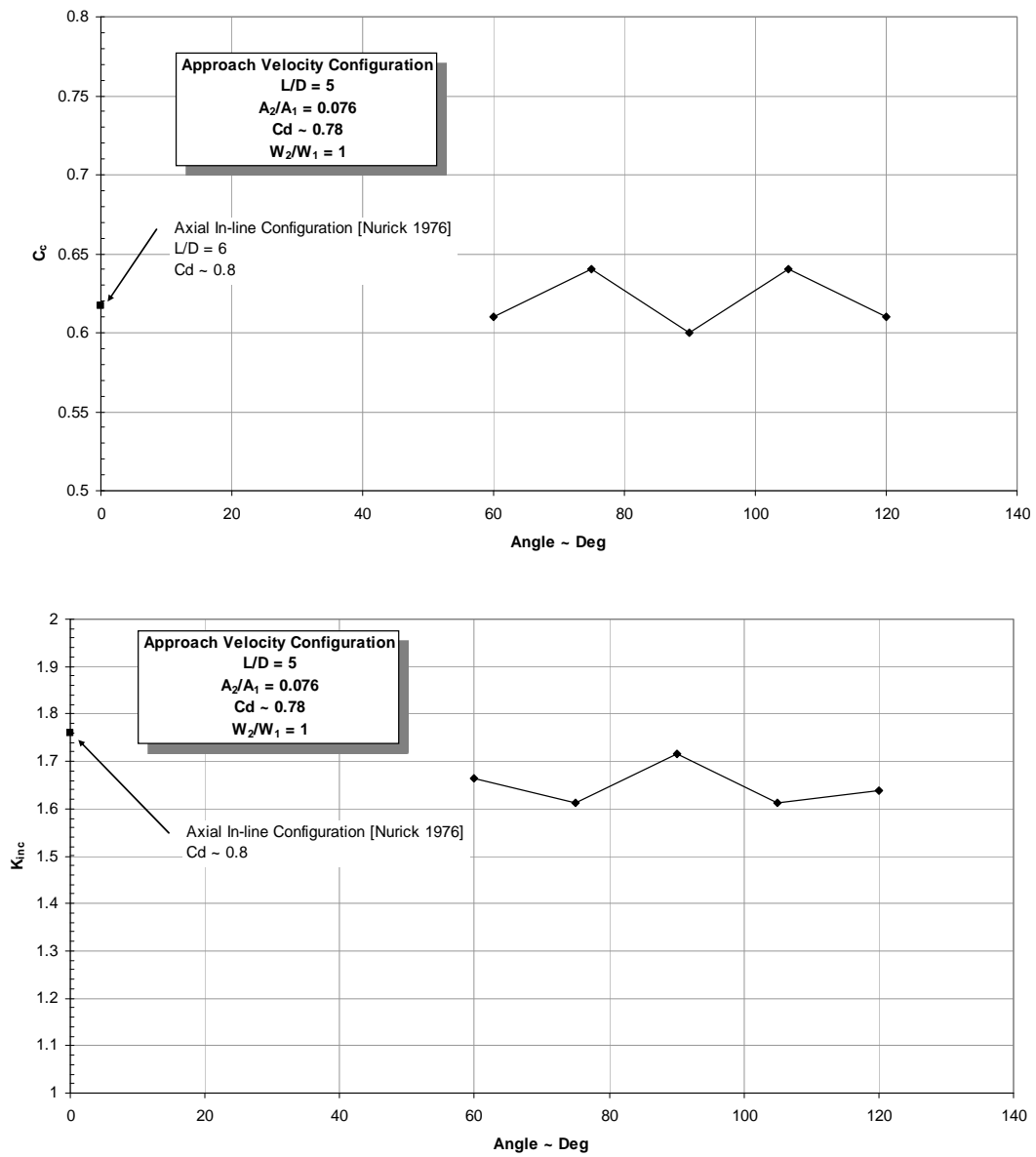
Figure B6: Approach Velocity Configuration C_d and K_{inc} Characteristics

14.3 APPENDIX C – IMPACT OF FLOWRATE RATIO AND CAVITATION INDEX ON CONTRACTION OFIFICE ENTRANCE LOSSES FOR 90° TURNING ANGLE

As discussed in Section 6.5.4, typical entrance losses between the manifold and the contraction orifice vena-contracta for turning angles of 60°, 105°, and 120° are less than 5% of the total head loss over the full range of operating pressures (P_1). Further, this same impact is also true for turning angles of 70° and 90° at upstream pressures equal or greater than 3.4 MPa.

For turning angles of 70° and 90° at upstream pressures of 0.689 MPa, as previously shown in Section 6.5.4, Fig. 31, the entrance loss between the manifold and the contraction orifice vena-contracta varies significantly with both cavitation index and flowrate ratio. As indicated in Fig. C1, the C_d in the non-cavitation flow regime ($K_{cav}^{0.5} > 1.35$) is impacted by the flowrate ratio; decreasing with decreasing flowrate ratio. Note that in the non-cavitation flow regime at constant flowrate ratio, the C_d is constant with cavitation index. Once cavitation is reached, C_d is impacted by both flowrate ratio and cavitation index.
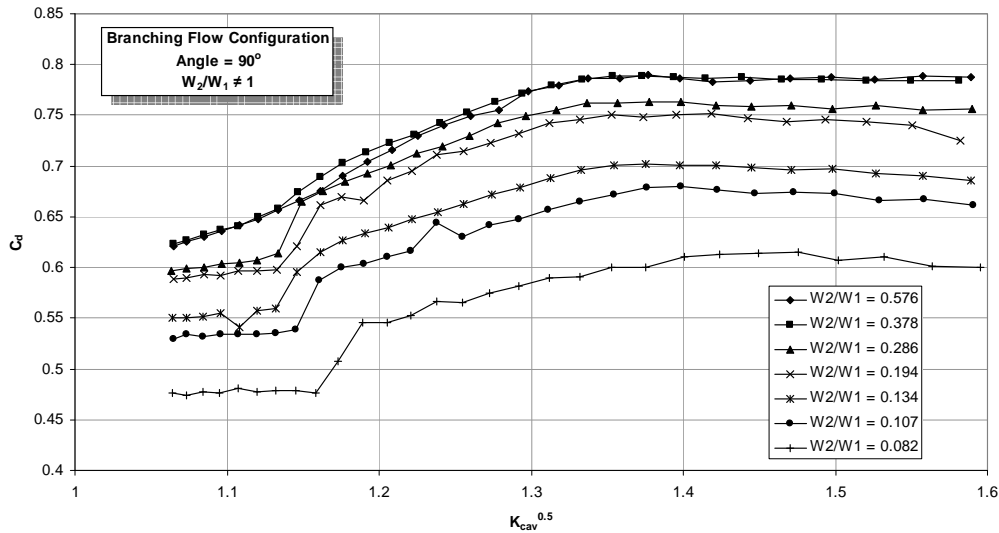
Figure C1: K_{cav} vs. C_d for Various Flowrate Ratios – 90° Turning Angle

The data of Fig. C1 was cross plotted at constant K_{cav} (i.e., a value in the non-cavitation flow regime) as functions of flowrate ratio and C_d, and the result is shown in Fig. C2. As indicated, for values of flowrate ratio > 0.4, entrance losses are independent of flowrate ratio. This characteristic strongly suggests that the impact of both the available pressure head and turning angle results in unstable high loss entrance conditions. Idelchik (1) has indicated similar eddy characteristics for 90° turning angle and similar flowrate ratios.

This characteristic is typical for all values of K_{cav} (or Re) in the non-cavitation flow regime.
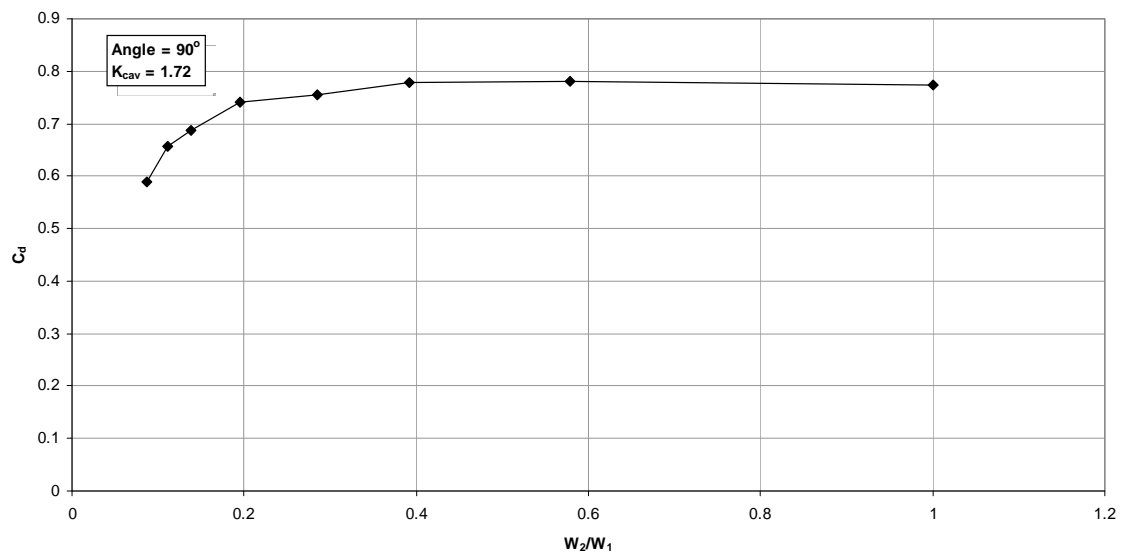
Figure C2: Impact of Flowrate Ratio on Cd at Constant Kcav – 90° Turning Angle

This Page Intentionally Left Blank

AFRL-RZ-ED-TR-2011-0021
Primary Distribution of this Report:

AFRL/RZSA   (1 CD)
Stephen A. Danczyk
10 E. Saturn Blvd.
Edwards AFB CA 93524-7680

AFRL/RZSA   (Electronic)
Record Custodian
10 E. Saturn Blvd.
Edwards AFB CA 93524-7680

AFRL/RZ Technical Library (2 CD + 1 HC)
6 Draco Drive
Edwards AFB CA 93524-7130

Chemical Propulsion Information Analysis Center
Attn: Tech Lib (Mary Gannaway) (1 CD)
10630 Little Patuxent Parkway, Suite 202
Columbia MD 21044-3200

Defense Technical Information Center
(1 Electronic Submission via STINT-TR)
Attn: DTIC-ACQS
8725 John J. Kingman Road, Suite 94
Ft. Belvoir VA 22060-6218